MACH REFLECTION OF GASEOUS DETONATIONS

By

Raza Akbar

A Thesis Submitted to the Graduate

Faculty of Rensselaer Polytechnic Institute

in Partial Fulfillment of the

Requirements for the Degree of

DOCTOR OF PHILOSOPHY

Major Subject: Aeronautical Engineering

Approved by the
Examining Committee:

Dr. Joseph E. Shepherd, Thesis Adviser

Dr. Ashwani. K. Kapila, Member

Dr. Michael M. Abbott, Member

Dr. Amir Hirsa, Member

Dr. John A. Tichy, Member

Rensselaer Polytechnic Institute
Troy, New York

August 1
(For Graduation December 1997)

MACH REFLECTION OF GASEOUS DETONATIONS

By

Raza Akbar

An Abstract of a Thesis Submitted to the Graduate

Faculty of Rensselaer Polytechnic Institute

in Partial Fulfillment of the

Requirements for the Degree of

DOCTOR OF PHILOSOPHY

Major Subject: Aeronautical Engineering

The original of the complete thesis is on file
in the Rensselaer Polytechnic Institute Library

Examining Committee:

Dr. Joseph E. Shepherd, Thesis Adviser
Dr. Ashwani. K. Kapila, Member
Dr. Michael M. Abbott, Member
Dr. Amir Hirsa, Member
Dr. John A. Tichy, Member

Rensselaer Polytechnic Institute
Troy, New York

August 1
(For Graduation December 1997)

CONTENTS

LIST OF TABLES

LIST OF FIGURES

ACKNOWLEDGMENT

At RPI:

Fred Tesman and Charlie Vannier helped immensely in the machine shop. Darwisah Burgess was a big help especially in the final stages of thesis completion. The members of my examining committee helped enormously by responding at short notice and remaining flexible, despite their busy schedules. The friendships of Ed and Lauren Malkiel, Nabeel and Amana Riza, Jonathan Meltzer, Marty Ross, Can Gulen, Ahmed Sabet, Cliff Lansil and Susan McCahan, are especially memorable.

At GALCIT, where this work was carried out in its entirety:

Lori Hsu worked under very difficult circumstances and wrote the bulk of the data acquistion sofware. It was a pleasure to supervise Kumar Raman and watch him take off. Joe Haggerty, Larry Frazier and Ali Kiani delivered all my machining jobs, working with me to get the job done quickly. Alan Goudy often improved my electronic circuits. Jeri Chittum provided a reliable, supportive handling of all paperwork. James Quirk provided useful pointers on organising computations, often through stern and humorous polemics. Chris Krok shared his enthusiasm for working hands-on. Jose and Maria Moriera were good and kind friends. Pavel Svitek, staff engineer at GALCIT, was essential to the design and construction of the detonation tube facility at GALCIT. Mike Kaneshige, built the test-section and set-up the data acquisition system. Indeed, working in the Detonation Physics Laboratory with Pavel and Mike form some of my best memories of life at GALCIT.

Joseph Shepherd patiently trained me, supported me through thick and thin and forced me to learn and produce, at the same time giving me considerable freedom in my work.

My parents, sister and brother gave me unconditional love and support, throughout the course of my studies.

ABSTRACT

The phenomenon of Mach reflection in gaseous detonations was investigated experimentally and numerically using laser shadowgraphy and calculations based on extensions of theories of shock wave reflection. Three different reactive mixtures were used in the experiments: mix 1 was stoichiometric hydrogen and oxygen at 295 K and 20 kPa, mix 2 was a stoichiometric hydrogen and oxygen with 77.5 % argon dilution, at 295 K and 20 kPa. Mix 3 consisted of stoichiometric acetylene and oxygen with 80 % argon dilution, at 50 kPa and 295 K. Detonations in each mixture were imaged interacting with wedges, with the wedge angle, θ, ranging from 15 degrees to 50 degrees. Triple point trajectory angles, χ, were inferred from the shadowgraphs. χ was also obtained from soot foil records for wedge angles of 20, 25 and 30 degrees. Relationships between χ and θ were calculated, using 3-shock theory and Whitham's shock dynamics theory, both with and without energy release. Contours of the leading waves were obtained from the shadowgraphs to investigate the self-similarity assumption. It was found that the Mach reflections mostly exhibited self-similar behavior, with the exception of θ of 30° for mix 1, where the Mach reflection seems to be changing shape, within the field of observation. The calculated χ - θ relations did not agree with those from the experiments, except in the case of mix 2, where, the relation calculated assuming frozen chemistry was in good agreement with the experiments. These results are discussed with regard to, the presence of an intrinsic length scale in gaseous detonations and the behavior of the transverse waves.

CHAPTER 1
Introduction

1.1 Basic Ideas on Detonations and Mach reflections

Detonation waves are a form of both combustion and explosion. Based on physical observations, a detonation is characterized as the region of change (separating the reactants from the products) that moves into the reactants with an effective speed higher than the speed of acoustic signals in the reactants and *exhibits a structure that is a mechanism for self sustenance*. The speed separates detonations from other forms of combustion such as flames, and the mechanism of propagation keeps them from being categorized as simply shock waves followed by chemical reaction. Figure 1.1 is a shadowgraph of a detonation wave in a diluted hydrogen oxygen mixture, moving from left to right. The complicated structure of the wave consists of shock waves moving both in the direction of propagation and transverse to it, and forms the mechanism for the propagation of the entire front. Locally, on any section of the main front, a coupling takes place between the dynamics of the various shocks, the flow and the explosive chemical reaction. Extensive research (Strehlow 1971) has shown that this local coupling is occurring cyclically, forming a substructure to the front as a whole, making detonations 'cellular' in nature. The fact that this behavior is typical of detonations in all detonatable media (solid, liquid or gas phase) is well established.

The subject of gaseous detonations alone is a highly researched one, and it is difficult to summarize the experimental and theoretical aspects succinctly. Thus, only the prominent ideas and results of past research on gaseous detonations that are useful in gaining an appreciation of the present work are summarized below.

1.1.1 Analytical Approximations: Chapman-Jouguet Theory

Short of simulating the waves numerically, the complicated nature of detonations forces analytical approaches to use models that only approximate their gross behavior. As a first step, the self-propagation mechanism is altogether ignored,

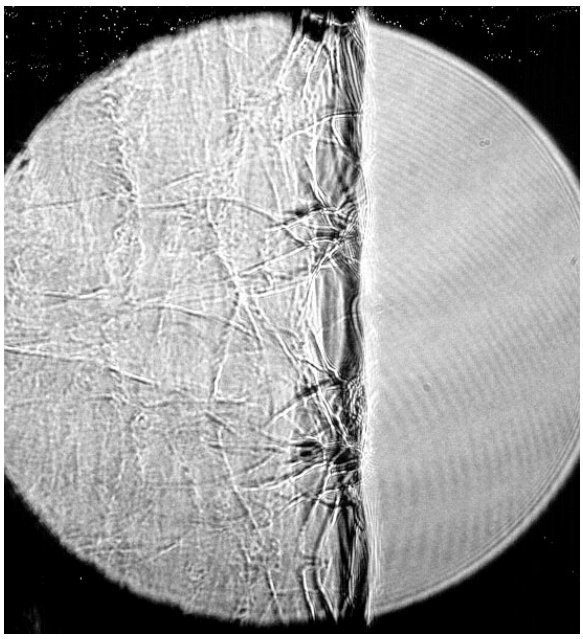

Figure 1.1: Detonation wave in $2H_2 + O_2 + 17.0$ Ar at 20 kPa and 295K

and the wave region is modeled by gas-dynamic discontinuities patched together to produce a self-consistent construction. One such model is the Chapman-Jouguet model. In this simplest, one-dimensional consideration, a detonation wave is a single discontinuity in space separating the mixture of reactants from the products. This is identical to the mathematical treatment of shock waves, but with the addition of energy release (Thompson 1972). Each mixture is separately in its own state of equilibrium, with no consideration of the approach to equilibrium (no chemical kinetics). A special consequence of the analysis of a Chapman-Jouguet wave is that the flow velocity in the products is exactly sonic with respect to the wave. Thus, the wave should remain unaffected by acoustic disturbances in the flow behind it. This result is supported by experimental evidence (Vasiliev et al. 1972).

Despite its simplicity, the Chapman-Jouguet model is used to calculate a value of the equilibrium wave speed of a self-propagating detonation (called the CJ wave speed, D_{CJ}) that is very close to that measured in actual experiments. The CJ model is also useful in extending theories established for shock waves to detonation waves, and was used towards this end in all calculations in the present work.

Another analytical construct of a detonation wave known as the ZND model

(Lee 1984) is also useful in interpreting detonation wave behavior. In this model the detonation is treated as a shock followed by a region of chemical reaction. Using a calculated CJ wave speed, chemical kinetics calculations are performed in conjunction with one-dimensional conservation relations of gas-dynamics to yield a profile of this region including its effective extent (Shepherd 1986), known as the reaction zone thickness.

1.1.2 Cell Width

A CJ detonation in a particular mixture has a characteristic length scale known as the cell width. This is associated with the mechanism of propagation of the front and is defined to be the maximum spacing obtained between the transverse traveling waves on the main front. This is also known as the transverse wave spacing, λ.

It has been shown that mixture cell size is related to the effective ZND reaction zone thickness of the mixture (Lee 1984). The relationship is approximately linear. Such relations have proved useful in developing correlations between parameters of explosive performance, such as initiation energy, and physical length scales, such as charge diameter (Lee 1984; Shepherd 1986). Mixture cell widths are obtained using soot foils, that are placed along the walls of the detonation tube. A detonation wave traveling over the foil upsets the uniform soot layer, leaving a characteristic 'fish-scale' pattern (called cells) that is the mark of the instability of the wave.

1.1.3 Velocity Deficit

A deficit always exists between the calculated value of D_{CJ} and that measured experimentally (labeled D). This deficit is attributed to energy and momentum losses that the wave experiences in a confinement (Fay 1959), and to the multi-dimensional structure of the front. Therefore, the deficit depends on the geometry of the containing vessel and the type of explosive mixture and is considered a measure of departure from ideal Chapman-Jouguet behavior. A corollary to this is that if a wave speed measured in the laboratory is found to be greater than the calculated one for the mixture, the wave had not approached the near CJ state in that vessel. Such waves are said to be 'overdriven', with the degree of overdrive defined as D/D_{CJ}.

1.1.4 Effect of Dilution

If a stoichiometric mixture is diluted, both the chemical kinetics and the energetics are modified. For the same initial pressure and temperature, and large enough dilution (greater than about 25%), the mixture cell size increases and the effective energy release per unit volume decreases with increasing dilution. This can be clearly seen in the dilution study given in the appendix (Fig B.1).

1.1.5 Mach Reflections

When a shock impinges on a surface, a reflected shock wave is produced. This 2-shock configuration, known as regular reflection, is obtained for sufficiently large values of the wedge angle θ, given a fixed incident wave strength (Fig. 1.2). The mechanism of this type of reflection is explained by considering the flow in a reference frame that is moving with the point of reflection (Thompson 1972). The oncoming flow, in this frame, is deflected towards the wedge by the incident wave. As the deflected flow cannot move into the wedge, a reflected wave is needed to deflect it back, parallel with the wall.

If θ is decreased, keeping the incident wave strength fixed, a critical value of θ is reached for which a 2-shock configuration is no longer obtained. This is because, within the 2-shock construct, the flow deflection across the reflected wave is insufficient to deflect the flow back, parallel to the wall. A 3-shock configuration, known as Mach reflection, is observed under these conditions (Fig. 1.3), and the critical value of θ for this change of configuration is known as the transition angle.

Mach reflections are analyzed with certain assumptions based on observed behavior (Hornung 1986). A basic assumption is that the angle χ does not change as the reflection configuration proceeds along the surface of the wedge. If this is true, and chemical reaction and transport effects are ignored, there is no length scale in the problem other than the position of the wave along the wedge. Thus, a Mach reflection at any position on the wedge could be scaled to resemble itself at an earlier or later position along the wedge. This is to say that the reflection process is self-similar about the angle χ, i.e. the angle χ fully describes the problem. This behavior has been verified experimentally for a range of conditions (Hornung 1986).

The ideas from non-reactive shock wave analysis of Mach reflection have been directly extended to detonations, and both regular and Mach reflections have been studied (Bazhenova et al. 1965; Edwards et al. 1984). Examples of each type of reflection from the current work are shown in Figures 1.4 and 1.5. It can be immediately noticed that another length scale has been introduced: that due to chemical reaction behind the lead waves. These waves are no longer thin as in the case of shock waves, and therefore the validity of the self-similarity assumption is questionable (Hornung 1986). Both non-self-similar (Gavrilenko and Prokhorov 1983) and self-similar (Bazhenova et al. 1965) detonation Mach reflections have been reported. Gavrilenko's observations are based on soot foil interpretations. The conclusion of Bazhenova et al. is perhaps more reliable, as it is based on cinematographic schlieren images of the reflection process using a high speed camera. However, their data is limited to two wedge angles in a single mixture, and in the domain of conditions over which such self-similar behavior is obtained is not clear.

More complicated configurations of non-reactive Mach reflections involving additional shock features behind the three main shocks, have also been observed (Hornung 1986). These have been excluded from consideration in detonation Mach reflections by arguing that the local velocities behind the detonations are subsonic (in the triple-point frame). However, some researchers (Bazhenova et al. 1965) have reported observations of such reflections, which suggests that these arguments are incomplete. In the present study, only the basic three wave configuration has been considered, with no consideration given to supersonic flow velocities.

1.1.6 Theories of Detonation Reflection

Theories of shock wave reflection that are readily extended to detonation wave reflection are the 2-shock and 3-shock (Hornung 1986) constructions, and the Whitham's method of shock dynamics (Whitham 1974). These have been carefully compared with measurements in the case of non-reactive shock waves (Bryson and Gross 1961; Henderson 1980; Law and Glass 1971), but such comparisons have not been explored as thoroughly for detonation waves. The basic shortcoming of these simple extensions is that there is no comprehensive incorporation of the actual un-

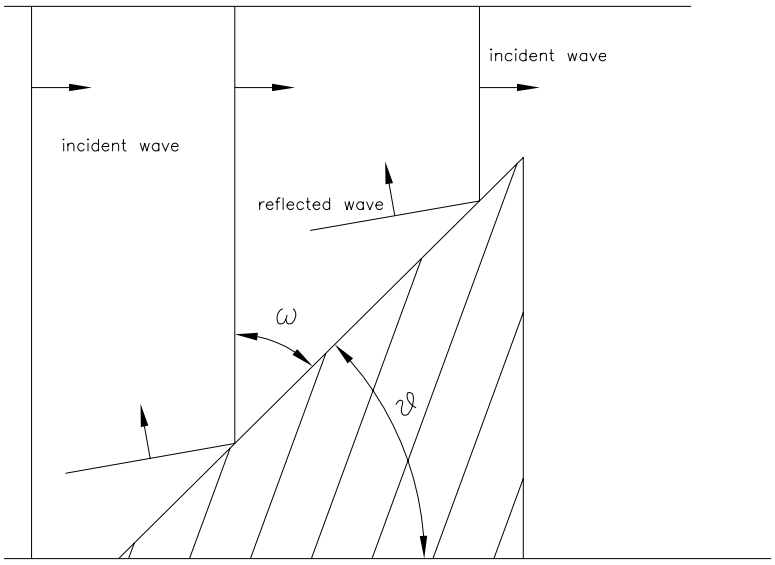

Figure 1.2: Regular Reflection

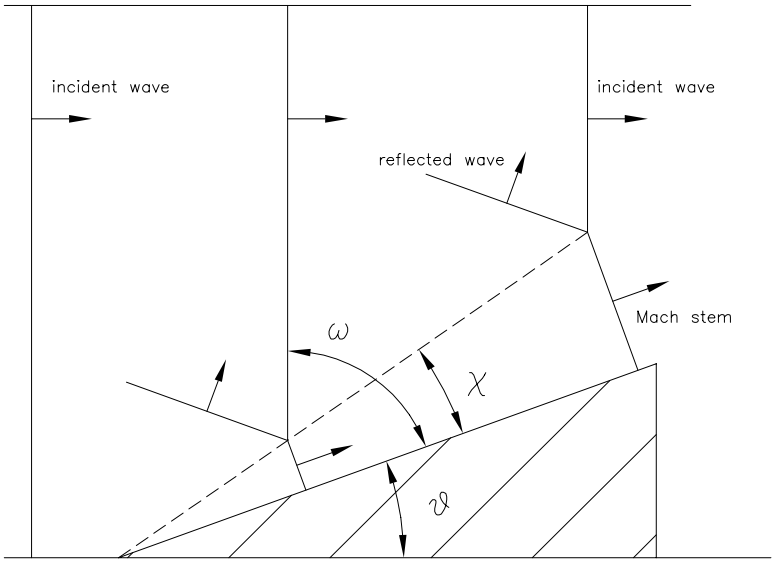

Figure 1.3: Simple Direct Mach Reflection

stable structure of the waves: the detonation wave is treated formally in an average sense. Furthermore, the theories are based on the fundamental assumption of self-similarity of the Mach stem. Therefore, such analyses can be be interpreted to be, at best, effective in the limit of a vanishingly small length scale due to chemical reaction.

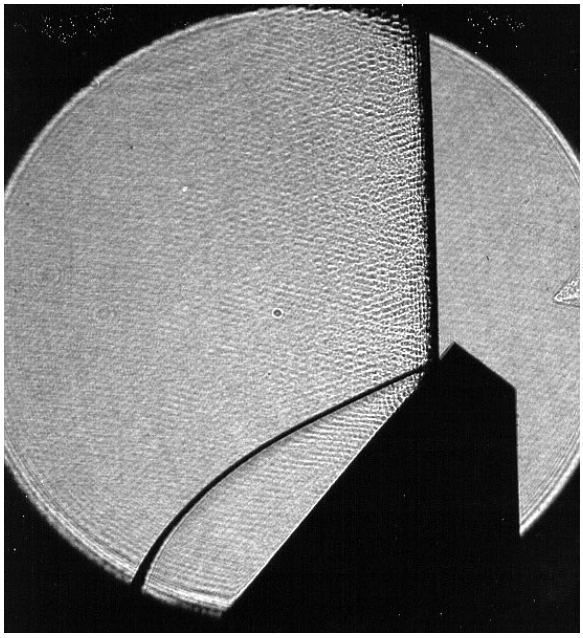

Figure 1.4: Detonation Regular Reflection

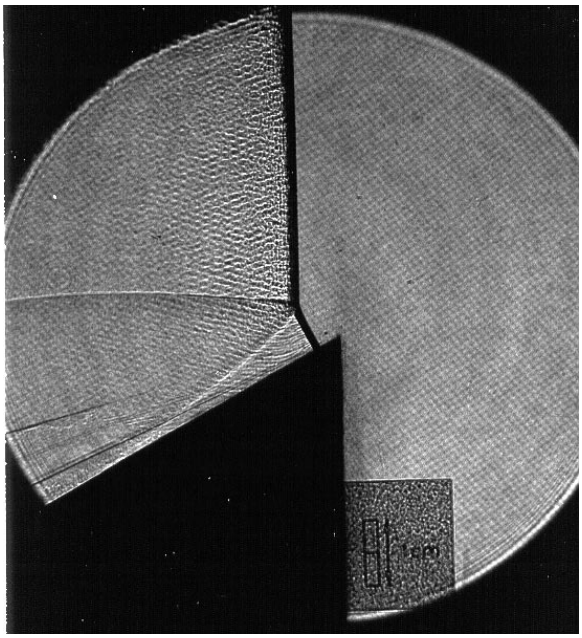

Figure 1.5: Detonation Mach Reflection

1.2 Previous Studies

Amongst previous investigations of detonation Mach reflection, those most relevant to the present study are that of Bazhenova et al. 1965, Gavrilenko and Prokhorov 1983, Meltzer 1990 and Walker 1983. Bazhenova et al. studied CH_4 - $2O_2$ mixtures using spark Schlieren cinematography (high-speed, framing camera). They reported the Mach reflection process to be self-similar. Comparisons between experimentally obtained trajectory angles and reactive 3-shock calculations were also made and reported to be poor. The main shortcoming of the study is that only two wedge angles were studied. Gavrilenko et al. (1983) studied mixtures of CH_4 - $2O_2$, $2H_2$ + O_2 and C_2H_2+$2.5O_2$ at various pressures. Their's was a soot foil study, but χ - θ relations were not reported as they concluded the Mach reflection to be non-self-similar. J. Meltzer studied a $2H_2$ + O_2 at 20 kPa, also using soot foils. Self-similarity of the Mach reflections was assumed, and reactive 3-shock calculations were compared with the measured χ - θ relation. There was disagreement between the theories and the experiment, and the error in the experimental results was thought to be considerable especially at the smaller wedge angles.

The study closest to the present one is that of Walker. He studied mixtures of $2H_2$ + O_2 + Ar, C_2H_2+$2.5O_2$ and C_2H_2+$2.5O_2$ + 11.67 Ar at various initial pressures. Though both soot foils and spark Schlieren were used, the comparison was incomplete as the techniques were both applied to one mixture only ($2H_2$ + O_2 + Ar). Self-similarity was assumed, and non-reactive and reactive 3-shock calculations and non-reactive Whitham theory calculations were made. Good agreement between measurements and reactive theory is reported for C_2H_2 + $2.5O_2$ + 11.67 Ar, but this is based on only 3 points, interpreted from soot foils. The $2H_2$ + O_2 + Ar measurements (χ - θ) seem to lie between reactive and non-reactive three-shock theories but there is considerable scatter data from both soot foils and Schlieren images.

1.3 The Present Work

In this study, the main goal was to obtain clear images of the Mach reflection process, both for qualitative and quantitative analysis. A secondary goal was to

Table 1.1: Average Measured Properties of the Mixtures

Mixture	T (K)	P_0 (kPa)	M_{CJ}	λ (mm)
$2H_2 + O_2$ (mix 1)	295	20	5.1	7 - 8
$2H_2 + O_2$ + 10.33 Ar (mix 2)	295	20	4.8	15 - 18
C_2H_2 + 2.5 O_2 + 14.0 Ar (mix 3)	295	50	5.6	1.75

obtain some soot foil records to compare with the results from the shadowgraphs. The wedge angles (θ) used in the imaging studies were 15°, 20°, 25°, 30°, 35°, 40°, 45° and 50°. Soot foil data were obtained for wedge angles of 20°, 25° and 30°. Values of χ were inferred from the images, for comparison with calculations using three-shock constructs and shock dynamics (reactive and non-reactive). The perceived contours of the leading waves were also obtained from the images. These were scaled with the position of the incident wave in the image, to determine whether the Mach reflection configuration was self-similar within the field of view.

Three different mixtures were used and they are given in Table 1.1. Mix 1 is a stoichiometric hydrogen oxygen mixture, the measured cell size for mix 1 is around 7 mm. However, the cells are not all of the same shape and size (irregular cells). Mix 2 is also a stoichiometric mixture diluted with argon (77.5 %). The cell size for this mixture is found to be about 18 mm, and the cells obtained are very regular. Mix 3 is a stoichiometric acetylene-oxygen mixture diluted with argon (80 %). The cell size for this mixture was about 1.75 mm. The cells for this mixture are also very regular.

Mix 1 was chosen because it had been studied previously within the research group (Meltzer 1990), and the data was available for comparison. Mix 2 provides direct comparison with mix 1 on the basis of an increased characteristic length scale due to chemical reaction (cell size). Mix 3 was chosen in order to obtain data for a much smaller cell size. In addition, the dilution level and initial pressure were chosen to yield a CJ Mach number that does not differ greatly from that of mix 1 and mix 2.

1.3.1 Cylinder Study

Imaging experiments were carried out to observe the reflection process over a half cylinder. The cylindrical geometry gives an opportunity to observe the evolution of regular reflection to Mach reflection, and the subsequent weakening of the Mach reflection through diffraction over the cylinder surface. A half-cylinder (4-inch diameter) was used, and shots were made with the delays set to capture the wave at various positions along it.

CHAPTER 2
Experimental Apparatus and Procedure

All the apparatus used in the experiments is located at the Detonation Physics Laboratory (DPL) of the Graduate Aeronautical Laboratories at California Institute of Technology (GALCIT). The apparatus was built for the experiments.

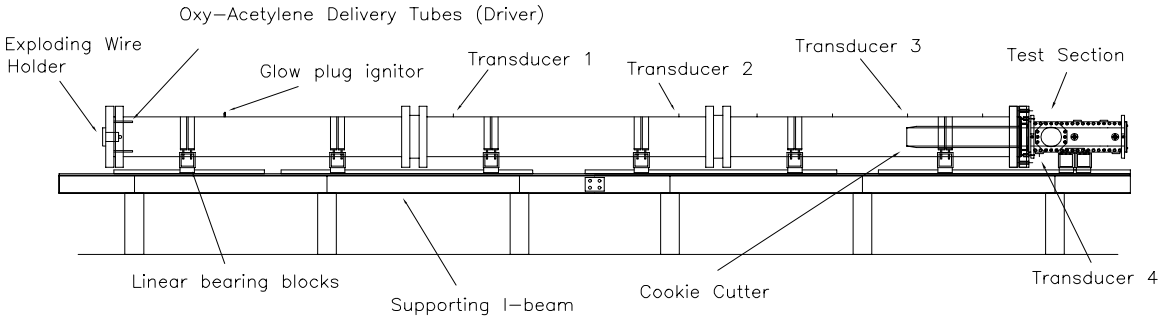

Figure 2.1: The GALCIT Detonation Tube Facility

2.1 Detonation Tube

The GALCIT detonation tube is intended for use in fundamental studies of gaseous detonations. The vessel is designed to contain dynamic, reflected shock pressure loadings of up to 1000 psi (about 68 atm).

The tube sections are made of spin-cast 304 stainless steel honed on the inside to a 63 micro-inch finish. Each tube section is 8-ft long, and has an internal diameter of 11 in. and an outer diameter of 13 in. Each section also has 4 ports for instrumentation or plumbing mounts. Grooves have been cut near the ends of each tube section in order to hold retaining rings that transfer longitudinal forces between the flange and the tube. The flanges and end-plates are 20 inches in diameter and 2 inches thick. They are held together by 1-inch, grade 8 bolts.

The tubes are sealed using O-rings that are retained by rings between the tubes. These contain a face seal (static) with a gland seal (dynamic) for back-up in case of joint movement. End-plates at each end close off the tube in its basic

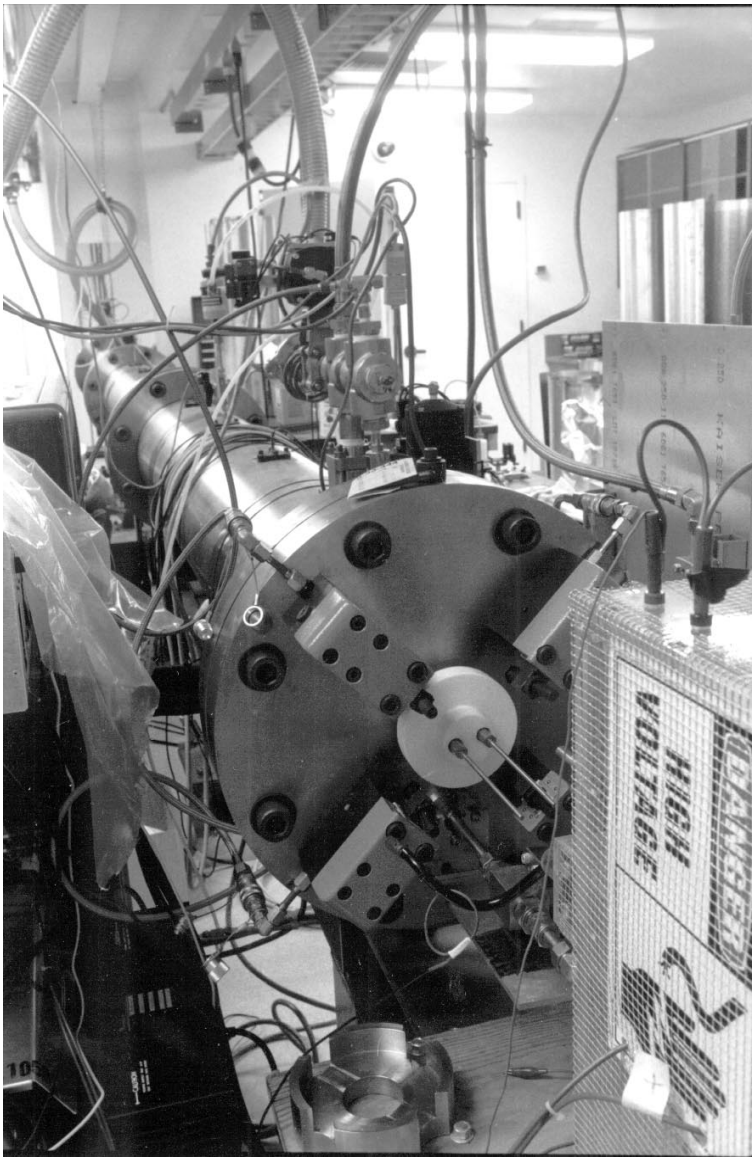

Figure 2.2: The detonation tube as seen from the ignition end, showing the firing plug and holding clamps.

utility mode, but when the test section is to be used a coupling flange replaces an end-plate.

2.1.1 Cookie-Cutter (Wave-Cutter)

For studies of detonation interactions with square obstacles and to facilitate flow visualization a square tube cross-section is required. To achieve this, a 'cookie-cutter' was used to effectively 'cut out' a wave of square cross-section from the

incident detonation wave. The cutter consists of four aluminum plates 1/2-inch thick, welded together to form a 6-inch square cross-section and is mounted inside the end of the last cylindrical tube section. The edges of these plates are sharp, with a 10° wedge angle on the outside only, to 'square-cut' the oncoming wave with minimal disturbance. The cutter is fitted into a 2.75-inch thick holding flange that couples directly with the test-section (Fig. 2.3).

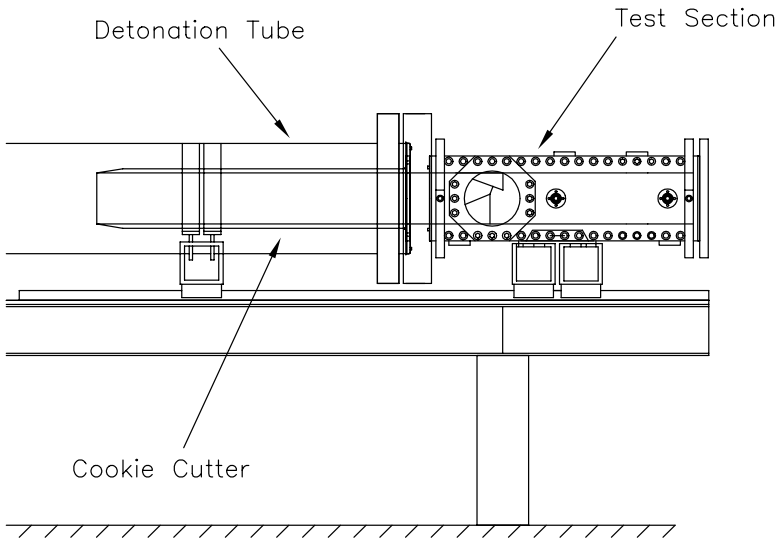

Figure 2.3: Detail of coupling between the main tube and the test-section, showing the cookie cutter and coupling flange.

2.1.2 Test-section

The test-section consists of 2-inch and 1.5-inch plates of 304 stainless steel bolted together to form a cross-section of 6-in. square. It has two in-line circular windows of 6.5-in. diameter. Ports on the top and bottom plates are used for pressure transducers and plumbing connections.

2.1.3 Models

These were made of aluminum and mounted on a large instrumentation mount on the top plate of the test section, using two 1/2 inch bolts and O-ring seals. The maximum exposed height (the back of the wedge and radius of the half- cylinder) was 2 inches. Gaps between the windows and the models were minimized by attaching

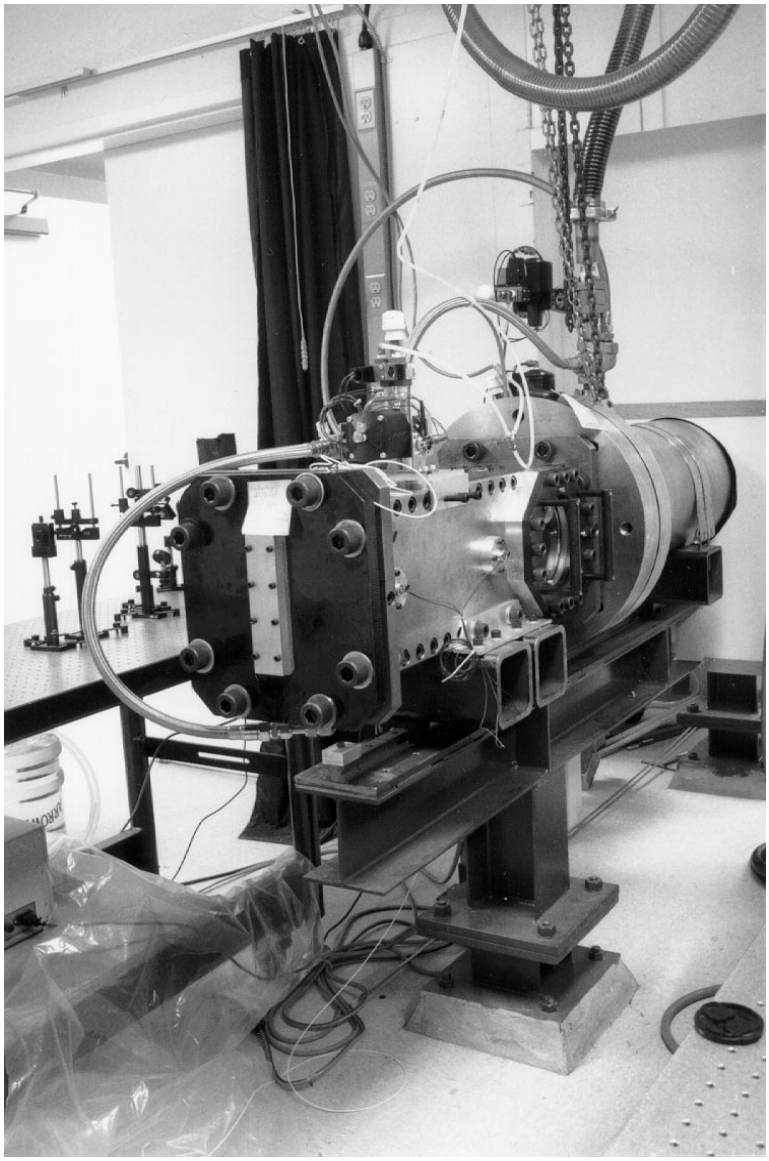

Figure 2.4: View of the Test Section

teflon sheets to the sides of the models. The teflon also mitigated scratching of the windows through any movement of the model.

2.1.4 Fasteners and Seals

The fasteners used in the vessel are grade 8 (high strength alloy steel) bolts. Grade 8 bolts are rated to a minimum yield stress of about 130,000 psi, and ultimate strength of about 150,000 psi. Stainless screws were in some locations where the forces are lower (e.g. port plug fittings). The tube joints, ports and mating fittings

are all sealed using O-rings. These are of a face seal type, with an additional industrial static type seal implemented at joints that are expected to move. The O-rings are made of Buna-N which is inert to mixtures of interest.

2.1.5 Linear Bearings and Tube Supports

Each section of the vessel is mounted on two structural steel square tubes with cut-outs that are shaped to fit the tube surface. The tubes are held down by 0.063 inch thick straps bolted to the structural steel tubes. The structural steel is in turn bolted to linear bearing blocks (THK HSR-35) that travel on sections of high precision rail. This enables the vessel to move freely, as a single unit, about a foot in each direction. The linear bearings are rated for much higher weights than that of the sections, and were also chosen to sustain some moment loading. Vessel travel is limited by aluminum blocks mounted on the ends of the rails.

2.1.6 Hydro-test

The vessel was hydro-tested to 2050 psi (static). Very mild deformation of the retaining rings and grooves was noticed. This deformation is thought to be partly due to a non-uniform loading of the grooves and partly due to excess shear loading of the retaining ring. The flanges were subsequently shimmed to a position that makes for a more uniform loading of the retaining rings. The dynamic loading pressure (conservative estimate) corresponding to 2050 psi is 1025 psi(about 70 bars). This means that for safe operation of the tube, the reflected shock pressure loading should never exceed 1025 psi.

2.2 Operating Systems

To perform a test in the detonation tube, a number of different sub-systems of the facility need to be operated regardless of the nature of the test. These are:

1. Vacuum service
2. Gas handling and isolation valves
3. Firing plug clamping system

4. High voltage circuitry

5. Oxy-acetylene driver

With the exception of the vacuum pump and its heat exchanger, all the equipment of the facility can be operated from the firing station end of the detonation tube.

2.2.1 Vacuum Service

An overhead vacuum line is connected to the detonation tube through flexible hose and by way of electro-pneumatic valves V1 and V2 (Fig 2.5). This vacuum line is connected to a Kinney KTC-112 vacuum pump which can evacuate the facility to around 12 milliTorr, and a pumping time of about 1 hour. Routinely, the pressure is lowered to about 35 milliTorr which takes 15 min. The initial combined outgassing and leak rate of the tube itself is less than 5 milliTorr in 15 min, but the test section and plumbing raises this to about 30 milliTorr in 15 min.

2.2.2 Gas Handling and Isolation Valves

The gas lines come into the laboratory from a bottle farm located outside the building. Provision has been made in the plumbing for a total of seven gases. These are typically hydrogen, methane, ammonia, nitrous oxide, oxygen, nitrogen and argon.

A control panel is mounted on the gas handling rack. This panel contains the switches for the various valves shown in Fig. 2.5, and also has the firing switch for the exploding wire circuitry. Valves V1, V2, T1, T2, E1, E2 and G1 have opto-interrupters mounted on them to sense their open and closed positions. These are linked to indicators on the control panel. The signal lines from the closed position interrupters are fed into a logic circuit that prevents firing unless all valves are in the closed position.

Gases are introduced into the tube by way of a ball valve and a main needle valve (N1) and the desired mixture composition is produced by monitoring the Heise gauge and using the method of partial pressures.

A bellows pump is used to circulate the gas in the tube in order to ensure mixture uniformity. Gas lines are made of stainless steel tubing with compatible

Swagelok fittings and are rated to at least 200 bar (static). The valves are rated (for operation) to a maximum of about 150 bar (static), and should be able to sustain higher pressures before failing.

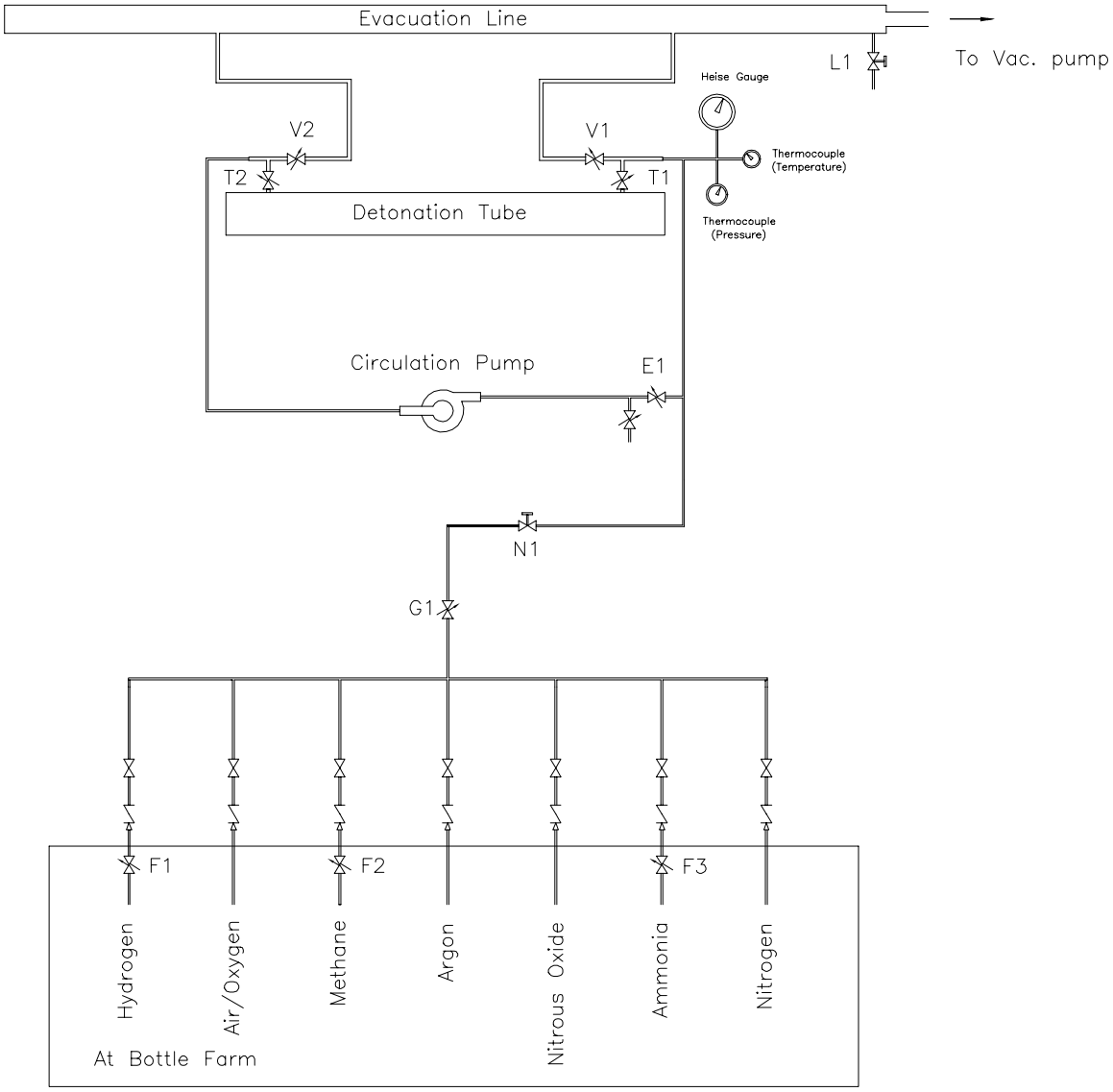

Figure 2.5: Gas handling systems

2.2.3 Firing Plug Clamping System

For operational ease the firing plug can be removed to replace the copper wire. In order to hold this plug in place and be able to sustain pressures experienced during a test, four work-holding clamps (Carr-Lane Roemheld 920-EX) are used as

can be seen in the photo in Fig 2.2. These are operated by a manual pump that raises the pressure in the hydraulic system. The clamping units have arms that first move radially and then axially with respect to the tube. They clamp on top of a stainless steel backing plate that covers the firing plug. This is needed in order to transmit the pressure uniformly to the teflon plug. A force of about 14,000 lb will be experienced by the plug at the maximum operating pressure. The clamps can provide up to a total of 26,000 lb.

2.2.4 High Voltage Circuitry

For direct initiation of detonations, a blast wave is generated inside the tube by exploding a copper wire and producing a rapid electrical discharge. High voltage capacitors (Maxwell) with a total capacitance of 2 μF are charged typically to 9,000 V using a power supply (Hipotronics) with the discharge across the copper wire held off by a spark gap (EG&G GP-20B). The spark gap is triggered by a high voltage pulse from a trigger module (EG&G TM-11). The copper wire is mounted across two copper electrodes fitted on a teflon plug.

The firing circuit is locked out by the logic circuit on the operating panel if any gas handling or isolation valve is not fully closed.

2.2.5 Oxy-Acetylene Driver

To promote the initiation of detonation in the test mixture, a mixture of oxygen and acetylene is injected in the vicinity of the exploding wire just before discharging the capacitors across the wire. Fig 2.6 shows the main elements of the system. Valves A and O are 1/4 inch electro-pneumatic ball valves and valve D is a 3/4 inch electro-pneumatic ball valve. A and O control the gas flow from the acetylene and oxygen regulators respectively, while valve D controls the overall flow into the detonation tube. The controlling circuit opens the valves for a preset time period, and arms and fires the TM-11 a second preset time period after valve D has closed. The time for which the valves are open determines the total amount of oxy-acetylene delivered, for a given regulator setting at the bottles. This is determined before the run and subtracted from the final desired test pressure before determining the partial pressures needed to prepare the test mix. The amount of gas as well as

the amount of time before ignition, both determine the effectiveness of the initiation.

The gases are fed into the tube a single point which then distributes it into four 5 in. long tubes running parallel to the tube axis, but close to the tube wall. Each of these tubes has a series of small holes that enable the gases to be injected radially into the main mixture. Typical regulator pressures are about 15 psi for the acetylene and 24 psi for the oxygen. Comparison of detonation velocity measurements of a typical driver mixture with calculated CJ values showed the mixture to be nearly equimolar (slightly fuel rich).

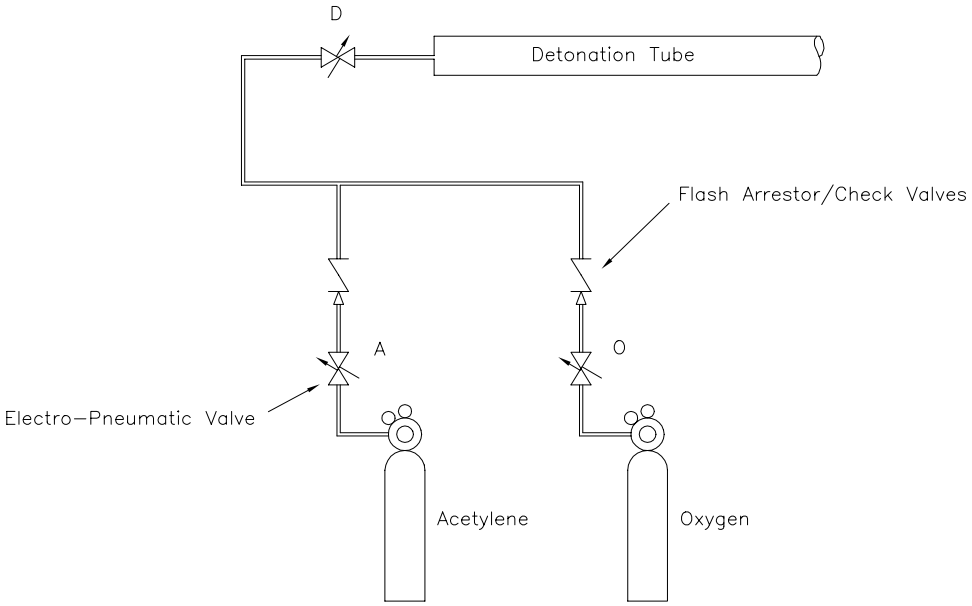

Figure 2.6: Oxy-Acetylene Driver Injection System

2.3 Optics

2.3.1 Ruby Laser

The light source for the shadowgraphs was a Q-switched ruby laser. The basic components of the laser (the ruby-rod and flash-lamp head, resonator mirror mounts, flash lamp power-supply and controller) were that of a used Holobeam 300 welding laser. To be able to Q-switch the inverted cavity, a Pockels cell (Lasermetrics 5016) was used in conjunction with a calcite Glan-laser polarizing beam splitter (Karl-Lambrecht) that had its polarization axis crossed with that of the ruby rod. The

laser was assembled on an optical table (Fig 2.8) and the components were aligned using a He-Ne laser and an auto-collimator. The cavity had a flat rear mirror (99.9% reflecting) and an output coupler of 63.5 cm focal length (35% reflecting). The cavity length was 75 cm. To obtain a clean output, an iris was used to induce the TEM_{00} mode in the cavity. A delay generator (Stanford Research) was triggered by a pressure transducer positioned before the window (Fig 2.10). This delay generator then triggered the Q-switch by sending a pulse to the Pockels Cell driver circuit. Optimal settings for the delays and the flash lamp energy input (capacitor charge voltage) were determined through experimentation. A typical pulse from the laser is shown in Fig 2.7. The characteristics of the pulsed ruby laser are summarized in table 2.1.

Table 2.1: Pulsed Ruby Laser Characteristics

Ruby Rod length = 3 inches	Rod diameter = 0.375 inches
Pulse Width (FWHM) $\simeq$ 50 ns	Optimum Inversion Build-up Time $\simeq$ 1 ms

2.3.2 Optical System

The optical set-up was that of a typical 'shadow' system (Fig 2.9). The main focussing mirrors were of 1 m focal length, and the expansion lens had a focal length of 5 mm. The beam was expanded such that only the most uniform central section fell on the converging mirror M1. The beam path at the output side of the test section was folded to fit into the available space, while obtaining a focussed image. A set-up with M2 focussed outside the test section and a different beam path folding was used in the early shots (see shot 142 photo). This was a more sensitive system, but at the expense of image clarity. The image was about 3 inches in diameter with the object field of about 4 inches.

The camera used was constructed of wood and a 4 in by 5 in film holder. An electronic capping shutter was installed for ease of use. An image quality laser band pass filter was (Andover Corp.) mounted in front of the shutter . This blocked out the light radiation emitted by the reactive flow, and allowed the shutter be left

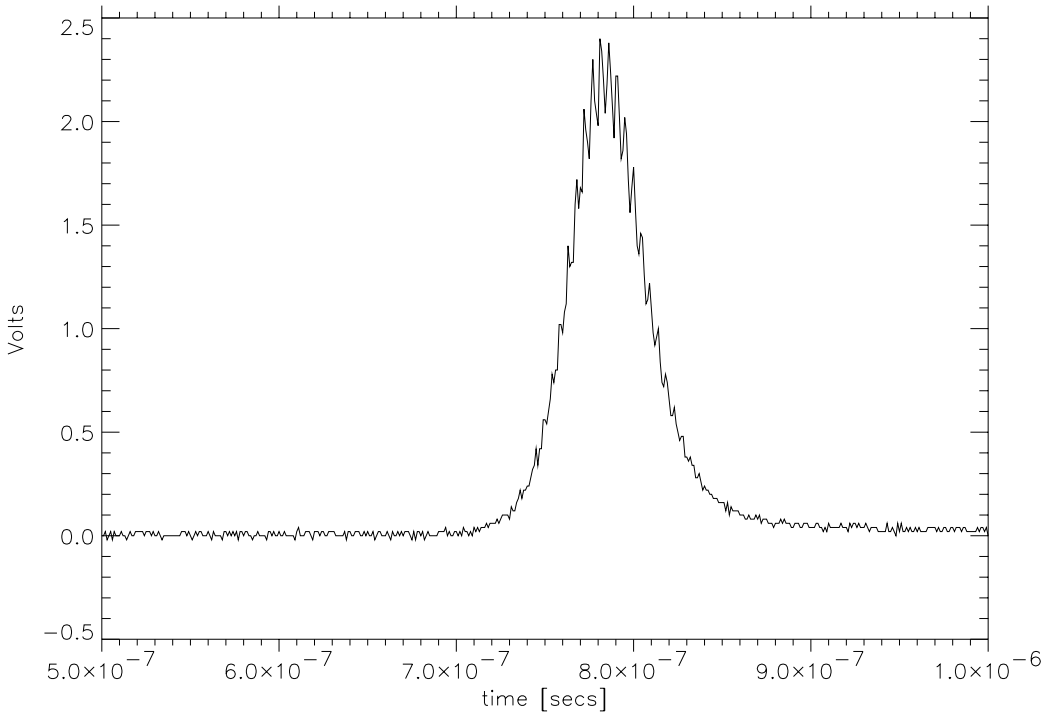

Figure 2.7: Typical photodetector output on receiving a pulse from the Q-switched ruby laser

open for several minutes without appreciable fogging of the film. The film used was Polaroid 667 high speed black and white film (3000 ASA).

A coherent light source such as the ruby laser inherently produces undesirable diffraction and interference in optical systems. To identify the disturbances in the field of view due optical effects as separate from that due to the actual density differences, a reference picture was taken prior to the actual shot.

2.4 Data Acquisition

Records are kept by archiving the pressure traces of each shot from various points on the facility as shown in Fig 2.10. These signals were obtained using pressure transducers (PCB series 113A21, 113A24 and 113A26). The output from the transducers is fed into an optical isolator (H-Tek) which serves to protect the digitizing equipment from the high voltage hazard. The signals were digitized by modules housed in a CAMAC standard crate (DSP Technology). A Sun Sparcstation 5 down-

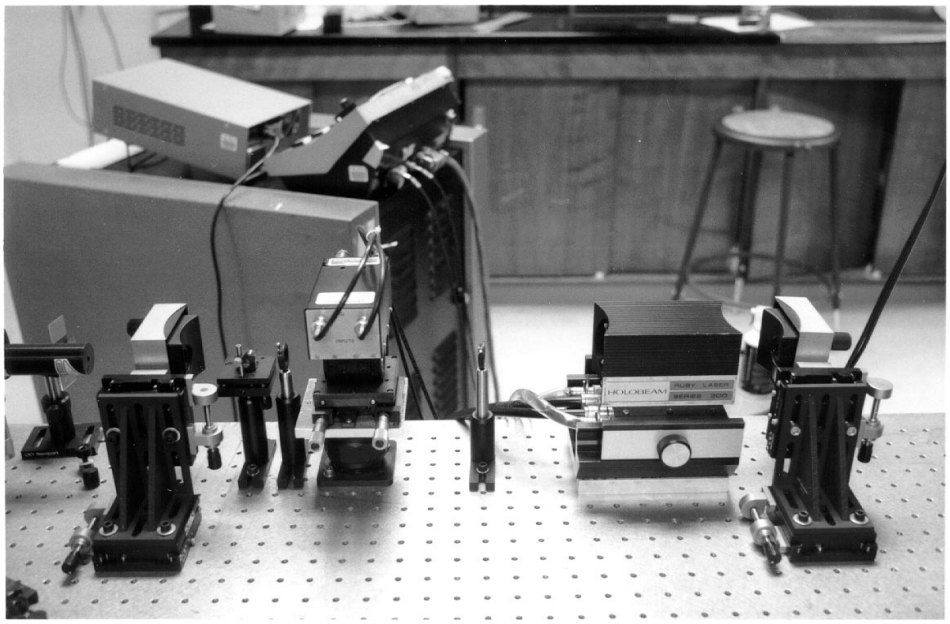

Figure 2.8: The pulsed ruby laser cavity

loads the data from the crate through a GPIP interface bus (National Instruments) and stores it on the internal hard disk in an archival format. PV-Wave graphics software (Visual Numerics) is used to read the files, generate plots and calculate the average speed of the wave between pressure transducer stations.

2.4.1 Shot Timing

In order to capture the detonation wave at a desired position, and obtain the shot pressure traces, a sequence of operations have to be executed with timed precision. This was achieved using delay generators as shown in Fig 2.10. The sequence of events after pressing the fire button are:

1. The laser flash capacitors are charged up.

2. After a 2-3 sec delay, the driver gas charge delivery is triggered.

3. On completion of the driver gas delivery, the driver controller triggers the exploding wire circuit (through the TM-11), the data acquisition, and the delay for the laser flash lamp.

4. The laser flash lamp is triggered after the set delay. This delay depends on

wave speed, and is preset to obtain the optimum exposure for the desired wave position in the field of view.

5. A pressure transducer in the test-section picks up the arrival of the wave and triggers the delay generator for the Q-switch.

6. The ruby laser is Q-switched. The delay between wave arrival at transducer 4 and the Q-switch is set according to the position of the wave desired in the field of view.

Through adequate shot preparation a wave positioning precision of better than 5 mm could be obtained in the field of view.

2.4.2 Soot foils

Strips of cloth, approximately 1-in by 6-in, were dipped in kerosene and placed in a concrete cylinder, which was used as a grate. The foils were clipped to the insides of a roomy carton. The strip was lit, and the carton quickly placed over the flame. The strip burnt out after about a minute, leaving the foils with a fairly uniform layer of soot. Care was taken to prevent the carton from burning, and the foils were only clipped to the its sides to avoid the soot layer from becoming too thick. This method was adapted from the conventional one using a kerosene lamp, as the sooting is faster, more uniform and repeatable. The foils were made of thin aluminum sheet, cut to fit alongside the wedges. Aluminum plates replaced the test section windows in the shots with soot foils.

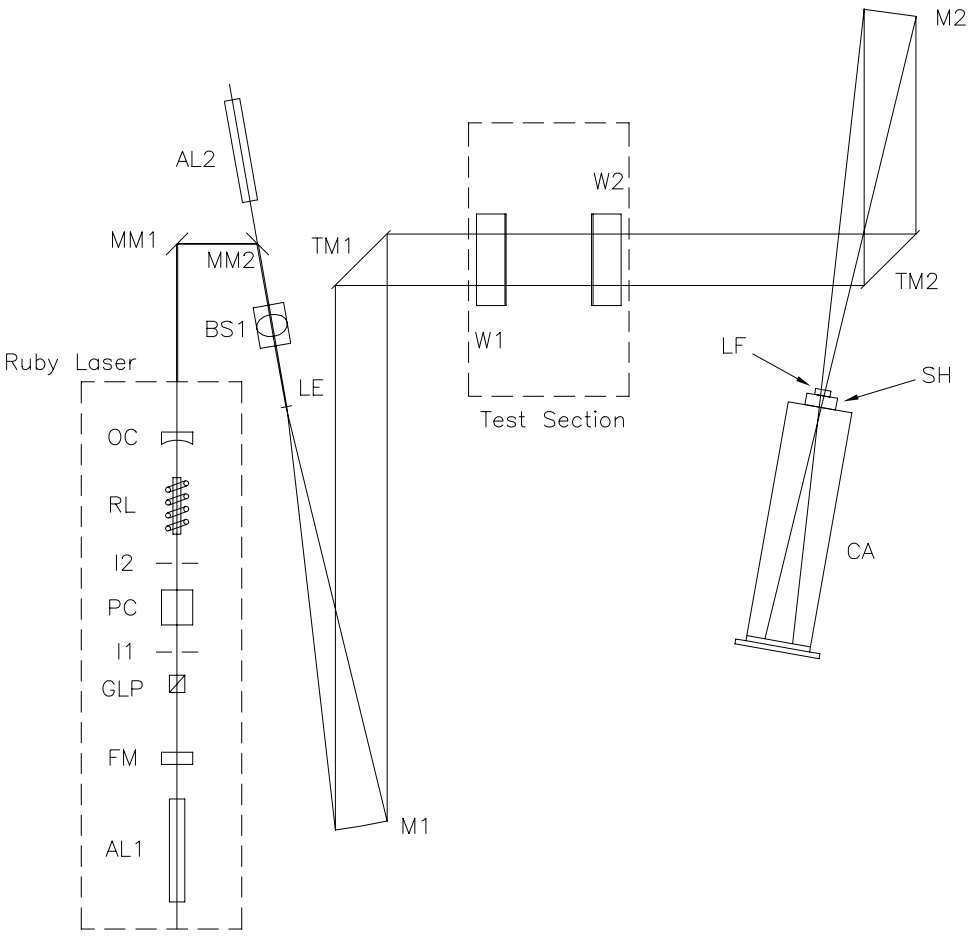

AL1	He Ne Alignment Laser
FM	Rear Cavity Mirror
GLP	Glan Laser Polarizing Beam Splitter
I1	Iris
PC	Pockels Cell
I2	Iris
RL	Ruby Rod and Flash Lamp
OC	Output coupler
MM1	Turning Mirror
MM2	Turning Mirror
AL2	He-Ne Alignment Laser
BS1	Beam Steering Mirror Pair
LE	Beam Expanding Lens
M1	Concave mirror
TM1	Input Turning Mirror
W1	Input Test Section Window
W2	Output Test Section Window
TM2	Output Turning Mirror
M2	Concave mirror
LF	Laser Line Filter
SH	Capping Shutter
CA	Camera with 4X5 back

Figure 2.9: Layout of the Ruby Laser and the Optical System

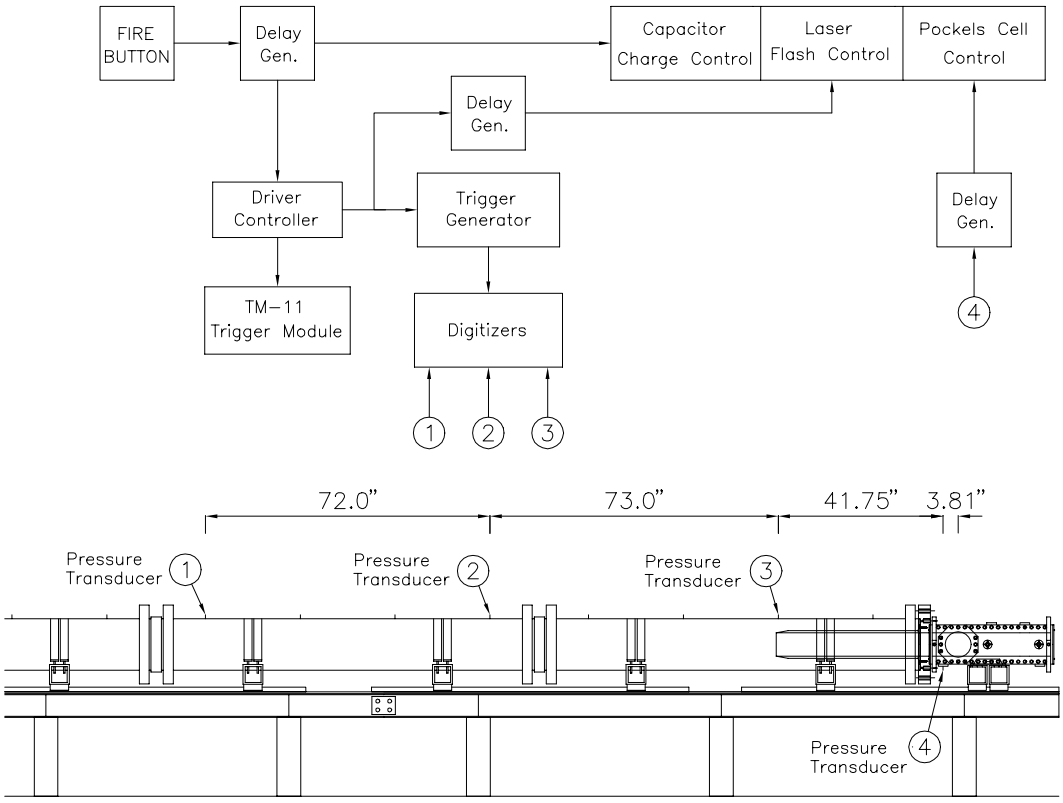

Figure 2.10: Experiment Data Acquisition and Timing Control

CHAPTER 3
Calculation Methods and Data Reduction

3.1 Calculation Methods

All calculations were based on the Chapman-Jouguet model of detonations. The approximation of a constant ratio of specific heats, γ, was also used in the Whitham theory. A comparison between constant γ and variable γ calculations using three-shock theory showed good agreement, lending support to the validity of this approximation.

3.1.1 Constant Ratio of Specific Heats

In this approach to thermodynamic modeling of the exploding gases, it is assumed that both the reactants and the products are thermally perfect gas mixtures. The value of γ was calculated for the products. STANJAN (Reynolds 1986), was used to calculate the equilibrium thermodynamic properties of the products for a Chapman-Jouguet wave in the mixture of interest. Points on the isentrope passing through the CJ point were then calculated for a representative temperature range, using STANJAN, and the value of γ was deduced from the slope of the plot of specific internal energy as a function of the product of pressure and specific volume:

$$e = Pv/(\gamma - 1) + e_0$$

The isentrope was also calculated for shocked reactants with frozen chemistry (no chemical reaction), for each mixture. The frozen ratio of specific heats is denoted by γ_f, and the unburnt ratio of specific heats is denoted by γ_0.

The Chapman Jouguet model using a constant γ is characterized by the following one-dimensional conservation relations (Thompson 1972) across the detonation wave:

$$\gamma P_2 \rho_2 M_2^2 = \gamma P_1 \rho_1 M_1^2 \tag{3.1}$$

$$P_2(1+\gamma M_2^2) = P_1(1+\gamma M_1^2) \tag{3.2}$$

$$\frac{\gamma}{\gamma-1}\frac{P_2}{\rho_2}\left(1+\frac{\gamma-1}{2}M_2^2\right) = \frac{\gamma}{\gamma-1}\frac{P_1}{\rho_1}\left(1+\frac{\gamma-1}{2}M_1^2\right) + \Delta h^0 \tag{3.3}$$

Here the subscript 1 identifies with the reactants and Δh^0 is the enthalpy difference between products and reactants at $T = 0$. It is convenient to define a energy release parameter, Φ as follows:

$$\Phi = \frac{\Delta h^0(\gamma-1)}{a^2} = \frac{\Delta h^0}{C_P T} = \frac{\Delta h^0(\gamma-1)}{\gamma R T} \tag{3.4}$$

Φ was calculated for each mixture by using the value of γ and the CJ Mach number from the equilibrium STANJAN calculations, and numerically inverting the relation:

$$M_{CJ} = \sqrt{(1+(1+\gamma)\Phi) + \sqrt{(1+(1+\gamma)\Phi)^2 - 1}} \tag{3.5}$$

which is obtained by applying the Chapman-Jouguet condition ($M_2 = 1$) to the conservation relations. Values of γ and Φ for the three mixtures are given in table 3.1.

Table 3.1: Perfect Gas Parameters

Mixture	γ_0	γ_f	γ	M_{CJ}	Φ
$2H_2 + O_2$	1.40	1.31	1.12	5.0	5.43396
$2H_2 + O_2$ + 10.33 Ar	1.61	1.52	1.22	4.8	4.72696
C_2H_2 + 2.5 O_2 14.0 Ar	1.61	1.44	1.21	5.6	6.57401

3.2 Reactive Shock-Dynamics (Whitham's Method)

Whitham's method of shock dynamics can be used to calculate the χ-θ relation for shock Mach reflections. It has been previously extended to detonations within the Chapman Jouguet model (Akbar 1991) and is only briefly described here. The key relation is the area-Mach number relation for the wave. This is derived from the solution on a C_+ characteristic in the flow behind the wave (Whitham 1974). The

quasi-one-dimensional equation of motion along this characteristic can be written as:

$$-\frac{1}{A}\frac{dA}{dM} = \frac{(u+a)}{\rho a^2 u}\left[\frac{dP}{dM} + \rho a \frac{du}{dM}\right] \tag{3.6}$$

The right hand side can be non-dimensionalised using $\hat{u} = u/u_0$, $\hat{P} = P/P_0$, $\hat{\rho} = \rho/\rho_0$ and $\hat{a}^2 = \hat{P}/\hat{\rho}$ to obtain:

$$g_d\,(M) = \frac{(\hat{u}+\hat{a})}{\gamma \hat{P}\hat{u}}\left(\frac{d\hat{P}}{dM} + \hat{\rho}\hat{a}\gamma\,\frac{d\hat{u}}{dM}\right) \tag{3.7}$$

The relation between the flow behind the shock wave and its movement is completed through the derivatives in equation 3.7. These are obtained using the conservation equations 3.1- 3.3.

The differential relation is then integrated to obtain the desired area-Mach number relation:

$$\frac{A}{A_0} = \exp\left[-\int_{M_0}^{M} g_d\, dM\right] \tag{3.8}$$

Finally, the formalism of two-dimensional shock dynamics (Whitham 1974) can be used. For wave reflections on a wedge, this yields the following relations for χ and θ:

$$\tan\theta = \frac{(1 - M_0^2/M_W^2)^{1/2}(1 - A_W^2/A_0^2)^{1/2}}{A_W/A_0 + M_0/M_W} \tag{3.9}$$

$$\tan\chi = \frac{A_W}{A_0}\left[\frac{1-(M_0/M_W)^2}{1-(A_W/A_0)^2}\right]^{1/2} \tag{3.10}$$

where M_0, A_0 and M_W, A_W are the Mach numbers and the area values of the incident wave and the Mach stem respectively. A_0 is set to 1 as only the area ratios are considered. The equations 3.9 and 3.8 are solved for M_W, for a given value of θ. The value of χ is then obtained from 3.10.

In contrast to three-shock theory and the physical nature of Mach reflections, shock dynamics theory does not account for the reflected wave (Fig 3.1). This is because the theory is constructed to consider the propagation of a continous front

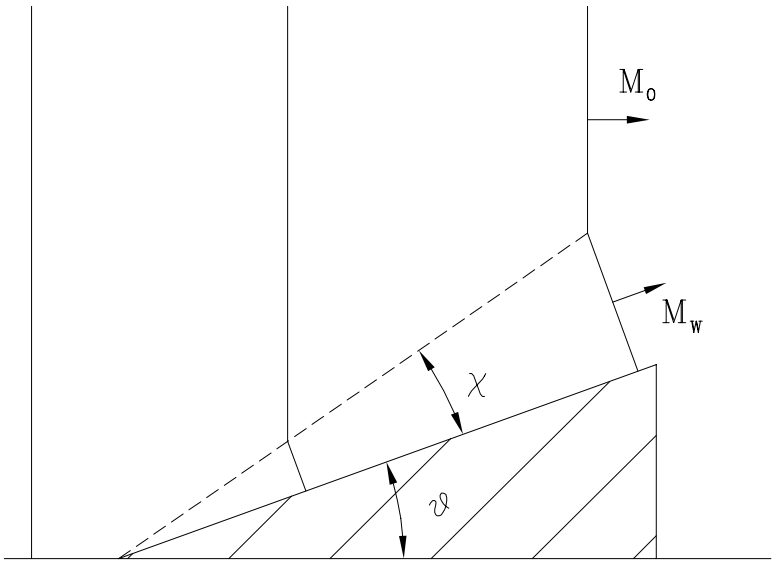

Figure 3.1: Whitham's Shock Dynamics Approximation of Mach Reflection

only.

3.2.1 Three Shock Theory

This is a more direct analysis of Mach reflections in that it involves a reconstruction of the physically observed configuration of waves. The analysis is executed in the vicinity of the triple point, in a frame of reference that is at rest with respect to the triple point. In addition to the one-dimensional conservation relations across each of the waves, constraints that elicit the solution are (Law and Glass 1971):

1. The Mach stem is normal to the wedge and straight between the triple point and the wedge.

2. The pressure and flow angle in the slipstream are matched.

It is convenient to calculate the polars using α the angle between the incident wave and the oncoming flow, in the triple point frame. The calculation was carried out as follows (referring to Fig 3.2):

(a) For a value of the angle α, the hugoniot (pressure and velocity behind the wave for a given normal velocity into the wave) for the Mach stem is calculated for

the range of values of the normal velocity bounded by D_{CJ} and $D_{CJ}/\sin\alpha$. The deflection (δ) is then calculated for each velocity pair and thus the incident polar (P-δ) is obtained.

(b) The polar for the reflected wave is calculated using the state behind the incident wave and a wave angle α_2 ranging from the local Mach wave angle ArcSin($1/M_{local}$) to 90 degrees.

(c) This solution point is graphically obtained as the intersection of the incident and reflected polars. It is the point at which constraint 2 above is satisfied: $\Delta\delta_1 = \delta - \Delta\delta_2$ (i.e. $\delta_1 = \delta_2$) and the pressures behind the waves are matched.

(d) The solution (P_1,δ_1) is used to obtain α_1, the angle the oncoming flow makes with the Mach stem.

(e) By geometry:
$\alpha_1 = 90 - \chi$ and $\alpha = 90 - (\theta + \chi)$.
These yield a χ - θ pair for the value of α under consideration.

Solutions are obtained for only a range of values of α. The lower bound is the Mach solution obtained near regular reflection (when the reflected wave polar actually crosses the zero δ line) as seen in Fig 3.3. The upper bound is where the reflected wave polar is very small and the solution is lost due to imprecision in the calculation (Fig 3.4). For sufficiently low values of θ, the solution near this region of the α range changes over to that with the reflected wave polar *adding* flow deflection to the incident. The flow deflection balance condition then becomes: $\Delta\delta_1 = \delta + \Delta\delta_2$.

3.3 Data Reduction

The shadowgraph photos were digitized through scanning at 250 dots per inch, and their contrast was enhanced to better use the available grey values. The image files (tiff format) were manipulated using PV-Wave software.

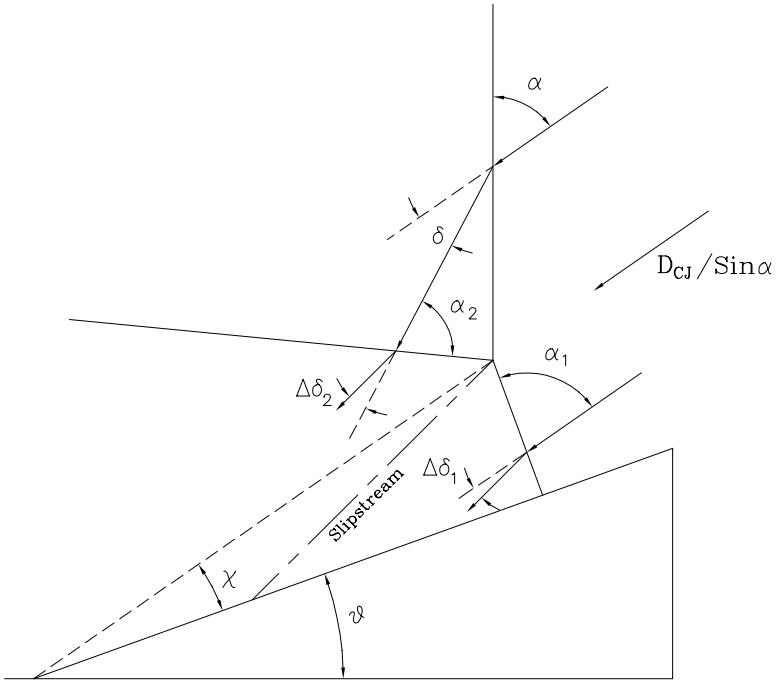

Figure 3.2: Three Shock Analysis

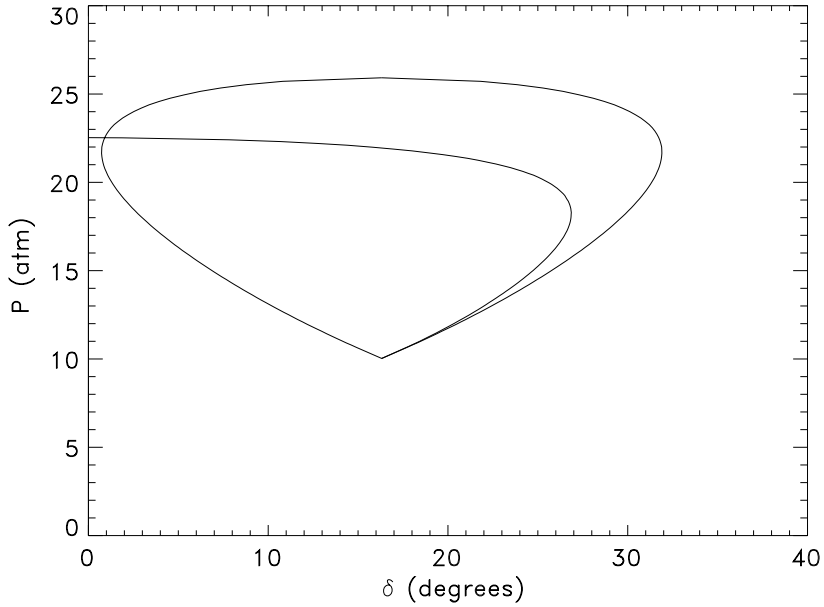

Figure 3.3: Detonation polar behavior near transition to regular reflection (large θ)

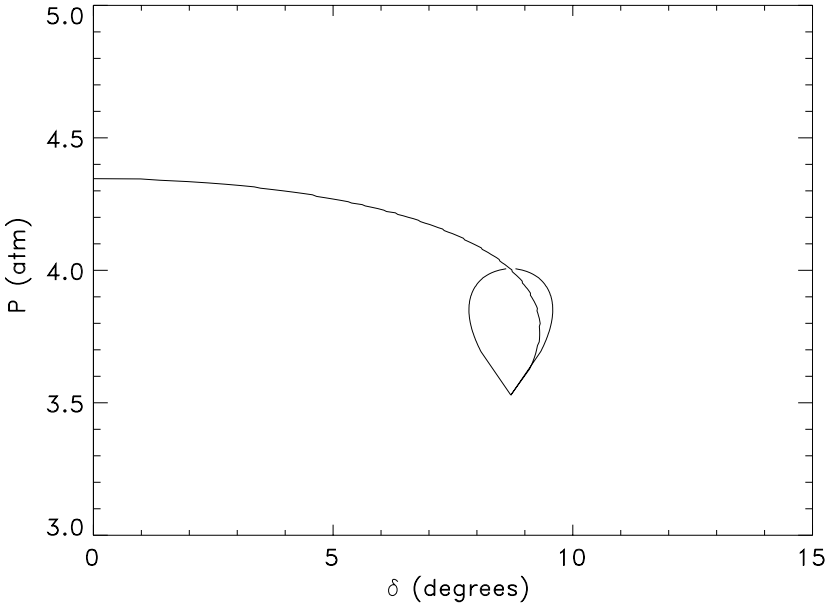

Figure 3.4: Detonation polar behavior for small θ (large α)

3.3.1 Wave Contours

PV-Wave programs were written to obtain the contour of the leading edge of the reflection (incident wave front and Mach stem front) by detecting the gray level of about 30 on a 0-255 scale. Using the scale in the picture and known physical geometry of the wedge, picture coordinates were converted to lab frame coordinates, with the origin at the front apex of the wedge (Fig 3.5). As the front apex is not in the field of view, the rear tip served as the reference point for the coordinate system. These coordinates were then scaled with the travel of the incident wave (Dt) in that image. The transformation collapses contour data from different shots of the same mixture of the same wedge angle on to a single contour, if the reflection process is self-similar (see Fig 3.6).

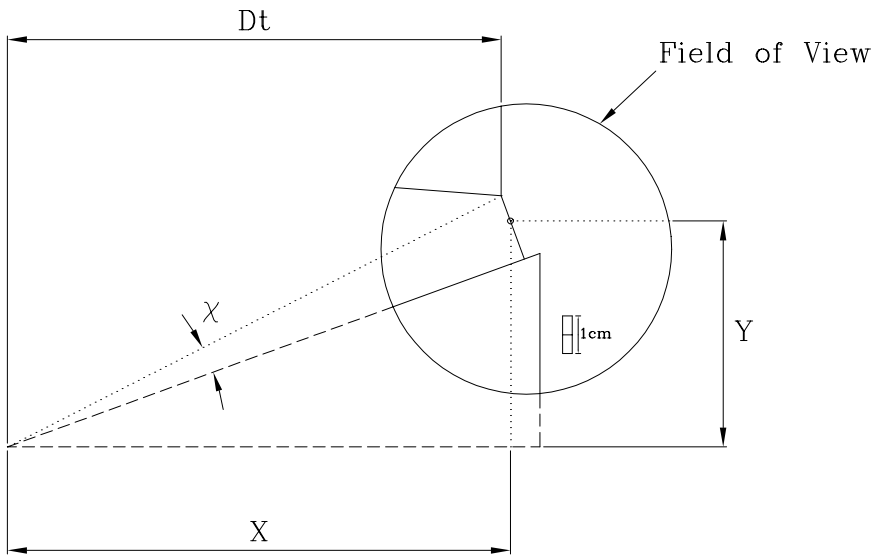

Figure 3.5: Data Reduction Coordinates

3.3.2 Angle Data

The same digitized images were used for the angle data. To obtain χ the wedge surfaces were located by placing points on the edges of the wedge through inspection. The triple point was selected by inspection as well. Given the scale in the picture, the program calculated the position of the Mach stem and a value for χ. When the triple point was not easily discernable, points close to the perceived location of triple point were used. Repeatability of the measurement was within 1/2 degree for a given feature in the image.

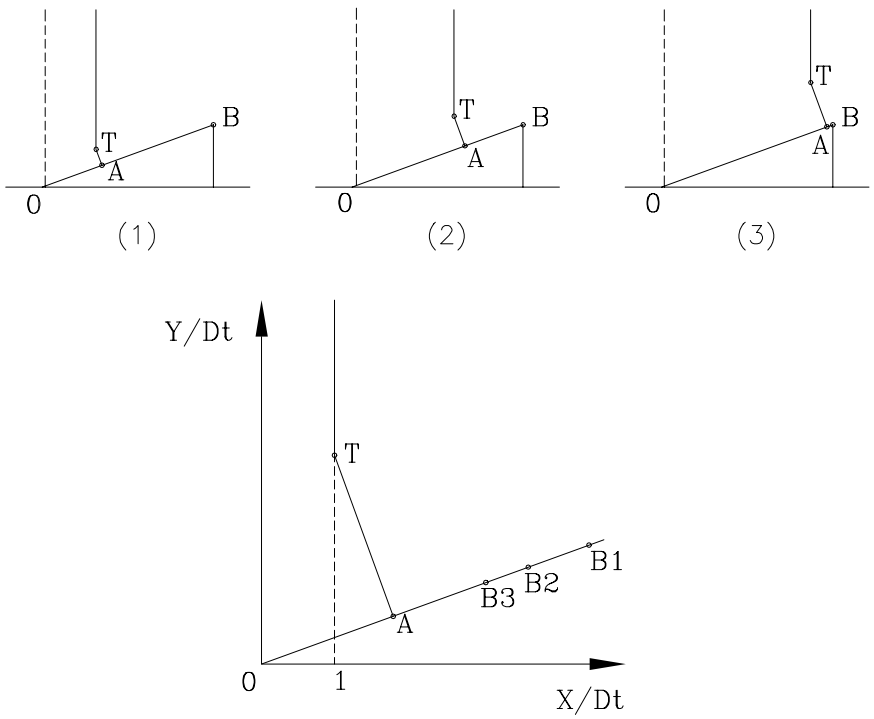

Figure 3.6: Detail of Transformation

CHAPTER 4
Results and Discussion

4.1 Results

Data reduced from the shadowgraph images and soot foils are presented in tabular and graphical form at the end of this chapter. The lists of the imaging experiments are given in Appendix A, with the images themselves given in Appendix B. The corresponding pressure traces are in Appendix C. Specific shadowgraph images that are referred to in the text are presented within this chapter in enlarged form. In all images, the detonation wave is moving from the left to the right.

4.1.1 Prominent Features in the Images

Illustrative examples of details observable in the shadowgraph images are:

- Transverse waves: These are the nearly horizontal lines behind the incident wave in Fig. 4.1 and 4.2, and the faint oblique lines seen behind the wave in Fig. 4.3. The regular spacing between the waves is clearly seen in Fig. 4.1 and 4.2. This spacing compares well with the measured cell widths from soot foils. A much smaller spacing is seen at the foot of the Mach stem, which is to be expected as it is overdriven. This smaller spacing apparently does not extend to the triple point, suggesting that the Mach stem strength varies from the foot to the triple point. It can also be noted, that the apparent transverse wave spacing behind the incident wave persists into the region behind the reflected wave and Mach stem (Fig. 4.1 and 4.2).

- Triple point: The juncture of the three waves is the triple point, as can be clearly seen in Fig. 4.5 and 4.4. In Fig. 4.6, a curved section between the incident wave and Mach stem has replaced the triple point, with the reflected wave apparently detached from the incident wave. If an extension of the curve of the reflected wave towards the front is visualized, the point of intersection of that imaginary curve with the wave front lies lower than the starting point

of curvature change in the incident wave.

- Shear layer (slip stream): This is seen as the faint oblique band, originating at the triple point region, and moving back into the flow between the reflected waves and Mach stem (Fig. 4.4) It is clearly seen in the shadowgraph of a blast wave (Fig. 4.5).

- Curved Detonation: A fully curved front, with no discernable reflected wave can be seen in Fig. 4.7. On close scrutiny, a continuous increase in the transverse wave spacing from the foot of the wave to top is noticed.

- Diffracting Waves: In the cylinder study, the waves can be seen to evolve from a regular reflection configuration, to that of Mach reflection as shown for mix 1 in Figs. 4.8 - 4.12. Comparison between the shadowgraphs for mix 3 and a blast wave case (Figs. 4.15 and 4.16) clearly show the shear layer rolling up into a vortex, in complete contrast with mix 2 (Fig. 4.14). The similarities between the undiluted cases of mix 1 and the driver shot are also noticable (Figs. 4.11 and 4.13). In particular, the triple point region is dispersed and the reflected wave seems to be of diminished strength near this region.

- Complex Mach Reflection: Although this is not addressed in this study, the fact that the reflected wave seems to be straight close to the triple point region and only begins to curve at some length behind it (from the effect of the corner signal) suggests that the flow is supersonic in the slipstream, on the reflected wave side of it (Figs. 4.1, 4.3 and 4.4). This can be compared to the fully subsonic flow behind the blast wave (Fig. 4.5), and a substantially subsonic region behind the detonation in Fig. 4.6.

4.1.2 Velocity Deficits

The velocity deficit is defined as:

$$\text{Velocity Deficit} = (D_{CJ}\text{-}D_M)/D_{CJ}$$

where D_{CJ} is the calculated value of the equilibrium (CJ) velocity of the wave and D_M is the measured value. The measured velocity was determined across the last two transducers, just before the cookie-cutter. The deficit has been calculated for

the shots on the wedge and cylinder studies and identified by mixture type as shown in Fig 4.17.

4.1.3 χ - θ Relations

Comparison plots (Figs. 4.18 - 4.20) have been made for the χ-θ relation for each mixture. The plots show the data from the shadowgraphs, the data reduced from the soot foils, calculated results and the data from the previous work within this research unit (Meltzer 1990).

The data from the shadowgraphs is summarized in Table 4.2. Typically, three shadowgraph images were taken at each wedge angle for each mixture, with the wave at a different position along the wedge. Each image was read three times in order to minimize the uncertainty in the readings and to obtain an average location of the triple point.

There is no data from the 15° wedge shots, as no triple point could be determined from the pictures. For mix 1 and 3, the entire wave was smoothly curved with no discernable reflected wave or Mach stem. For mix 2 (shots 147-149) the triple-point was located outside the field of view, as only the straight Mach stem was captured in the image.

The soot foil data (Fig. 4.3) is less reliable as the foils were usually damaged in the experiment. A single value was used where the trajectory angle was barely observable, and a range was used where significant change was encountered between repeated readings of the foils from the same shot.

In the three-shock calculations, the point of transition from regular to Mach reflection (χ equal to zero) was obtained by linearly extrapolating the χ-θ relation. This value was verified by examining the polars for values of α near that point.

Figure 4.21 summarizes the data obtained from the cylinder study and shows the trajectories of the triple points in coordinates that have been scaled by the cylinder diameter. Also shown is the location of the cylinder surface. Some of the triple points, close to the surface the cylinder, seem to lie *within* the cylinder. This is an error due to the uncertainty in the absolute location of the cylinder from the image. However, the triple-points are well defined in the images, and their relative

positions are more certain.

4.1.4 Wave Front Contours

Referring to the scaled plots (Figs. 4.22 - 4.34), it can be immediately noticed, that the contour of the incident wave (towards the top of the plots) shows a 'stepping'. This is not only due to the protuberances introduced by the cellular structure of the wave (prominent in mix 2 data), but also due to the slight rotation of the image, introduced by the misalignment between the camera and the test section, and by the process of scanning the photograph to obtain the digitized image. The scaled contours of the incident wave and Mach stem are shown in the plots of Figs. 4.23 - 4.34. This data is for wedge angles from 20° to 35°, with the 15° cases given for mix 3 only. The 15° shots for mix 1 were not complete for comparison, and the mix 2 shots at 15° show the wave to be straight and normal to the wedge in the field of view.

The Mach stems are smaller for the larger angles, and could not be captured by the current method of reduction. The scatter in the data is largest for mix 1 because of the uncertainty in the wave front location (a spread of grey values).

4.1.5 Sources of Error

1. There was a gap of about 0.02 inches on each side of the wedge, causing the wave to diffract into it. However, this is not considered significant, as the region is small and the detonation appeared to fail in it.

2. Rotation about axes parallel to the plane of the photo cannot be eliminated. These are possible as the light rays traversing the test section have a finite degree of perpendicularity to the test section. Every effort was made to minimize this and it can be regarded as small.

3. Slight rotation about an axis perpendicular to plane of the photo was apparent in data reduced from the images. This was incurred mainly because the only marks of reference were the wedge tip and the incident wave-front. The wedge angle deduced from the images were all within 1 degree of their actual value and three-point fits of a circle onto the cylinder yielded a maximum of 5%

error on the radius. Future tests should have clear orienting reference marks located in a part of the window undisturbed by the flow-field.

4. Diffraction effects due to finite temporal and spatial coherence of the laser light source are unavoidable in this technique, but were minimized by using a focussed shadowgraph system. These clutter the image, but a 'proof' shot was made before the actual test for comparison.

5. Velocity data in the main tube indicates the shots are highly repeatable, but there is no indication of accuracy. A change in the strength of the driver did not bring about an appreciable change in the measurement of the angles even though a change in the speed was noticed. This provides some support, especially to the mix 1 data, in that the type of measurement being made is relatively insensitive to small departures from the equilibrium wave speed.

4.2 Discussion

4.2.1 Velocity Deficits

It is clear from Fig 4.17, that detonations in mix 1 were still slightly overdriven at the end of the tube, indicated by a negative velocity deficit. This fact is supported in part by the shape of the pressure traces for the mix 1 shots (e.g. Figs. C.1, C.2, C.21 and C.22). However, the following should be considered regarding the data from experiments in mix 1:

1. The calculation of the CJ velocity depends on the choice of species used. This can vary up to 3 m/s.

2. The wave speed was measured across two stations 1.85 m apart. The 1 Ms/s digitizer (10 MHz bandwith) and the 1 μs response time of the PCB pressure transducers, make the timing precision 1 μs, at best. This means that for D_{CJ} of about 2750 m/s, the precision in the velocity measurement is no better than around 5 m/s.

3. The wave enters the cookie cutter after passing the third transducer location. Thus the measured wave speeds are for the main tube only. The effect of

increased wave confinement, with no decrease in the effective area in a ray-tube sense (Whitham 1974), makes losses on the wave solely due to boundary layer effects. These are greater in the smaller cross-section of the cookie cutter, thus the wave is expected to approach CJ more rapidly.

For these reasons, we do not consider that the detonations in mix 1 to be sufficiently overdriven to be a major concern. However, this problem still remains from being completely resolved. Shots conducted at higher pressure show the wave to be overdriven between the last two transducers, even though the cell size is much lower- which should have made the wave approach CJ more quickly.

4.2.2 Self-Similarity and Triple Point Trajectories

A brief outline of some basic guiding notions is useful at this point. As mentioned in the introduction, the fundamental assumption utilized in both the calculations and experiments is that χ is a constant, i.e. the Mach reflection is self-similar. In other words, there is no length scale in the problem except for the position of Mach reflection configuration, as measured from the apex of the wedge- the assumed origin of the growing Mach stem. This assumption is questionable if an independent length scale exists (Hornung 1986). Such an independent scale is obtained in detonations, due to the interaction of chemical reaction with the gas-dynamics. The length scale can be conveniently represented by the mixture's intrinsic detonation cell width, λ, but could be equivalently represented by the apparent thickness of the wave (called the hydrodynamic thickness) and perhaps more interpretatively represented by a calculated ZND reaction zone thickness. The value of λ can then be compared to the position of the incident wave, L, (Fig. 4.35) to characterize the interaction after Sandeman et al. (1980):

Small L/λ : The extreme value would be zero- corresponding to frozen chemistry. The calculations expected to compare favorably with the experiments in this regime are the non-reactive 3-shock and Whitham theories. The region on the wedge corresponding to this regime can be regrded as the near field with respect to the origin of the interaction (the wedge tip).

Large L/λ : The extreme value would be infinite, corresponding to a negligible reaction zone. In this regime the reactive 3-shock theory and reactive Whitham theory would be expected to compare favorably with experimental observations. The corresponding region on the wedge is considered to be the far-field.

Intermediate L/λ : The special value would be 1. In this regime neither frozen nor reactive analyses would be expected to apply. The corresponding to this region on the wedge is then referred to as the intermediate field, or the transitional region.

Although the position of the Mach reflection changes within the field of view, the field of view itself does not change between mixes, for a given wedge. Thus, for a given wedge length, the mixtures can roughly be characterized relative to each other. Mix 3 would then be expected to fall in the first regime of effectively reactive flow behavior, mix 2 could be considered to be in the regime of effectively frozen flow behavior, and mix 1 would most likely lie in the intermediate regime. More precise considerations involves the inclusion of the actual locations of the incident wave, in each image. This is treated, approximately, in the following section.

4.2.2.1 Wave Front Contours: Self-similarity

Except, perhaps, for the mix 1 case of 30° (Fig. 4.29), the scaled similarity plots suggest that the Mach reflection process is self-similar, *within the field of view of the optical measurement*. This assertion is made because the apparent shape of the Mach stem is seen to be similar for a given wedge, and the contours collapse on top of one another, within the differences attributed to the technique. A particularly strong result is the collapse of the mix 3 contours for θ equal to 15° (Fig. 4.22), as the wave is completely curved in this case.

The reason for the slight change in shape that can be noticed in the mix 1 case of 30° wedge angle is not entirely clear. This change is also noticable in the shadowgraphs used for the plot (see shots 172 and 170 in Appendix B). Some insight into this effect is gained by considering the characterizing parameter L/λ. The value of L can be approximated by the horizontal wedge length, as the rear tip of every wedge was located near the center of each image. Values of L/λ, so obtained, are

given in Table 4.4. It should be noted that the incident wave travel *decreases* with wedge angle, i.e., the wave travel is greater for smaller wedge angles, simply because the wedges had the same height at the back, which was approximately at the center of the field of view.

It can be immediately noticed from the table that, over the range of wedge angles, L/λ is large for mix 3, is small for mix 2 and, in the case of mix 1, lies between the largest mix 2 values and smallest mix 3 values . In the special mix 1 case of $\theta = 30°$, L/λ has a value of about 11. This happens to be the largest L/λ for mix 2, and the Mach stem (see shots 148 and 149 in Appendix B) indeed exhibits a slight curvature. Furthermore, the shadowgraphs and the similarity plots for mix 1 cases of L/λ larger than 11, all show the incident wave and the Mach stem to be one, smoothly contoured, lead wave. This is also true for the case of mix 3, with the only difference being that the curved region apparently shifts towards that triple point for larger wedge angles. Thus a fundamental character of the detonation Mach reflection seems to suggest itself: a curved wave is obtained for small values of θ *and large enough travel along the wedge*. Furthermore, the Mach reflection appears self-similar in the field of view, if in the apparent near field or in the apparent far field, and seems to change in shape, losing its geometric similarity, in the intermediate field. Whether or not the triple point trajectory changes as the Mach stem acquires curvature is uncertain at this point, and it may be that the effective radius of curvature continues to grow linearly with distance, with the same trajectory followed by an effective triple point. More work is needed to confirm and quantify the apparent change in shape. The obvious experiment would be to clearly image the detonation within each L/λ regime, on a single wedge.

A sense of the magnitudes involved in the similarity plots can be obtained by noting that, for example, in the 30° case, the incident wave travel is bounded by the wedge length, which was 87 mm. Thus, 0.01 on the abscissa of the plot corresponds to about 0.87 mm. Also, in the approximately 50 ns exposure of the laser pulse, the wave travels 0.14 mm. Typical precision in locating the contours of the waves was about 0.2 mm.

4.2.2.2 χ - θ Relations

The following observations are made based on the triple-point data comparison plots (Figs 4.18 - 4.20):

1. In Figure 4.18, the present mix 1 soot foil data is seen to be fairly consistent with the previous study (Meltzer 1990), given the uncertainty in the soot foil technique. This is despite the fact that Meltzer's facility had a smaller cross-section and consequently a velocity deficit.

2. The angle of transition from regular to Mach reflection is underpredicted by the reactive three-shock theory, which is consistent with previous studies (Meltzer 1990; Walker 1983; Bazhenova et al. 1965). In particular, the value is estimated to be between 45 and 50 degrees for mix 1. Meltzer obtained a value of 45 degrees using the soot foil technique.

3. For mix 1, values of χ inferred from the soot foils are larger than those obtained from the shadowgraphs for small values of θ. This is not as clear for mix 2, and is completely uncertain for mix 3.

4. There is clear disagreement between all of the calculated χ-θ relations and the measurements for mix 1 and mix 3. For mix 2, there is reasonable agreement between the non-reactive 3 shock calculations and the measurements.

The first two points are given only to indicate consistency between the present and previous data. The last two points are further discussed below.

Soot - Shadowgraph Discrepancy: A possible explanation is obtained through the consideration of the strength, and therefore the speed, of the reflected wave compared to that of the transverse waves in the early part of the reflection process. For small θ, the reflected wave is weak. This is because the flow deflection that is needed is small. Thus, the reflected wave is closer to being an acoustic pulse. On the other hand, the transverse waves are typically travelling between 1.1 and 1.3 times the local speed of sound (Strehlow 1969), and will overtake an acoustic pulse moving laterally across the incident wave. Since, χ is obtained from the soot foils by following the track of the transverse wave seperating the smaller sized cells

(presumed to be entirely from the Mach stem) from the larger ones (presumed to be entirely behind the incident wave), the value obtained is larger than the actual triple point angle. This could explain the discrepancy between the between the soot foil data and the shadowgraph data for mix 1. More data and careful comparison are needed to address this issue for mix 2 and mix 3.

Calculations vs. Experiment: The exceptional agreement between the non-reactive 3-shock theory and measurements in mix 2 is probably due to the flow being close to the effectively frozen regime. The flow is definitely not frozen (that would only be true for an extremely small distance along the wedge), but, it may be that the dynamics of the reflection are still being determined by the interaction of the lead shock and reflected wave within the region ahead of the reaction, where the flow variables are in the so-called Von-Neuman point (Fickett and Davis 1979). Experiments using wedges that are long compared to the cell size of mix 2, to obtain all three types of region, are needed to resolve this matter further.

The contrasting case of mix 3 should lie in the fully reacted regime, however agreement between the reactive 3-shock theory and reactive Whitham theories is poor. This counter-intuitive result, suggests that these simple CJ extensions and associated arguments might be inadequate. This is especially true for reactive three-shock theory, as the similarity investigations show that wave to be self-similar within the field of view, with an effective origin at the apex of the wedge. For large values of θ, the measured χ - θ relationship seems to approach the reactive Whitham theory, but not in a definitive manner.

Mix 1 experimental results are similar to that of mix 3, in that they are also not in agreement with any of the theories. There is a weak trend towards the reactive Whitham theory as the wedge angle increases. It is difficult to make any assessment of the theories, as the intermediate regime under which mix 1 is categorized is not well defined. Furthermore, mix 1 exhibited self-similar behavior for most values of θ, as discussed previously.

4.2.3 Cylinder Study

The main result here suggested by Fig. 4.21 is that the triple point trajectories are de-lineated by Mach number. The rise of the triple point from the surface of the wedge is the greatest for the lowest Mach number case of mix 2. This was also substantiated by shots using the driver mix, which have a Mach number of about 8, as can be seen by comparing Figs. 4.12 and 4.13 which have the waves at approximately the same position on the cylinder.

4.3 Tentative Conclusions

Based on the previous analyses, and the inspection of the shadowgraphs, some tentative conclusions can be made. The strongest among these, is the one suggested earlier: in the Mach reflection process, the Mach stem may be straight in the early part of the process, developing curvature as it proceeds along the wedge. The exceptional agreement between the χ- θ experimental results for mix 2 and the corresponding calculations based on non-reactive theory is probably because we are observing the early stages of Mach reflection. This should evolve into a curved wave for a long enough wedge and not too large θ, as is noticable for $\theta = 15°$. At present it is unclear whether the triple-point trajectory itself will change for any of the mixtures.

Another observation that requires further study and quantification is the apparent modification of the triple point region as the reflection proceeds down the obstacle. This is conjectured to be due to the deterioration of the reflected wave by the action of the transverse waves, moving down into the vicinity of the triple-point from behind the incident wave, as can be seen in shadowgraphs, especially in the cylinder shots. However, the dispersion of the triple point region is clearest in the mix 1 shots, and much less noticable in the mix 3 shots. Why this is so is not certain at present. One reason for this may be that the much more regular cells of mix 3 make the flow field much less cluttered in the line of sight, such that the shadowgraph obtains greater sensitivity. Another contributing factor may be the relative power involved in the local cyclical explosions that are effecting the triple-point region. The importance of the local explosion intensity is suggested by the

striking similarity between mix 1 and the driver mix, seen in Figs. 4.11 and 4.13, inspite of λ being much smaller in the driver mixture.

The transformation of the triple-point into a smooth curve, and the associated deterioration of the reflected wave could result in a distributed compression region replacing the reflected wave, to provide the neccessary flow turning and maintain the pressure difference behind the incident wave and Mach-stem. This is similar to that reported to occur in weak shocks (Collela and Henderson 1990).

A possible interpretation of the 'evolving dispersion' of the sharp kink at the triple point may also be obtained by considering finite reaction zone effects in the leading waves, as calculated by Bdzil et al. (1996), for solid explosives. This ignores the cellular structure of the detonation, treating it as shock followed by a reaction zone of prescribed dynamics and is an extension of shock-dynamics applied to detonations. The main features of the flow were obtained by Bdzil et al., and in particular a distributed compression wave region occured in their simulations of Mach reflection.

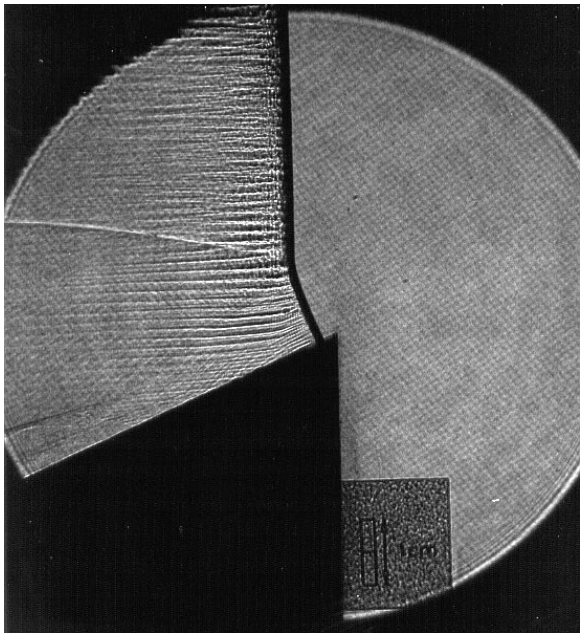

Figure 4.1: Shot 168: mix 3, 25° wedge.

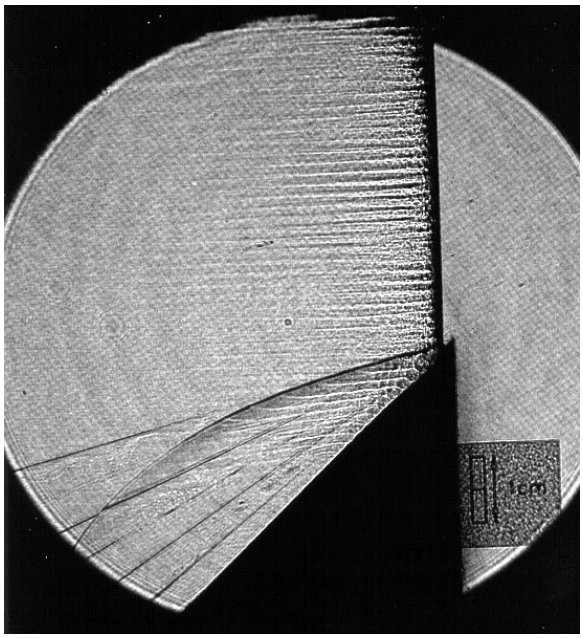

Figure 4.2: Shot 198: mix 3, 45° wedge.

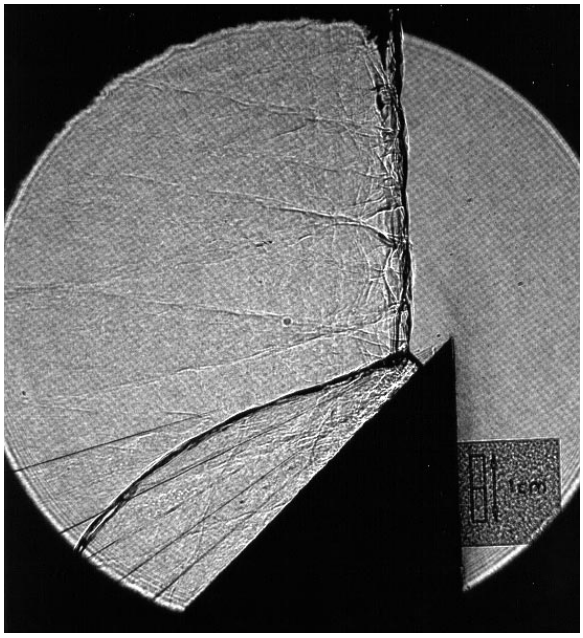

Figure 4.3: Shot 199: mix 2, 45° wedge.

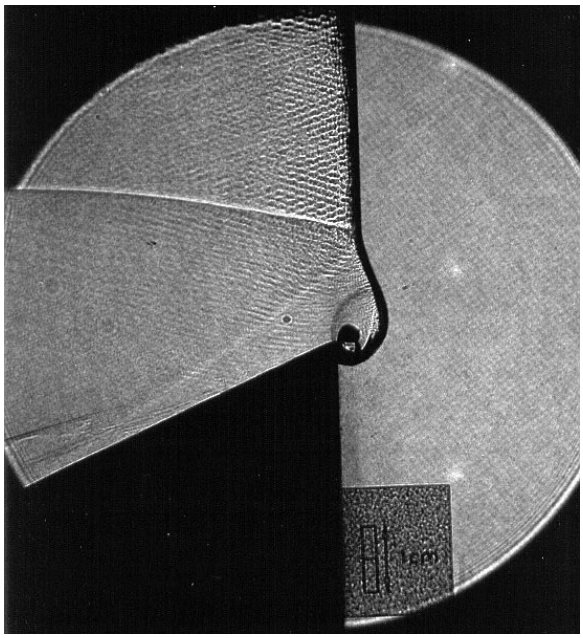

Figure 4.4: Shot 169: mix 3, 25° wedge.

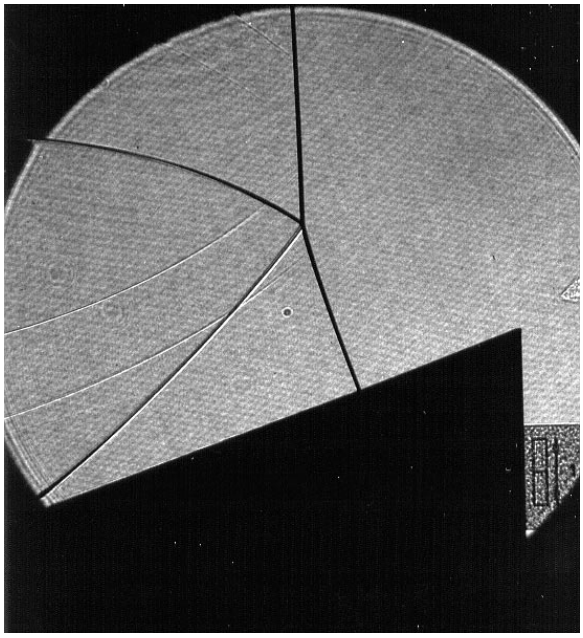

Figure 4.5: Shot 224: air blast, 20° wedge.

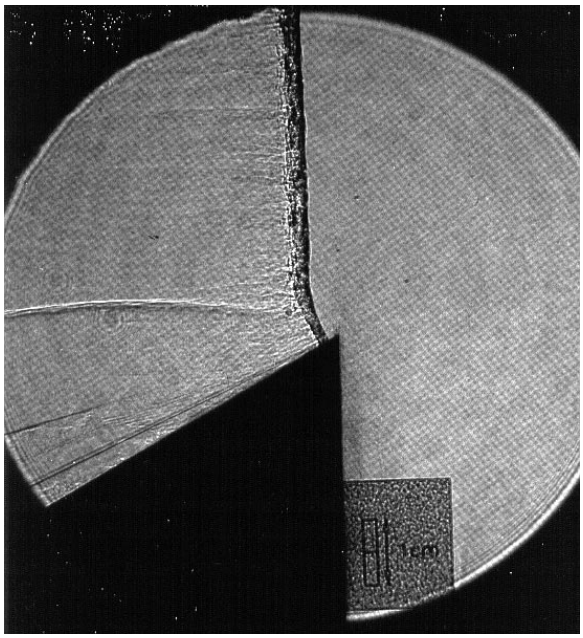

Figure 4.6: Shot 170: mix 1, 30 ° wedge.

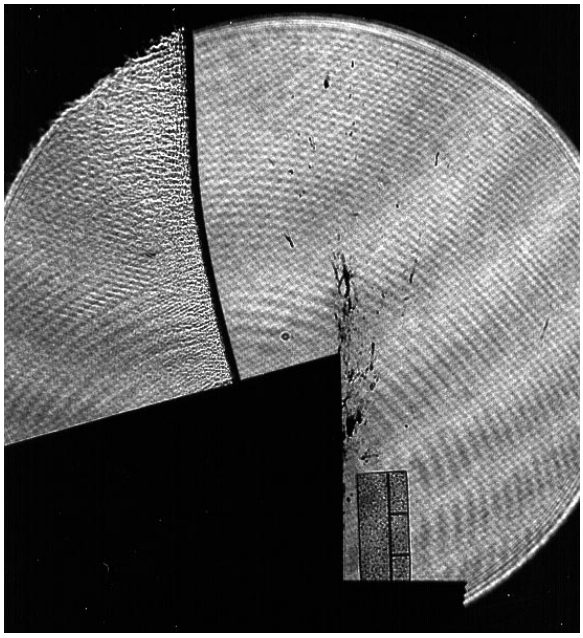

Figure 4.7: Shot 154: mix 3, 15° wedge.

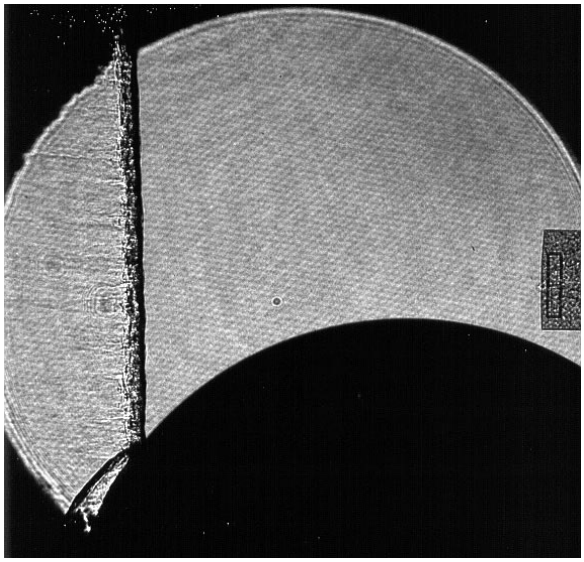

Figure 4.8: Shot 228: mix 1.

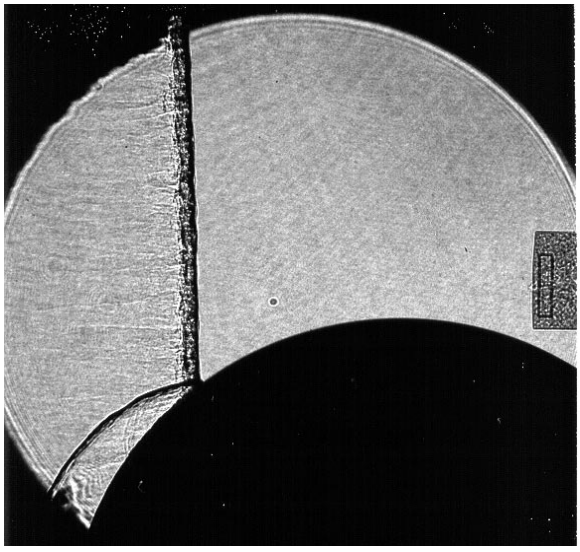

Figure 4.9: Shot 227: mix 1.

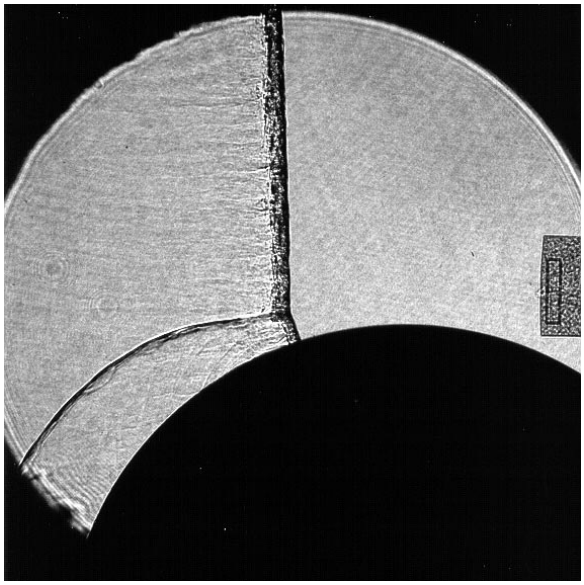

Figure 4.10: Shot 229: mix 1.

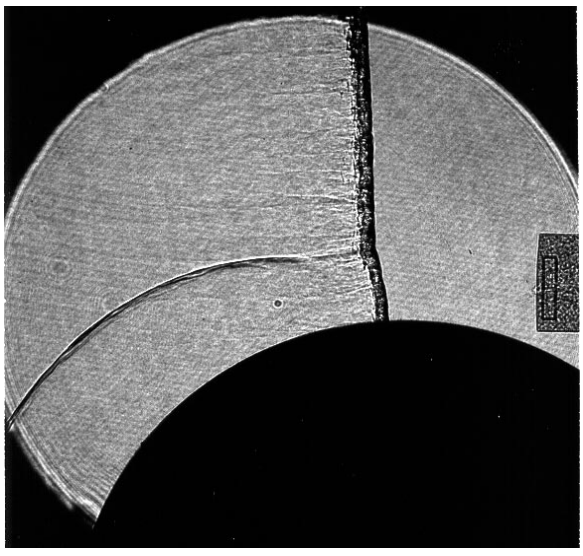

Figure 4.11: Shot 226: mix 1.

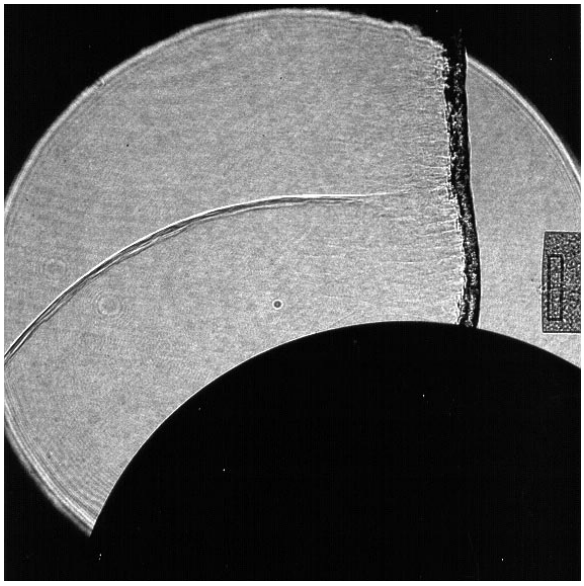

Figure 4.12: Shot 230: mix 1.

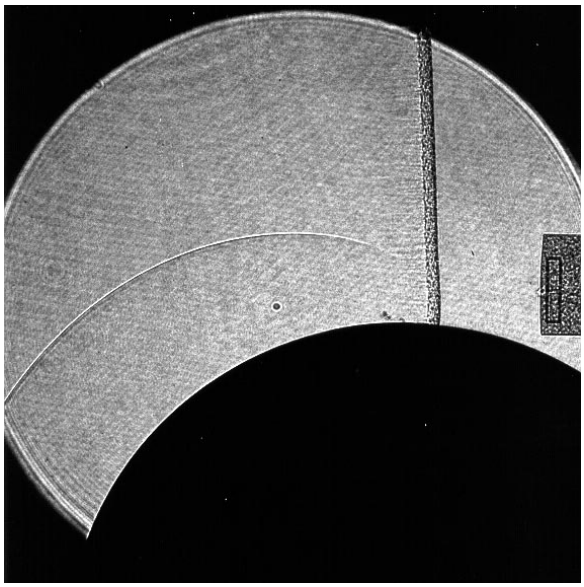

Figure 4.13: Shot of driver mixture (approx. 1.25 $C_2H_2 + O_2$)

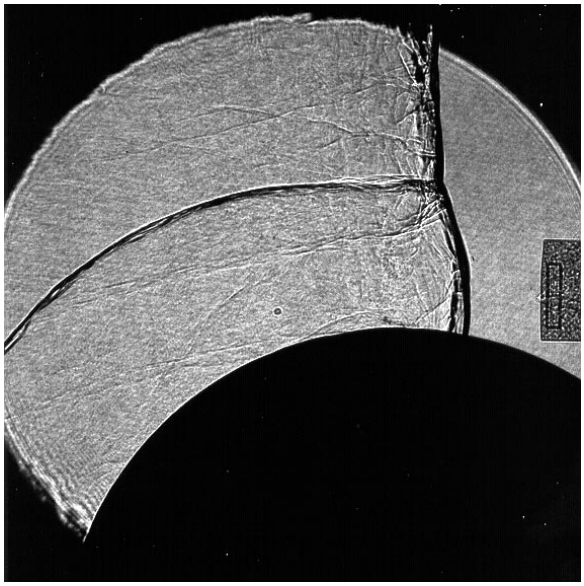

Figure 4.14: Shot 241: mix 2.

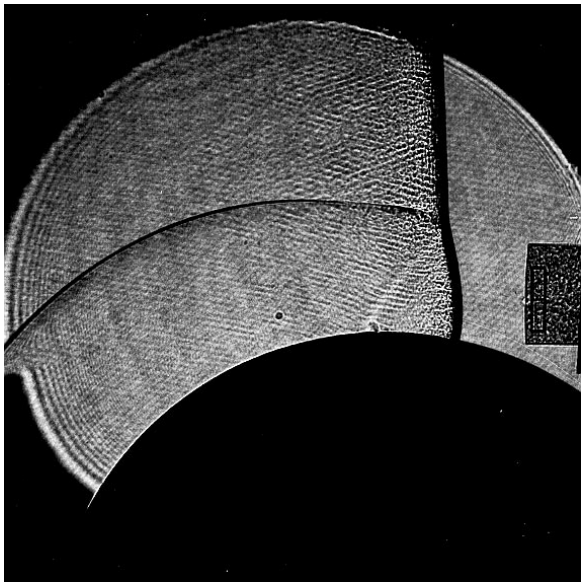

Figure 4.15: Shot 255: mix 3.

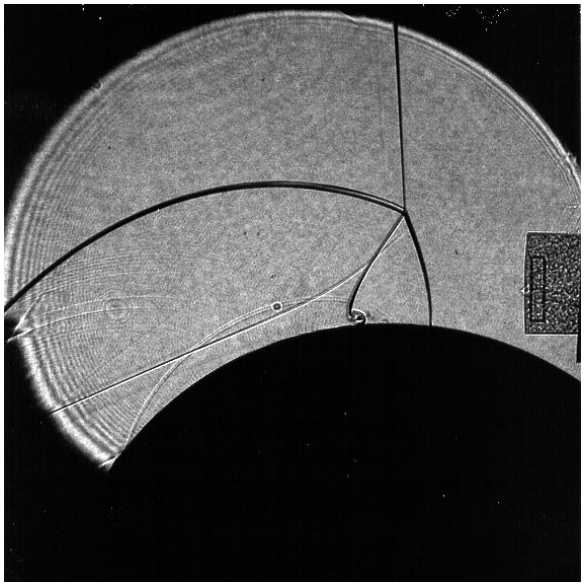

Figure 4.16: Shot 254: air blast wave at 1 atm.

Table 4.1: Average Measured Properties of the Mixtures

Mixture	P_0 (kPa)	D_{CJ} (m/s)	λ (mm)
$2H_2 + O_2$ (mix 1)	20	2757	7 - 8
$2H_2 + O_2 + 10.33$ Ar (mix 2)	20	1540	15 - 18
$C_2H_2 + 2.5\ O_2 + 14.0$ Ar (mix 3)	50	1688	1.75

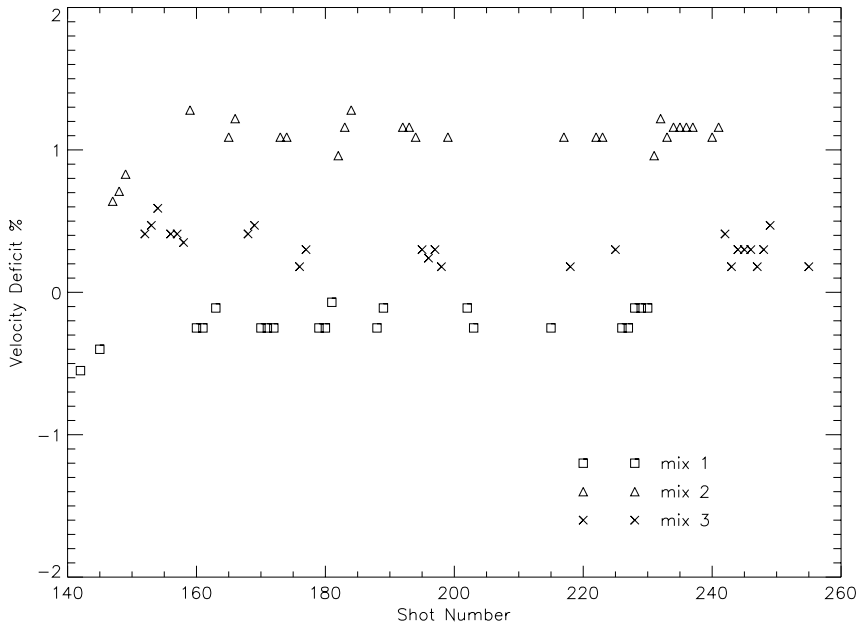

Figure 4.17: Velocity Deficits for the wedge and cylinder studies, catagorized by mixture

Table 4.2: Data From Shadowgraphs

Mix	θ (deg)	Mean χ (deg)	Stand. Dev.	Samples
1	20	5.2	0.7	21
1	25	4.9	0.6	9
1	30	4.2	0.7	9
1	35	3.1	0.7	9
1	40	2.5	0.9	9
1	45	1	0	1
2	20	13	0.6	15
2	25	11.1	0.4	9
2	30	8.9	0.5	9
2	35	6.6	0.5	9
2	40	4.8	0.7	9
2	45	2.8	0.1	3
3	20	8.7	0.1	9
3	25	6.2	0.6	9
3	30	4.5	0.24	9
3	35	3.0	0.28	9
3	40	2	0.6	9
3	45	reg.	-	1

Table 4.3: Data From Soot Foils

Mix	θ (deg)	χ (deg)
1	20	13
1	25	7 - 10
1	30	5 - 7
2	20	13 - 17
2	25	10 - 12
2	30	9
3	20	9
3	25	6 - 8
3	30	4 - 5

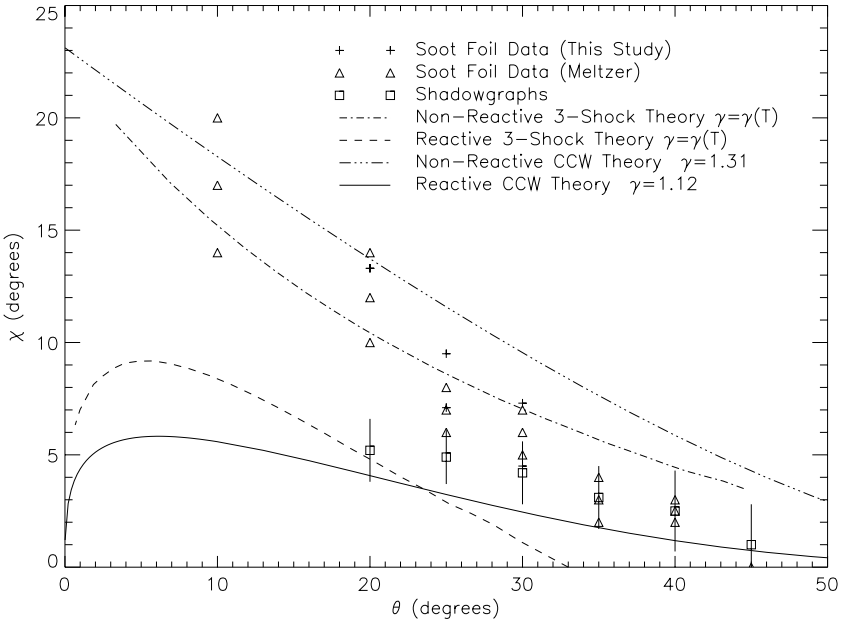

Figure 4.18: χ-θ results: mix 1.

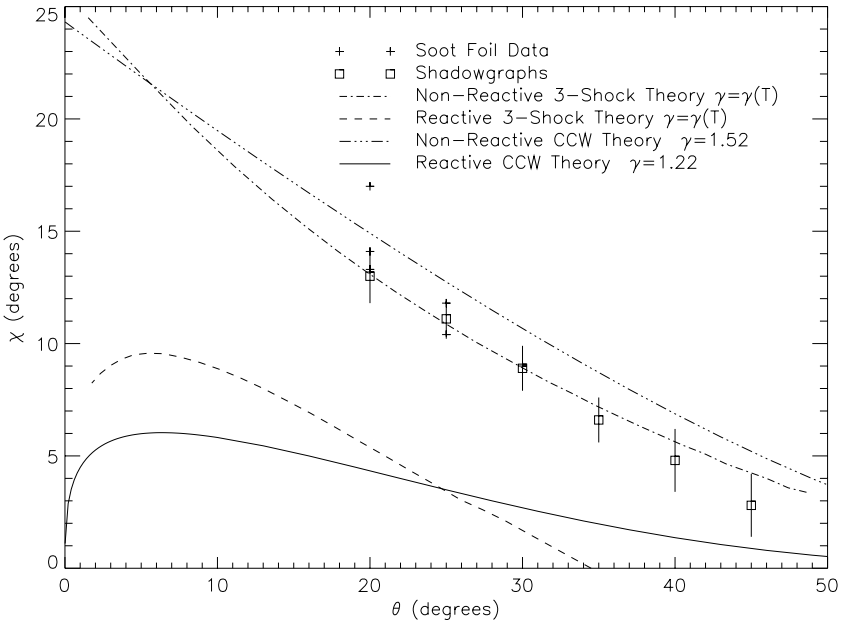

Figure 4.19: χ-θ results: mix 2.

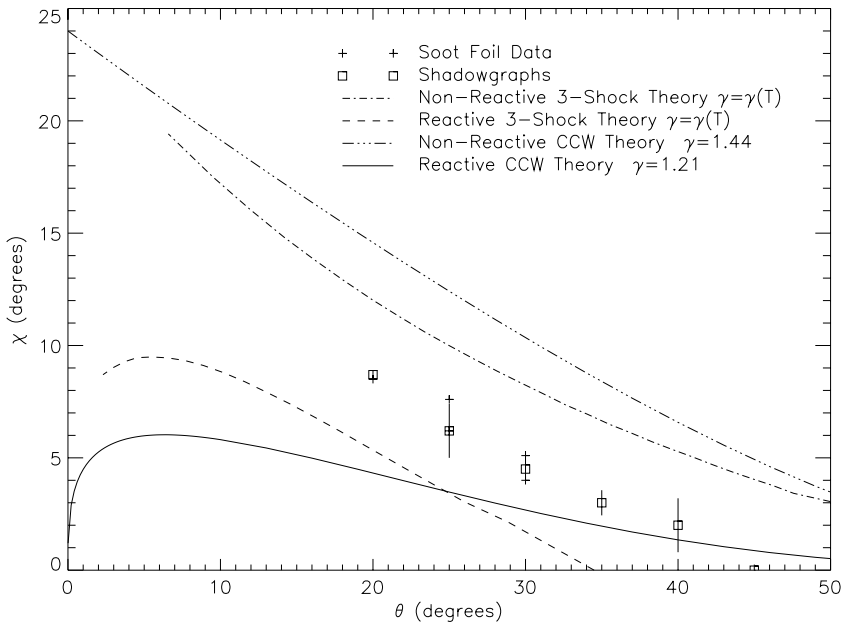

Figure 4.20: χ-θ results: mix 3.

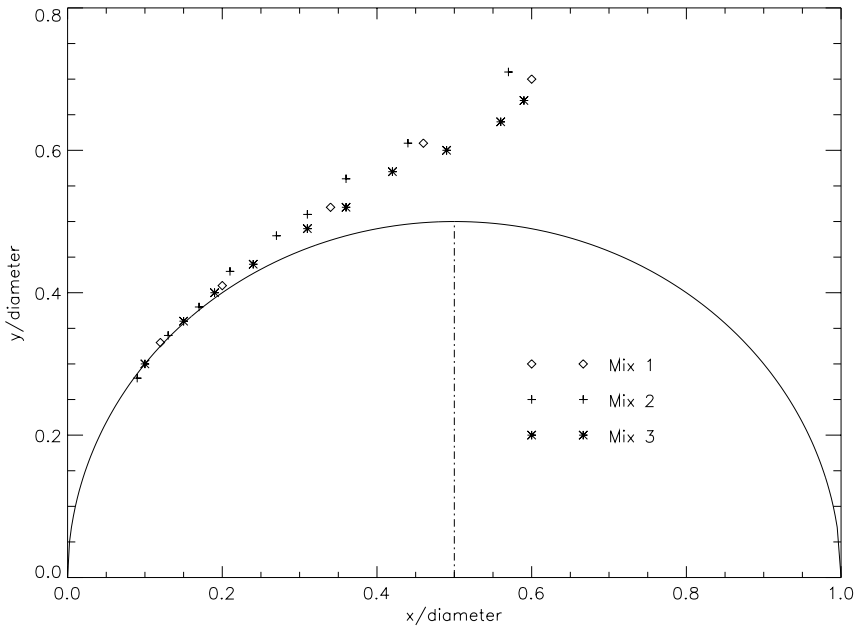

Figure 4.21: Half-Cylinder Triple Point Trajectories.

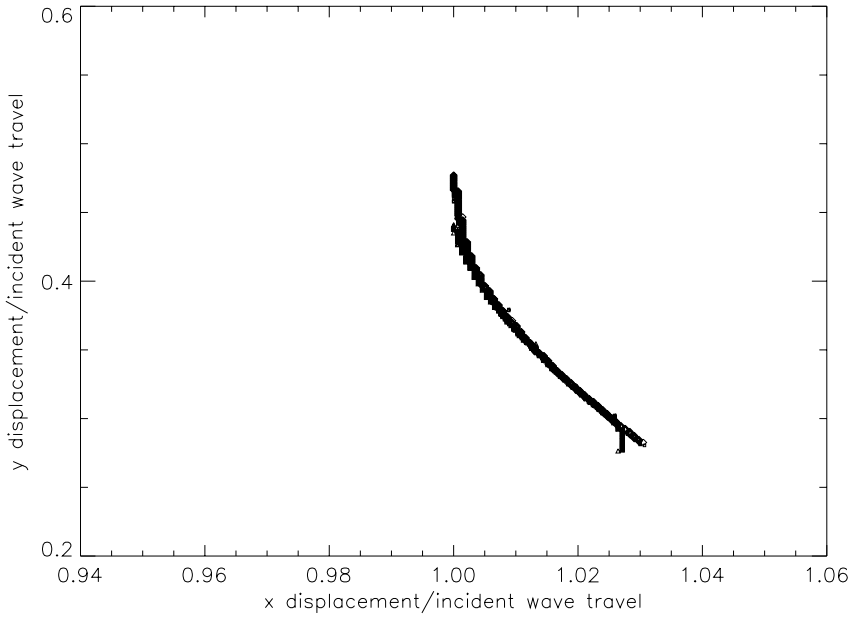

Figure 4.22: Scaled Fronts: mix 3, 15° wedge. Data from shots 145, 153 and 154

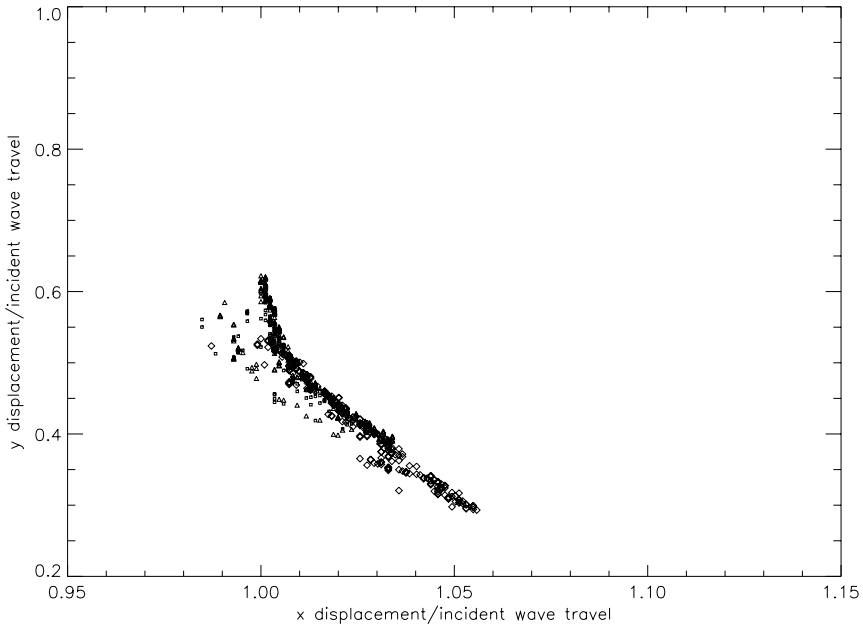

Figure 4.23: Scaled Fronts: mix 1, 20° wedge. Data from shots 149, 202 and 203

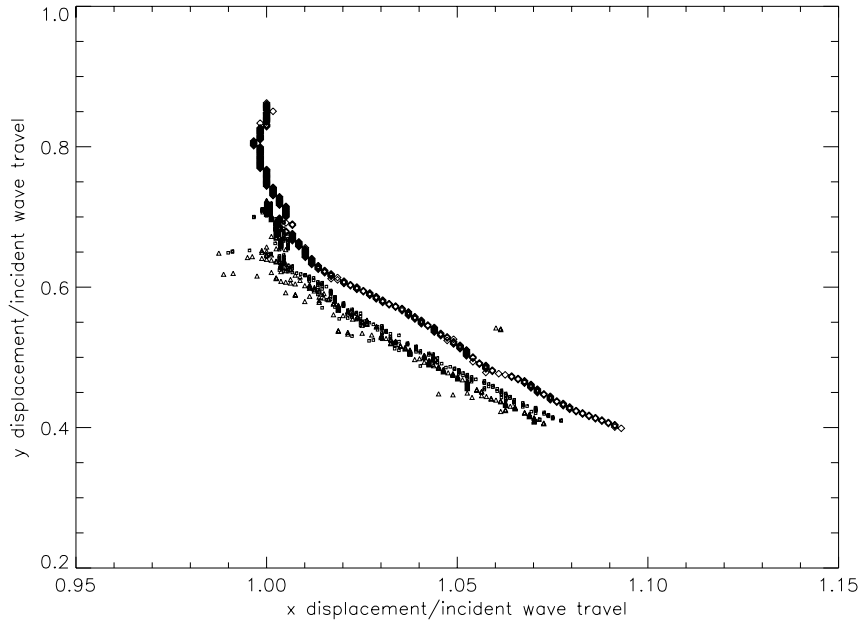

Figure 4.24: Scaled fronts: mix 2, 20° wedge. Data from shots 122, 123 and 223.

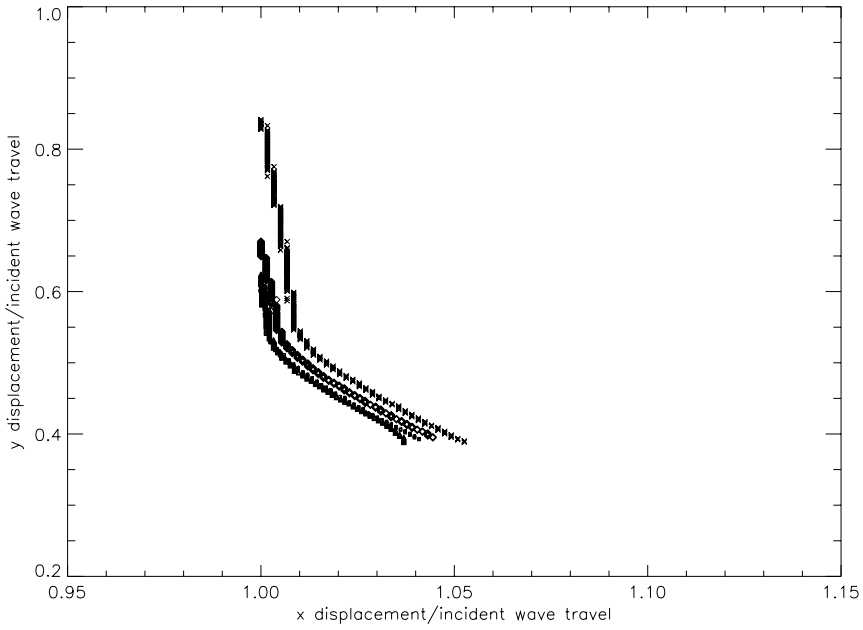

Figure 4.25: Scaled fronts: mix 3, 20° wedge. Data from shots 156, 157, 158 and 225.

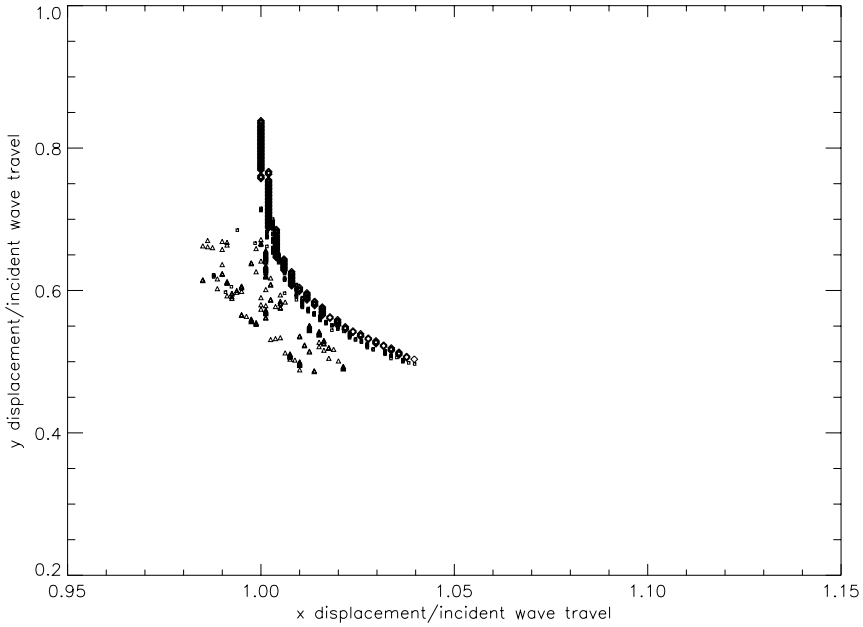

Figure 4.26: Scaled fronts: mix 1, 25° wedge. Data from shots 160, 161 and 163.

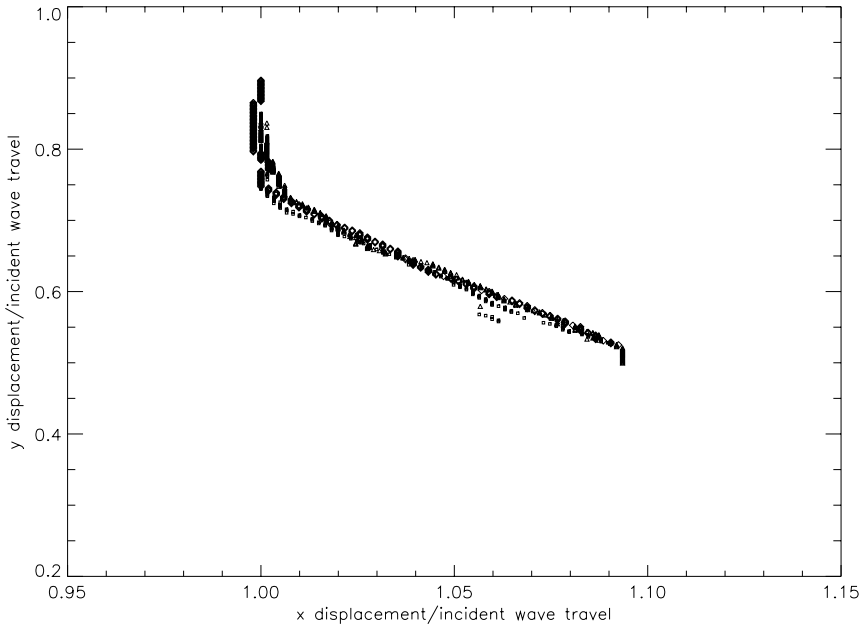

Figure 4.27: Scaled fronts: mix 2, 25° wedge. Data from shots 164, 165 and 166.

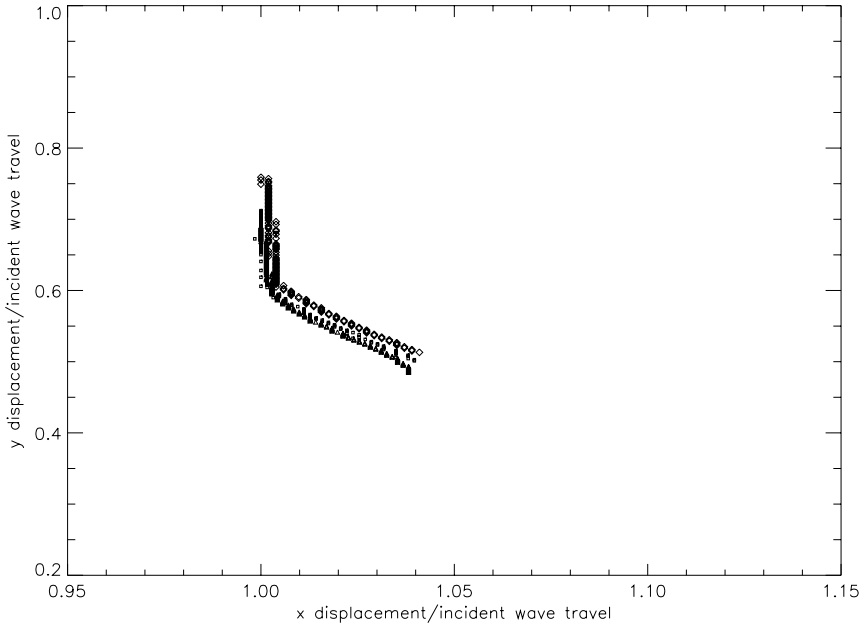

Figure 4.28: Scaled fronts: mix 3, 25° wedge. Data from shots 167, 168 and 169.

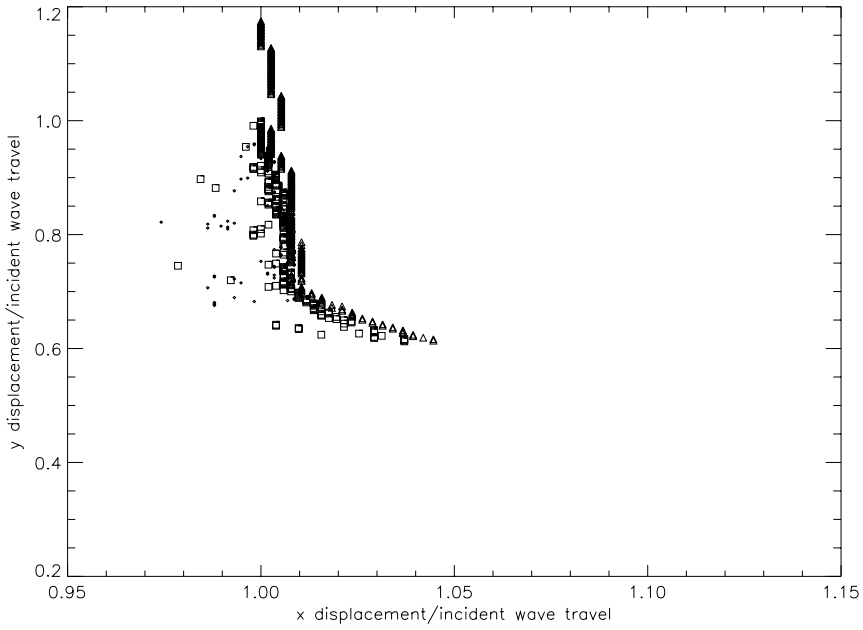

Figure 4.29: Scaled fronts: mix 1, 30° wedge. Data from shots 170, 171 and 172.

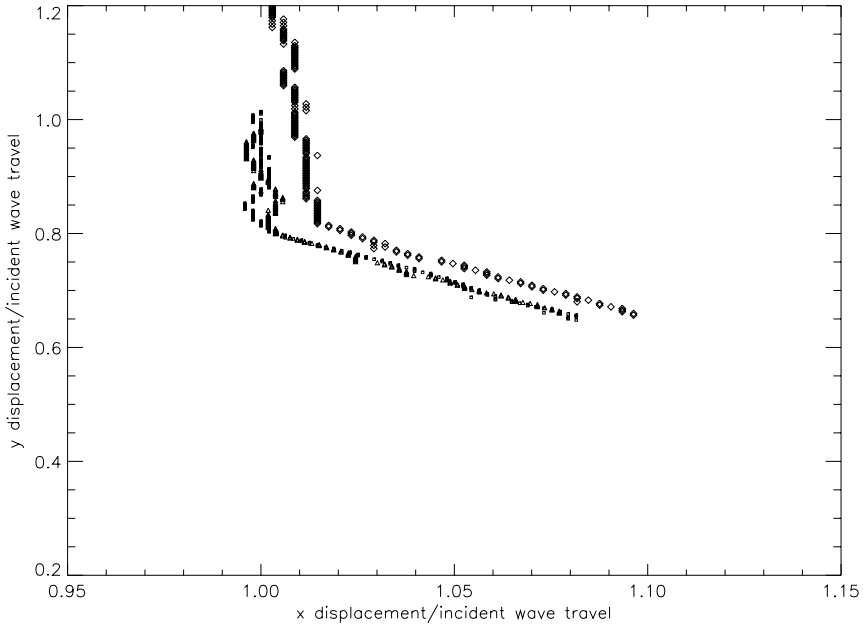

Figure 4.30: Scaled fronts: mix 2, 30° wedge. Data from shots 173, 174 and 175.

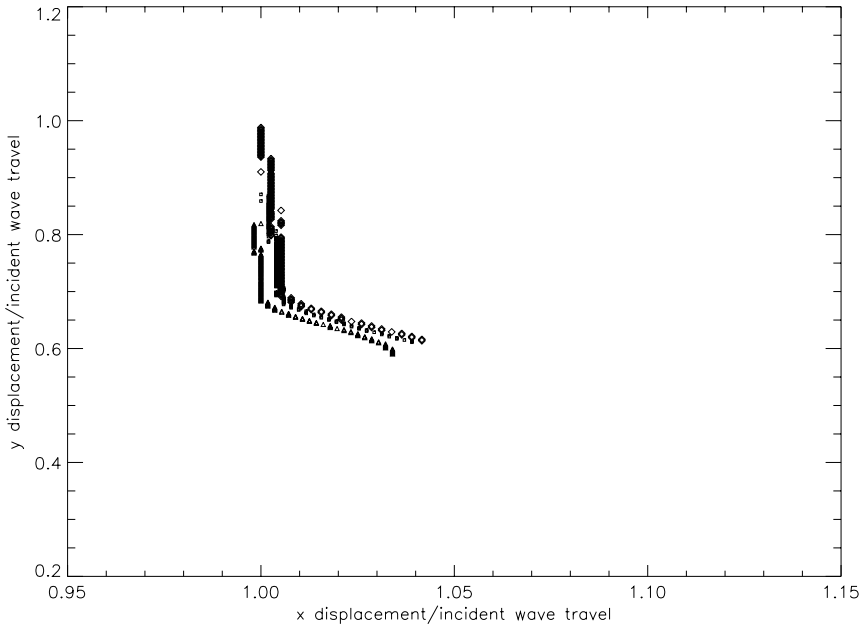

Figure 4.31: Scaled fronts: mix 3, 30° wedge. Data from shots 176, 177 and 178.

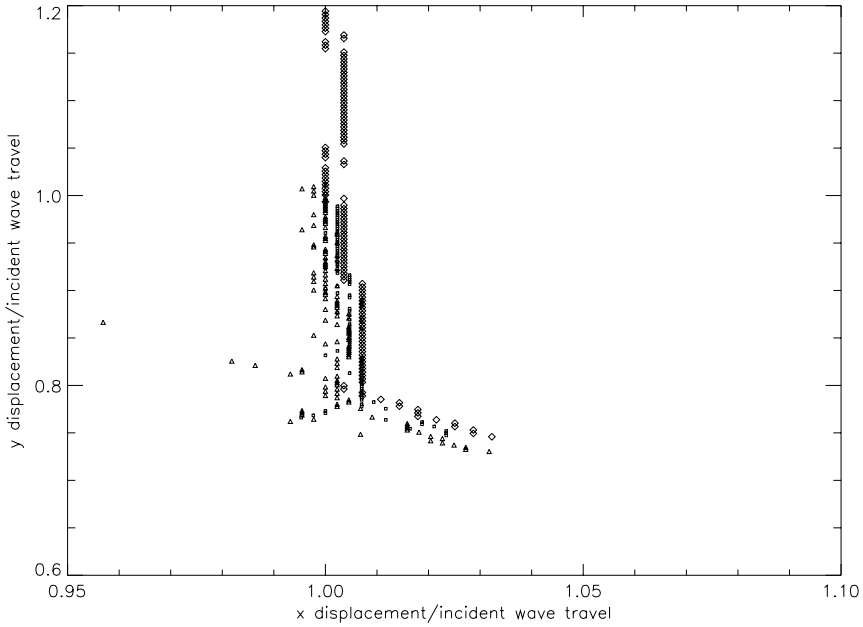

Figure 4.32: Scaled fronts: mix 1, 35° wedge. Data from shots 179, 180 and 181.

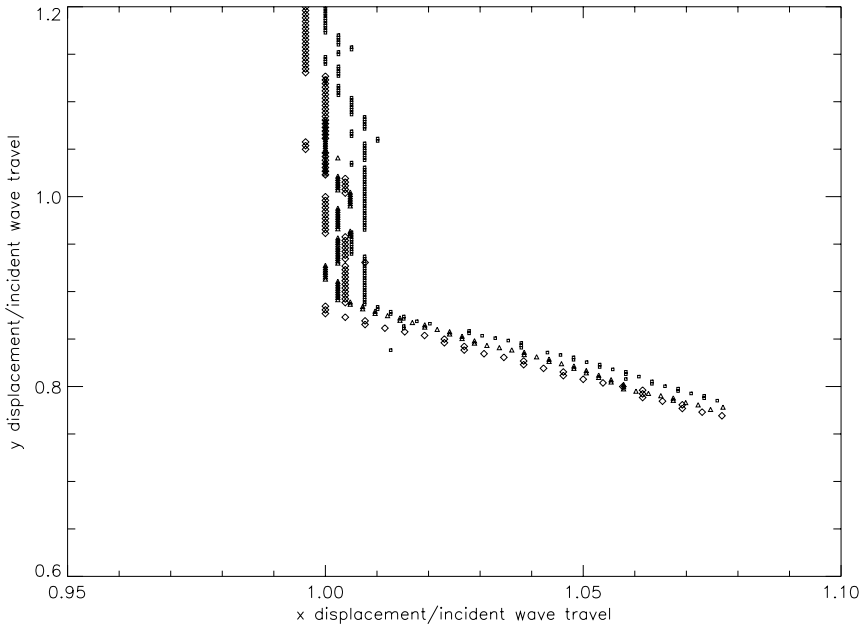

Figure 4.33: Scaled fronts: mix 2, 35° wedge. Data from shots 182, 183 and 184.

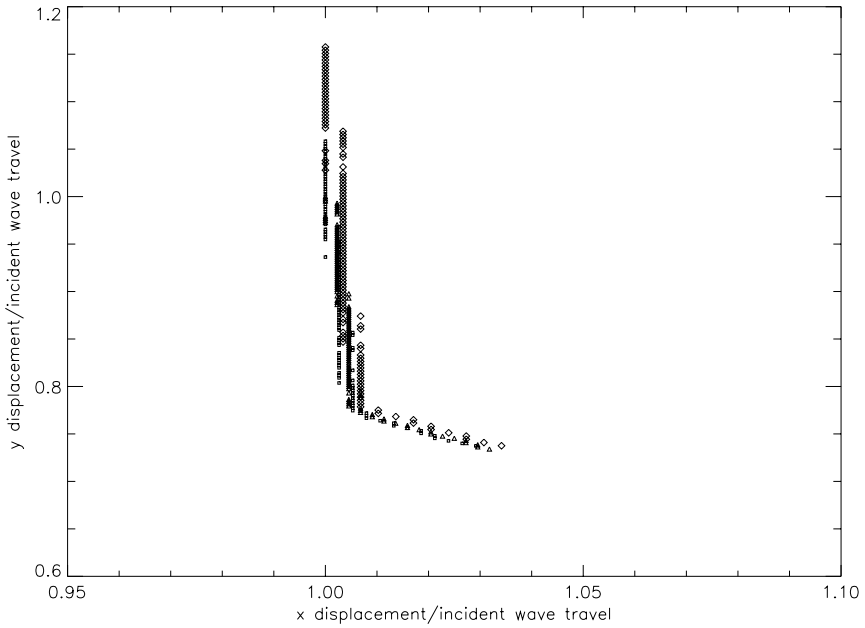

Figure 4.34: Scaled fronts: mix 3, 35° wedge. Data from shots 185, 186 and 187.

Table 4.4: Similarity Parameter of the Mixtures

L (mm)	θ (deg)	L/λ_1	L/λ_2	L/λ_3
190	15	24	11	95
140	20	17.5	7.8	70
109	25	13.6	6.1	55
88	30	11	4.9	44
73	35	9	4.1	36.5
61	40	7.6	3.4	30.5
51	45	6.4	2.8	25.5

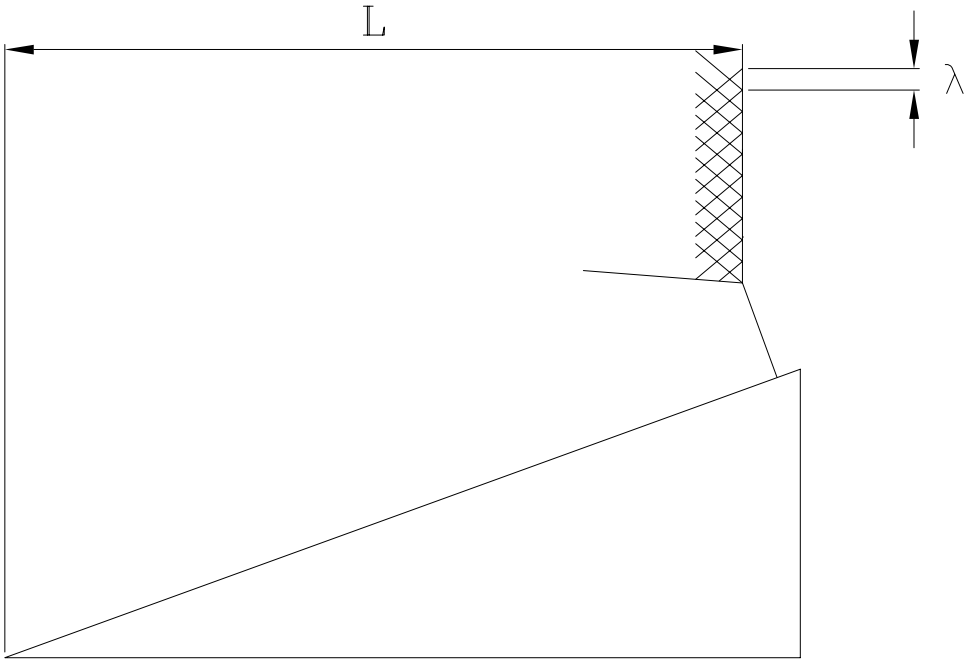

Figure 4.35: Length scales used to characterize the Mach reflection.

CHAPTER 5
Summary and Conclusions

Mach reflection in gaseous detonations was investigated, experimentally using laser shadowgraphy, and through calculations based on extensions of theories of shock wave reflection. Three reactive mixtures were studied in the experiments: mix 1 was stoichiometric hydrogen and oxygen at 295 K and 20 kPa, mix 2 was a stoichiometric hydrogen and oxygen with 77.5 % argon dilution, at 295 K and 20 kPa. Mix 3 consisted of stoichiometric acetylene and oxygen with 80 % argon dilution, at 50 kPa and 295 K. Detonations in each mixture were imaged interacting with wedges, with the value of the wedge angle, θ, ranging from 15 degrees to 50 degrees. Triple point trajectory angles, χ, were inferred from the shadowgraphs. χ was also obtained from soot foil records for wedge angles of 20, 25 and 30 degrees. To explore the self-similarity of the Mach reflections, contours of the leading waves were also obtained from the shadowgraphs. Shadowgraph studies of detonations diffracting over half-cylinders were also made. Relationships between χ and θ were calculated, using 3-shock theory and Whitham's shock dynamics theory with reactive and frozen chemistry. From the data reduction and discussion, the following conclusions are drawn:

1. The velocity deficit data from the experiments indicated the mix 1 detonations to be very slightly overdriven prior to entering the test section. However, the implications of this are uncertain, as the triple point trajectory data did not seem sensitive to these small changes.

2. Scaled comparisons of the lead wave contours for the same mix and θ show self-similar behavior of the Mach reflections within the field of view. This was found to be true for all values of θ considered, within the error in the technique. In mix 1, for a wedge angle of 30°, a slight change in shape is noticable between shots that are located at different positions on the wedge, indicating that the Mach-reflection may be evolving, and may not be self-similar.

3. For all three mixtures considered, there is clear disagreement among the calculated reactive χ-θ relations from 3-shock and reactive Whitham theories and measurements of χ from the shadowgraph images. This is to be expected for mix 2, but is contrary to expectations for mix 3 based on simple considerations of the ratio of the intrinsic length scale of the mixture and the physical length scale (the position along the wedge). This is thought to be due to the exclusion of the effect of the transverse waves in the treatments of both 3-shock theory and Whitham's theory of shock dynamics.

4. There is reasonable agreement between the calculated χ - θ relation from non-reactive 3-shock theory and the experimental values, in the case of mix 2, as expected from length scale arguments. This may be because the Mach reflection is in its early stages, in what might be termed the near field, with the dynamics of the interaction being determined by the lead shock and reflected wave pulse, within the Von Neumann state.

5. It was found that, for small θ, χ inferred from shadowgraphs was different from that inferred from the soot foil records. This effect was most pronounced for mix 1 and is attributed to the transverse waves overtaking the weak reflected pulse at the smaller wedge angles. As χ is interpreted from the apparent transverse wave spacing on the soot-foils, the angle so obtained is larger than obtained from shadowgraphs.

6. Mach stems in mix1 and mix 3 were curved at particular wedge angles. Simple reasoning suggests that this curvature may have developed from an initially straight wave, and is being observed at large enough distances away from the wedge apex, with respect to the mixture's intrinsic cell size. The curved region seemed reduced and closer to the triple-point at larger wedge angles.

7. Shadowgraphs taken of detonations interacting with a half-cylinder show that the triple point trajectories are sensitive to the incident wave speed. The images also clearly show the transformation of an initially sharp triple-point into a curve that smoothly connects the incident wave and Mach stem.

Bibliography

Akbar, R. (1991). On the Application of Whitham Theory to Gaseous Detonations. Master's thesis, Department of Aeronautical Engineering, Rensselaer Polytechnic Institute.

Bazhenova, T. V., L. G. Gvozdeva, Y. Lobastov, I. M. Naboko, R. G. Nemkov, and O. A. Predvoditeleva (1965). *Shock Waves in Real Gases*, pp. 109–113. Nauka Press, Moscow, USSR. Available as NASA TT F-585, 1969.

Bdzil, J. B., T. D. Aslam, and D. S. Stewart (1996). Curved Detonation Fronts in Solid Explosives: Collisions and Boundary Interactions. In B. Sturtevant, J. E. Shepherd, and H. G. Hornung (Eds.), *Proceedings of the 20th Int. Symp on Shock Waves*. World Scientific.

Bryson, A. E. and R. W. F. Gross (1961). Diffraction of Strong Shocks by Cones and Cylinders and Spheres. *J. Fluid Mech. 10(1)*, 1–16.

Collela, P. and L. F. Henderson (1990). The Von Neumann Paradox for the Diffraction of Weak Shock Waves. *J. Fluid Mech. 213*, 71–94.

Edwards, D. H., J. R. Walker, and M. A. Nettleton (1984). On the Propagation of Detonation Waves Along Wedges. *Archivum Combustionis 4(3)*, 197–209.

Fay, J. A. (1959). Two-Dimensional Gaseous Detonations: Velocity Deficit. *The Physics of Fluids 2*(3), 283–289.

Fickett, W. and W. C. Davis (1979). *Detonation*. University of California Press, Berkerely, CA.

Gavrilenko, T. P. and E. S. Prokhorov (1983). Overdriven Gaseous Detonations. In *Prog. Astro. Aero.*, Volume 87, pp. 244–250.

Henderson, L. F. (1980). On the Whitham theory of shock-wave diffraction at concave corners. *J. Fluid Mech. 99(4)*, 801–811.

Hornung, H. (1986). Regular and Mach Reflection of Shock Waves. *Annu. Rev. Fluid Mech. 18*, 33–58.

Law, C. K. and I. I. Glass (1971). Diffraction of Strong Shock Waves by a Sharp Compressive Corner. *C.A.S.I Transactions 4*(1), 2–12.

Lee, J. H. S. (1984). Dynamic Parameters of Gaseous Detonations. *Ann. Rev. Fluid Mech. 16*, 311–336.

Meltzer, J. (1990). The Diffraction of a Detonation by a Wedge. Master's thesis, Department of Aeronautical Engineering, Rensselaer Polytechnic Institute.

Reynolds, W. C. (1986). The Element Potential Method for Chemical Equilibrium Analysis: Implementation in the Interactive Program STANJAN; Version 3. Technical report, Stanford Univ., Palo Alto, CA.

Sandeman, R. J., A. Leitch, and H. Hornung (1980). The Influence of Relaxation on Transition to Mach Reflection in pseudosteady flow. In A. Lifshitz and J. Rom (Eds.), *Shock Tubes and Waves*, pp. 298–307.

Shepherd, J. E. (1986). Chemical Kinetics of Hydrogen-Air-Diluent Detonations. In *Dynamics of Explosions, Bowen J.R., Leyer J.-C., Soloukhin R.I.*, Volume 106, pp. 263–293.

Strehlow, R. A. (1969). On the Strength of Transverse Waves in Gaseous Detonations. *Combustion and Flame 13*, 577 – 582.

Strehlow, R. A. (1971). Detonation Structure and Gross Properties. *Combustion Science and Technology 4*, 65–71.

Thompson, P. A. (1972). *Compressible Fluid Dynamics*. McGraw-Hill, New York.

Vasiliev, A. A., T. P. Gavrilenko, and M. E. Topchian (1972). On the Chapman-Jouguet Surface in Multi-headed Gaseous Detonations. *Astronautica Acta 17*, 499–502.

Walker, J. R. (1983). *Flame Propagation and Detonation Reflection*. Ph. D. thesis, Department of Physics, University College of Wales, Aberystwyth.

Whitham, G. B. (1974). *Linear and NonLinear Waves*. Wiley-Interscience, John Wiley & Sons, New York.

APPENDIX A
Shot Lists

Table A.1: Shot List for the Dilution Study

Shot	Mixture	P kPa	T K	Driver kPa	D_{CJ} m/s	V_{1-2} m/s	V_{2-3} m/s	Deficit %
131	$2H_2 + O_2$	20	296	2.12	2750.0	2769.0	2757.0	-0.25
132	$2H_2 + O_2$ + 77.5% Ar	20	296	2.12	1557.0	1576.0	1548.0	0.58
133	$2H_2 + O_2$ + 80% Ar	20	295	2.12	1518.0	1540.0	1503.0	0.99
134	$2H_2 + O_2$ + 85% Ar	20	295	2.12	1415.0	1443.0	1399.0	1.13
135	$2H_2 + O_2$ 87% Ar	20	295	2.12	1357.0	1399.0	1342.0	1.11
136	$2H_2 + O_2$ 88% Ar	20	295	2.12	1319.0	1375.0	1307.0	0.91
137	$2H_2 + O_2$ 89% Ar	20	295	2.12	1279.0	1347.0	1271.0	0.63
138	$2H_2 + O_2$ 90% Ar	20	295	2.12	1235.0	1318.0	1236.0	-0.08

Table A.2: Shot List for the Wedge Experiments

Shot	Angle	Mixture	P kPa	T K	Driver kPa	D_{CJ} m/s	V_{1-2} m/s	V_{2-3} m/s	Deficit %
142	15°	$2H_2 + O_2$	20	295	2.12	2750.0	2760.0	2765.0	-0.55
145	15°	$2H_2 + O_2$	20	296	2	2750.0	2764.0	2761.0	-0.40
147	15°	$2H_2 + O_2 + 10.33$ Ar	20	296	2	1557.0	1574.0	1547.0	0.64
148	15°	$2H_2 + O_2 + 10.33$ Ar	20	296	2	1557.0	1572.0	1546.0	0.71
149	15°	$2H_2 + O_2 + 10.33$ Ar	20	296	2	1557.0	1565.0	1544.0	0.83
152	15°	$C_2H_2 + 2.5O_2 + 14$ Ar	50	296	1.5	1693.0	1693.0	1686.0	0.41
153	15°	$C_2H_2 + 2.5O_2 + 14$ Ar	50	296	1.5	1693.0	1690.0	1685.0	0.47
154	15°	$C_2H_2 + 2.5O_2 + 14$ Ar	50	296	1.5	1693.0	1691.0	1683.0	0.59
156	20°	$C_2H_2 + 2.5O_2 + 14$ Ar	50	296	1.5	1693.0	1690.0	1686.0	0.41
157	20°	$C_2H_2 + 2.5O_2 + 14$ Ar	50	295	1.5	1693.0	1693.0	1686.0	0.41
158	20°	$C_2H_2 + 2.5O_2 + 14$ Ar	50	295	1.5	1693.0	1693.0	1687.0	0.35
159	20°	$2H_2 + O_2 + 10.33$ Ar	20	296	1.5	1557.0	1554.0	1537.0	1.28
160	25°	$2H_2 + O_2$	20	295	1.5	2750.0	2769.0	2757.0	-0.25
161	25°	$2H_2 + O_2$	20	295	1.5	2750.0	2769.0	2757.0	-0.25
163	25°	$2H_2 + O_2$	20	296	1.5	2750.0	2764.0	2753.0	-0.11
164	25°	$2H_2 + O_2 + 10.33$ Ar	20	295	1.5	1557.0	DAS	Error	-
165	25°	$2H_2 + O_2 + 10.33$ Ar	20	295	1.5	1557.0	1556.0	1540.0	1.09
166	25°	$2H_2 + O_2 + 10.33$ Ar	20	295	1.5	1557.0	1554.0	1538.0	1.22
167	25°	$C_2H_2 + 2.5O_2 + 14$ Ar	50	295	1.5	1693.0	DAS	Error	-
168	25°	$C_2H_2 + 2.5O_2 + 14$ Ar	50	295	1.5	1693.0	1690.0	1686.0	0.41
169	25°	$C_2H_2 + 2.5O_2 + 14$ Ar	50	296	1.5	1693.0	1691.0	1685.0	0.47
170	30°	$2H_2 + O_2$	20	295	1.5	2750.0	2764.0	2757.0	-0.25
171	30°	$2H_2 + O_2$	20	295	1.5	2750.0	2764.0	2757.0	-0.25
172	30°	$2H_2 + O_2$	20	295	1.5	2750.0	2769.0	2757.0	-0.25
173	30°	$2H_2 + O_2 + 10.33$ Ar	20	295	1.5	1557.0	1556.0	1540.0	1.09
174	30°	$2H_2 + O_2 + 10.33$ Ar	20	295	1.5	1557.0	1559.0	1540.0	1.09
175	30°	$2H_2 + O_2 + 10.33$ Ar	20	295	1.5	1557.0	DAS	Error	-
176	30°	$C_2H_2 + 2.5O_2 + 14$ Ar	50	296	1.5	1693.0	1690.0	1690.0	0.18
177	30°	$C_2H_2 + 2.5O_2 + 14$ Ar	50	296	1.5	1693.0	1688.0	1688.0	0.30
178	30°	$C_2H_2 + 2.5O_2 + 14$ Ar	50	296	1.5	1693.0	DAS	Error	-
179	35°	$2H_2 + O_2$	20	295	1.5	2750.0	2769.0	2757.0	-0.25
180	35°	$2H_2 + O_2$	20	295	1.5	2750.0	2764.0	2757.0	-0.25
181	35°	$2H_2 + O_2$	20	295	1.5	2750.0	2760.0	2752.0	-0.07
182	35°	$2H_2 + O_2 + 10.33$ Ar	20	295	1.5	1557.0	1556.0	1542.0	0.96
183	35°	$2H_2 + O_2 + 10.33$ Ar	20	295	1.5	1557.0	1556.0	1539.0	1.16
184	35°	$2H_2 + O_2 + 10.33$ Ar	20	295	1.5	1557.0	1556.0	1537.0	1.28
185	35°	$C_2H_2 + 2.5O_2 + 14$ Ar	50	296	1.5	1693.0	DAS	Error	-
186	35°	$C_2H_2 + 2.5O_2 + 14$ Ar	50	296	1.5	1693.0	DAS	Error	-
187	35°	$C_2H_2 + 2.5O_2 + 14$ Ar	50	296	1.5	1693.0	DAS	Error	-
188	40°	$2H_2 + O_2$	20	295	1.5	2750.0	2769.0	2757.0	-0.25
189	40°	$2H_2 + O_2$	20	295	1.5	2750.0	2769.0	2753.0	-0.11
190	40°	$2H_2 + O_2$	20	295	1.5	2750.0	DAS	Error	-
192	40°	$2H_2 + O_2 + 10.33$ Ar	20	295	1.5	1557.0	1557.0	1539.0	1.16
193	40°	$2H_2 + O_2 + 10.33$ Ar	20	295	1.5	1557.0	1555.0	1539.0	1.16
194	40°	$2H_2 + O_2 + 10.33$ Ar	20	295	1.5	1557.0	1553.0	1540.0	1.09
195	40°	$C_2H_2 + 2.5O_2 + 14$ Ar	50	295	1.5	1693.0	1691.0	1688.0	0.30
196	40°	$C_2H_2 + 2.5O_2 + 14$ Ar	50	295	1.5	1693.0	1690.0	1689.0	0.24
197	40°	$C_2H_2 + 2.5O_2 + 14$ Ar	50	295	1.5	1693.0	1690.0	1688.0	0.30
198	45°	$C_2H_2 + 2.5O_2 + 14$ Ar	50	296	1.5	1693.0	1691.0	1690.0	0.18
199	45°	$2H_2 + O_2 + 10.33$ Ar	20	295	1.5	1557.0	1559.0	1540.0	1.09
200	45°	$2H_2 + O_2$	20	296	1.5	2750.0	DAS	Error	-
202	20°	Re-check $2H_2 + O_2$	20	295	1	2750.0	2769.0	2753.0	-0.11
203	20°	Re-check $2H_2 + O_2$	20	295	<1	2750.0	2764.0	2757.0	-0.25
215	50°	$2H_2 + O_2$	20	296	1.5	2750.0	2769.0	2757.0	-0.25
217	50°	$2H_2 + O_2 + 10.33$ Ar	20	296	1.5	1557.0	1556.0	1540.0	1.09
218	50°	$C_2H_2 + 2.5O_2 + 14$ Ar	50	296	1.5	1693.0	1691.0	1690.0	0.18
222	20°	$2H_2 + O_2 + 10.33$ Ar	20	296	1.5	1557.0	1556.0	1540.0	1.09
223	20°	$2H_2 + O_2 + 10.33$ Ar	20	296	1.5	1557.0	1555.0	1540.0	1.09
224	20°	Air Blast	100.6	296	1.5	-	648.0	598.0	
225	20°	$C_2H_2 + 2.5O_2 + 14$ Ar	50	296	1.5	1693.0	1690.0	1688.0	0.30

Table A.3: Shot List for the 4 inch Half-Cylinder

Shot	Mixture	P kPa	T K	Driver kPa	D_{CJ} m/s	V_{1-2} m/s	V_{2-3} m/s	Deficit %
226	$2H_2 + O_2$	20	296	1.5	2750.0	2765.0	2757.0	-0.25
227	$2H_2 + O_2$	20	296	1.5	2750.0	2764.0	2757.0	-0.25
228	$2H_2 + O_2$	20	296	1.5	2750.0	2769.0	2753.0	-0.11
229	$2H_2 + O_2$	20	296	1.5	2750.0	2764.0	2753.0	-0.11
230	$2H_2 + O_2$	20	296	1.5	2750.0	2764.0	2753.0	-0.11
231	$2H_2 + O_2 + 10.33$ Ar	20	296	1.5	1557.0	1559.0	1542.0	0.96
232	$2H_2 + O_2 + 10.33$ Ar	20	296	1.5	1557.0	1556.0	1538.0	1.22
233	$2H_2 + O_2 + 10.33$ Ar	20	296	1.5	1557.0	1559.0	1540.0	1.09
234	$2H_2 + O_2 + 10.33$ Ar	20	296	1.5	1557.0	1557.0	1539.0	1.16
235	$2H_2 + O_2 + 10.33$ Ar	20	296	1.5	1557.0	1557.0	1539.0	1.16
236	$2H_2 + O_2 + 10.33$ Ar	20	296	1.5	1557.0	1557.0	1539.0	1.16
237	$2H_2 + O_2 + 10.33$ Ar	20	296	1.5	1557.0	1555.0	1539.0	1.16
240	$2H_2 + O_2 + 10.33$ Ar	20	296	1.5	1557.0	1556.0	1540.0	1.09
241	$2H_2 + O_2 + 10.33$ Ar	20	296	1.5	1557.0	1553.0	1539.0	1.16
242	$C_2H_2 + 2.5O_2 + 14$ Ar	50	296	1.5	1693.0	1693.0	1686.0	0.41
243	$C_2H_2 + 2.5O_2 + 14$ Ar	50	296	1.5	1693.0	1691.0	1690.0	0.18
244	$C_2H_2 + 2.5O_2 + 14$ Ar	50	296	1.5	1693.0	1690.0	1688.0	0.30
245	$C_2H_2 + 2.5O_2 + 14$ Ar	50	296	1.5	1693.0	1690.0	1688.0	0.30
246	$C_2H_2 + 2.5O_2 + 14$ Ar	50	296	1.5	1693.0	1690.0	1688.0	0.30
247	$C_2H_2 + 2.5O_2 + 14$ Ar	50	296	1.5	1693.0	1690.0	1690.0	0.18
248	$C_2H_2 + 2.5O_2 + 14$ Ar	50	296	1.5	1693.0	1688.0	1688.0	0.30
249	$C_2H_2 + 2.5O_2 + 14$ Ar	50	296	1.5	1693.0	1688.0	1685.0	0.47
250	$C_2H_2 + 2.5O_2 + 14$ Ar	50	296	1.5	1693.0	-	-	
255	$C_2H_2 + 2.5O_2 + 14$ Ar	50	296	1.5	1693.0	1691.0	1690.0	0.18

APPENDIX B
Shadowgraphs

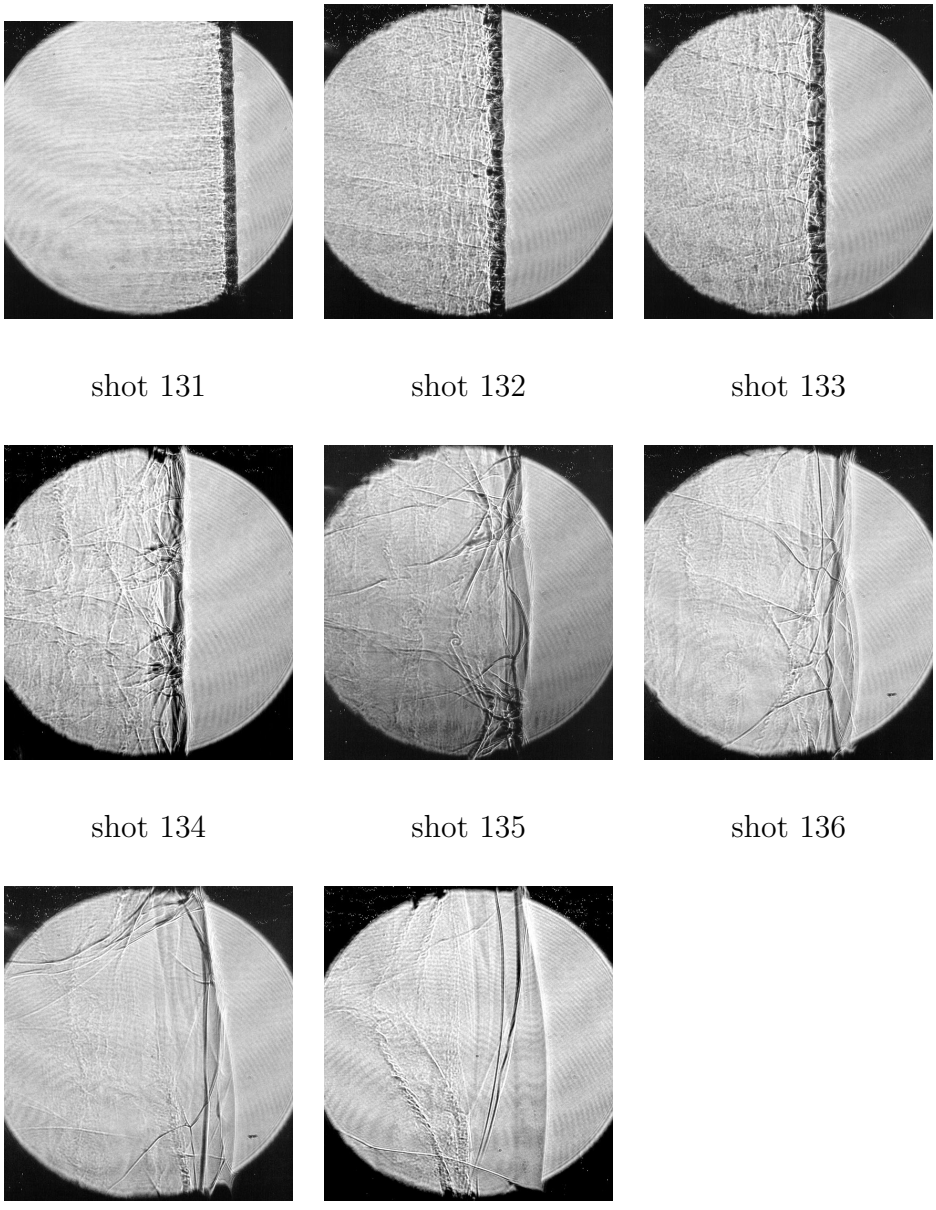

Figure B.1: Effect of argon dilution on observed cellular structure (inital pressure and temperature: 20 kPa and 295 K)

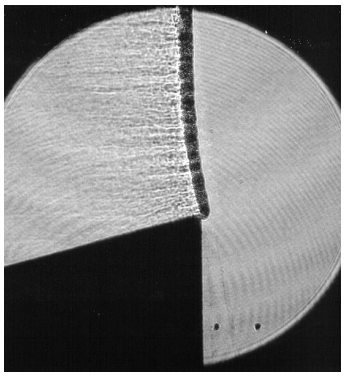

shot 142

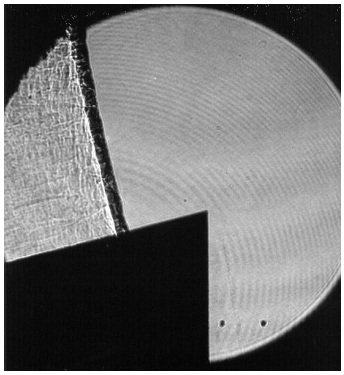

shot 149

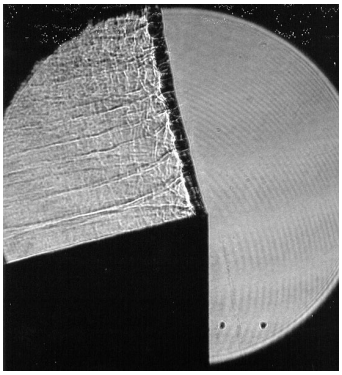

shot 148

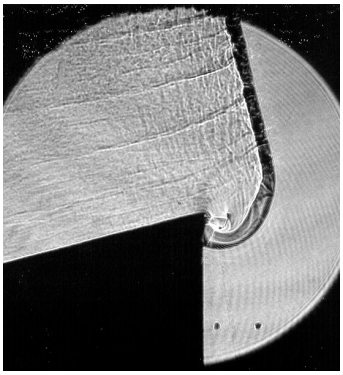

shot 147

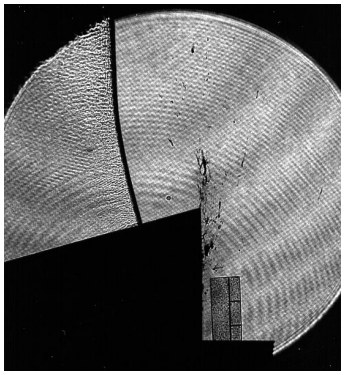

shot 154

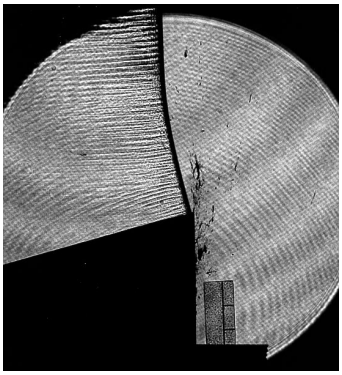

shot 153

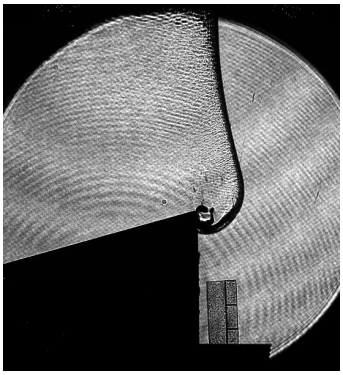

shot 152

Figure B.2: 15^o **Wedge**

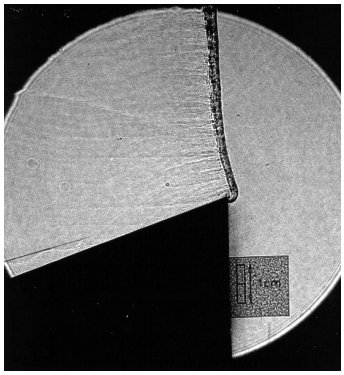

shot 202

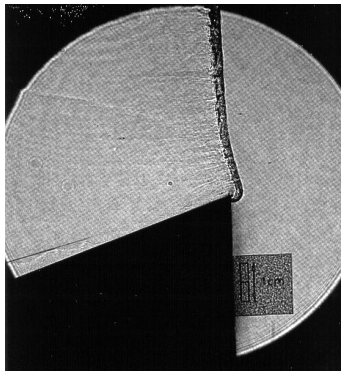

shot 203

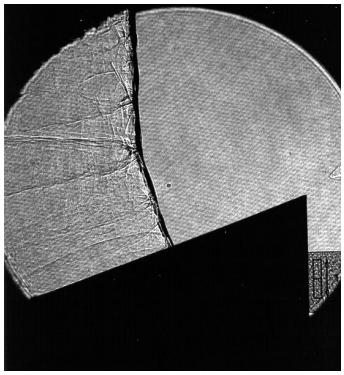

shot 223

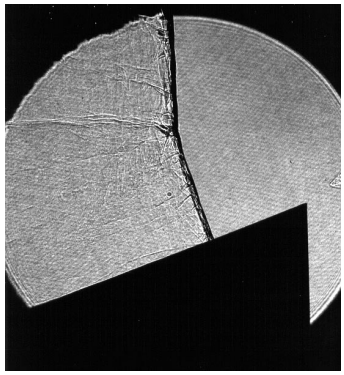

shot 222

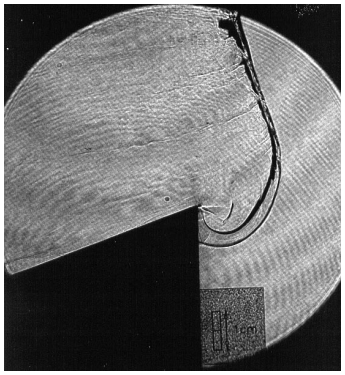

shot 159

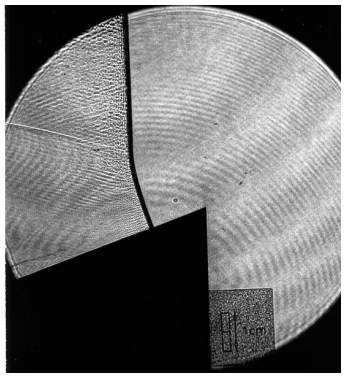

shot 158

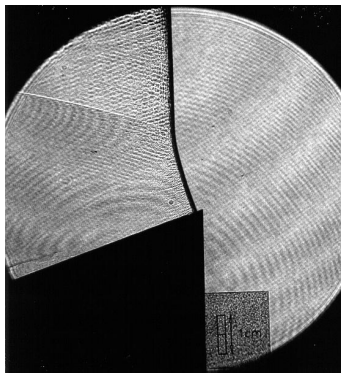

shot 156

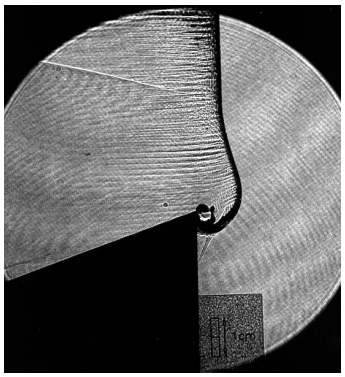

shot 157

Figure B.3: 20^o **Wedge**

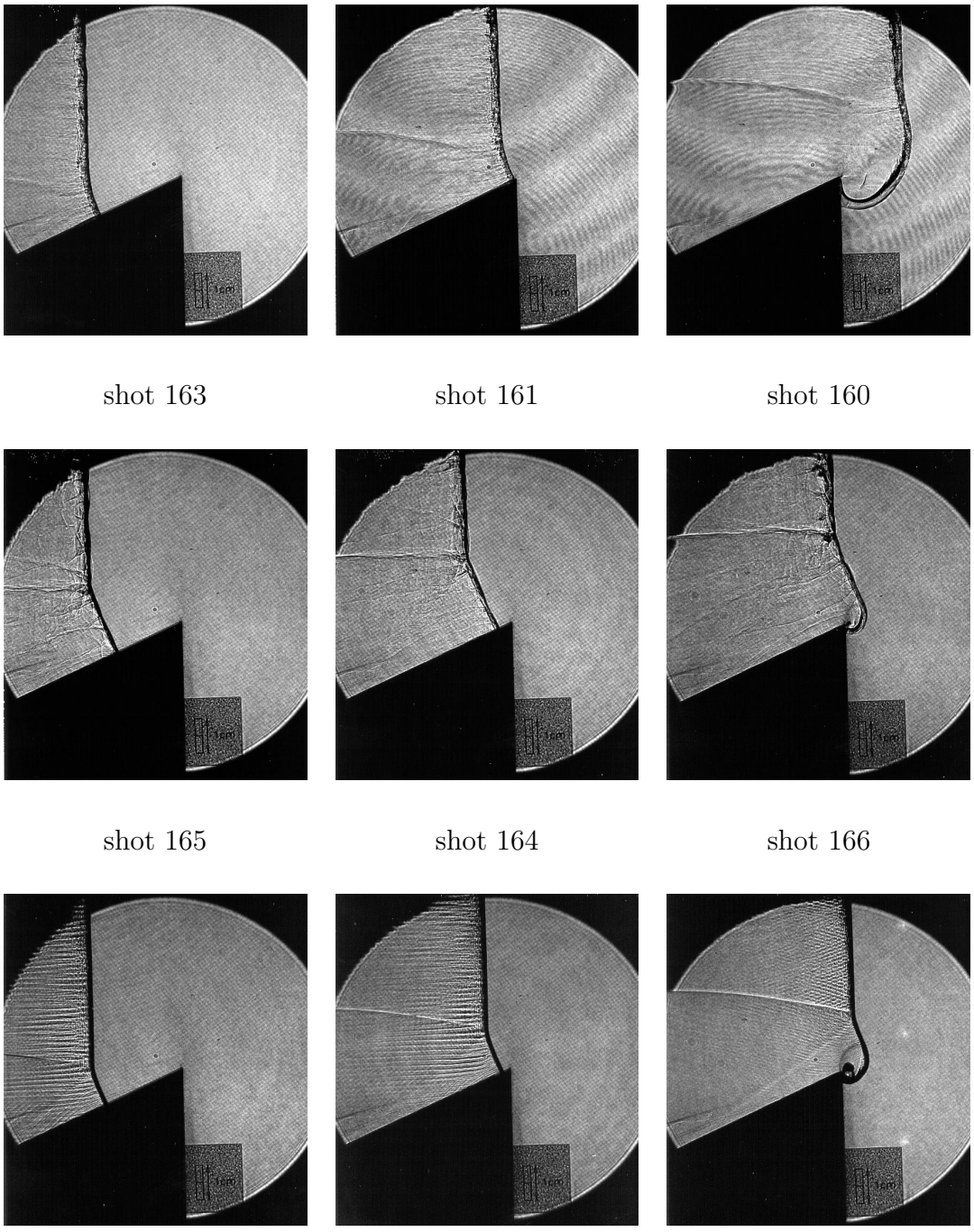

shot 163 shot 161 shot 160

shot 165 shot 164 shot 166

shot 167 shot 168 shot 169

Figure B.4: 25^o **Wedge**

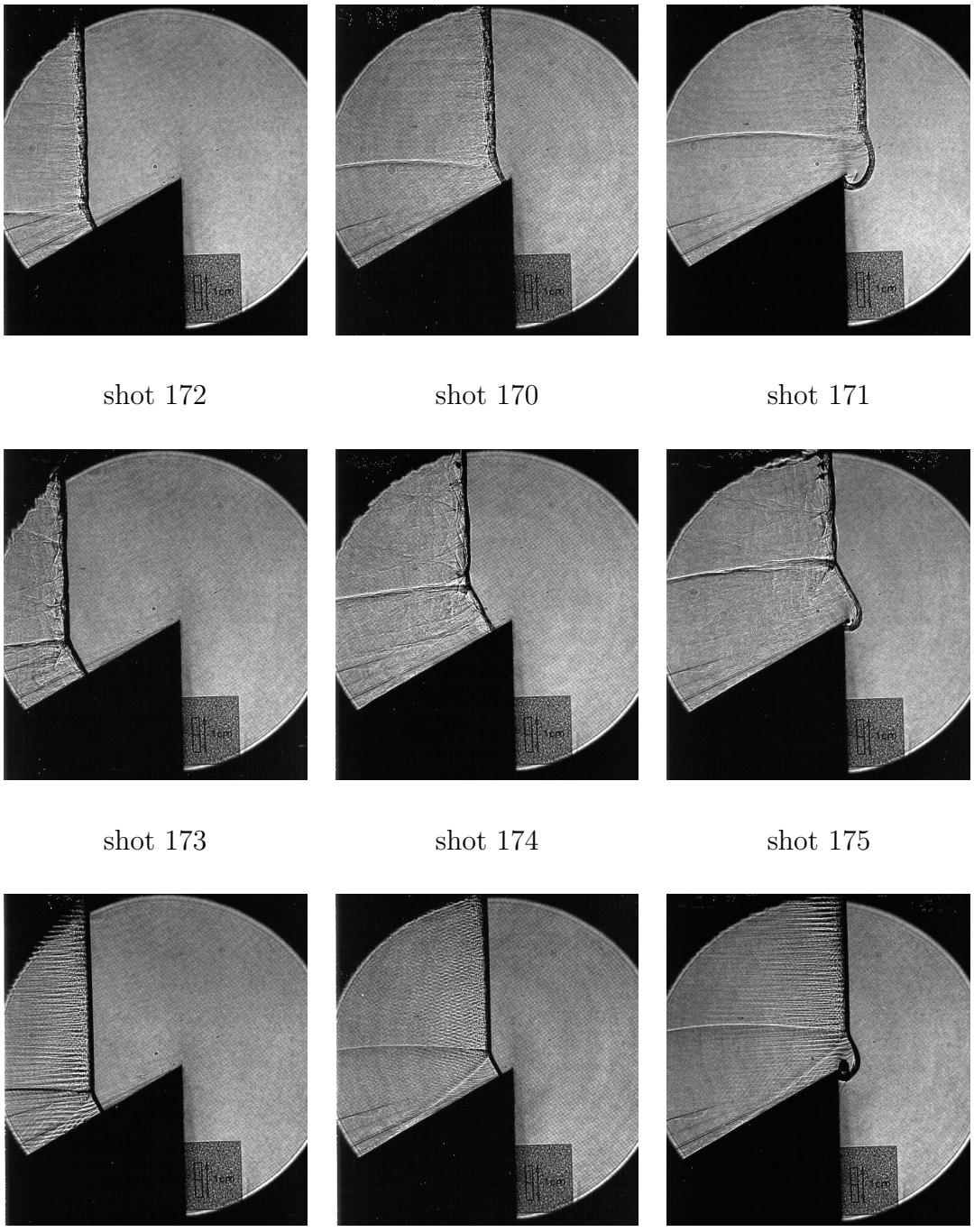

shot 172 shot 170 shot 171

shot 173 shot 174 shot 175

shot 176 shot 177 shot 178

Figure B.5: 30^o **Wedge**

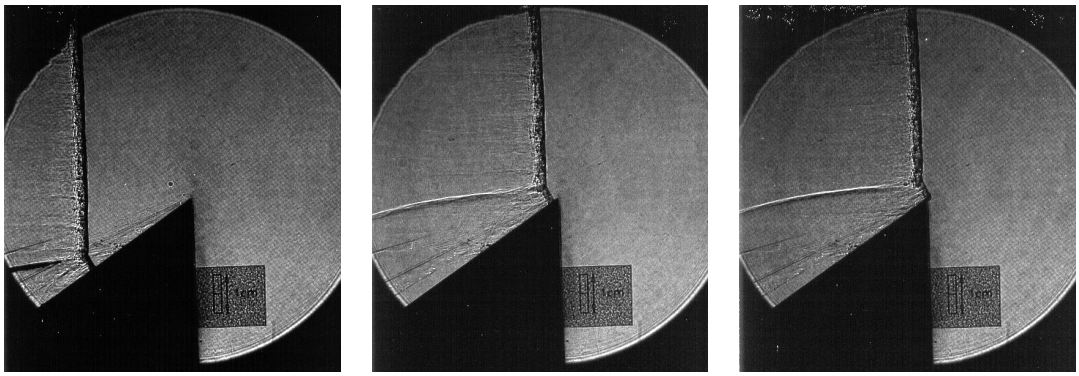

shot 179 shot 180 shot 181

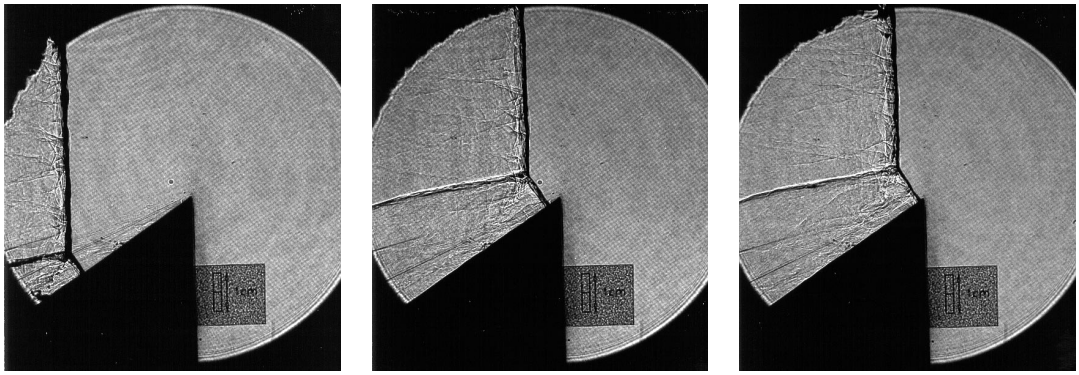

shot 182 shot 183 shot 184

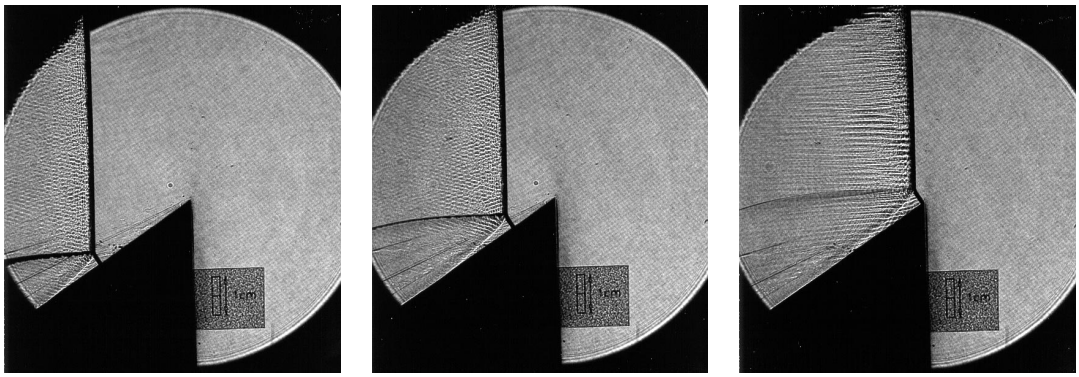

shot 185 shot 187 shot 186

Figure B.6: 35^o **Wedge**

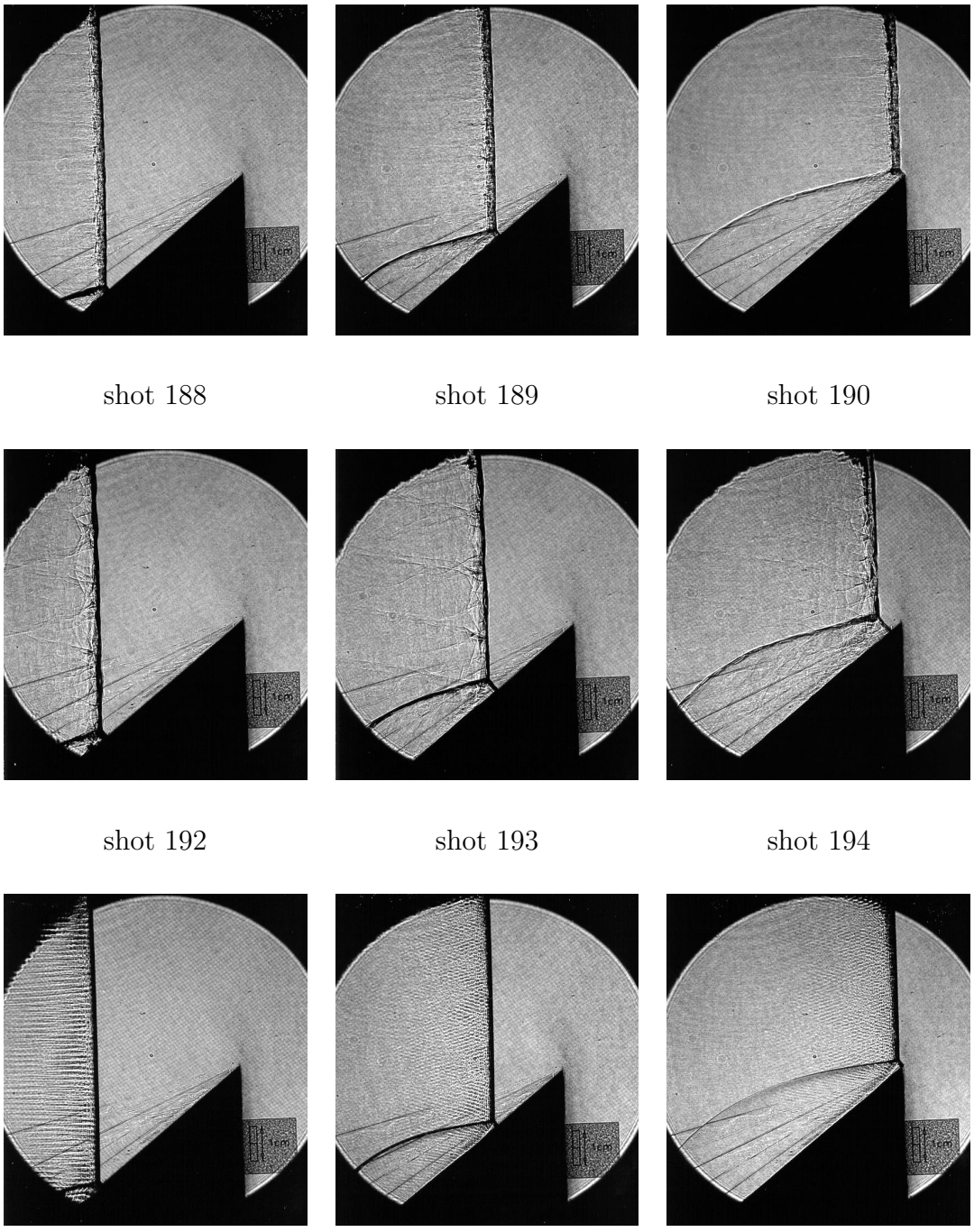

shot 188 shot 189 shot 190

shot 192 shot 193 shot 194

shot 195 shot 196 shot 197

Figure B.7: 40^o **Wedge**

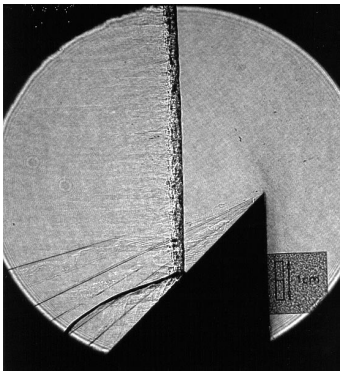

shot 200

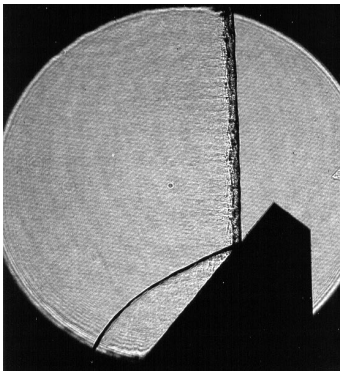

shot 215

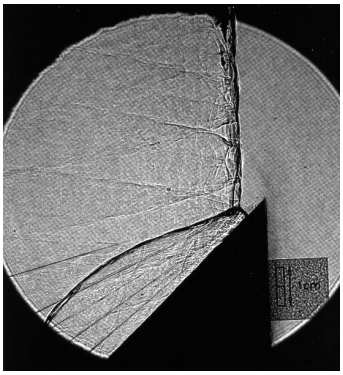

shot 199

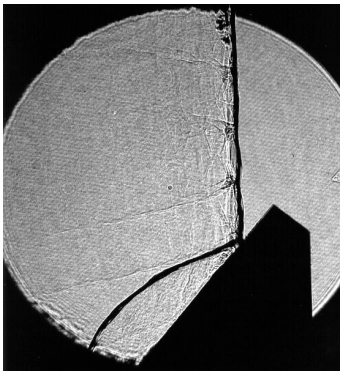

shot 217

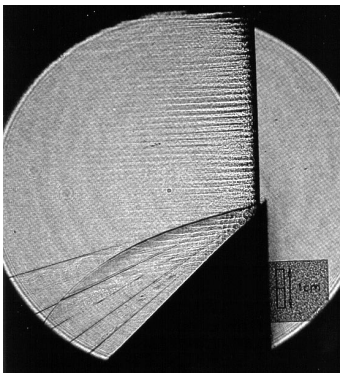

shot 198

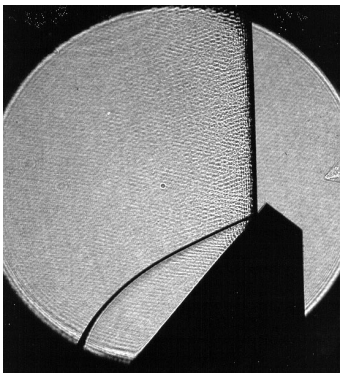

shot 218

Figure B.8: 45^o **and** 50^o **Wedges**

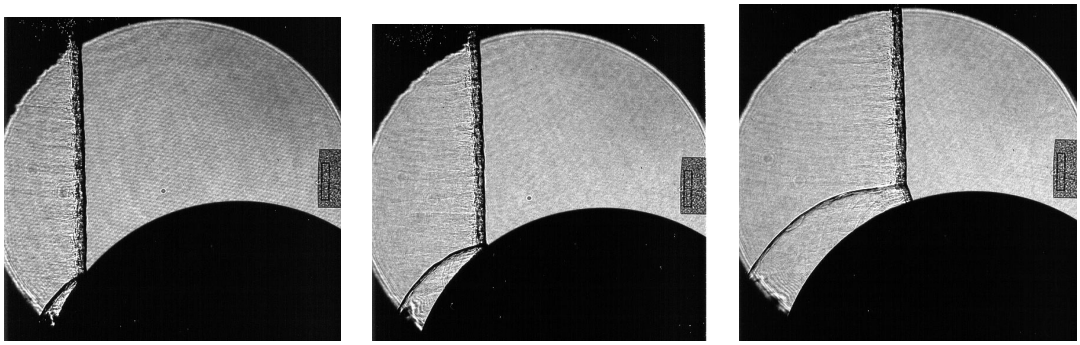

shot 228 shot 227 shot 229

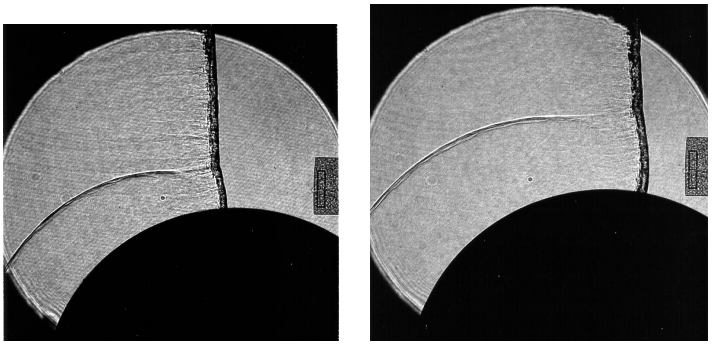

shot 226 shot 230

Figure B.9: Half-Cylinder Study: Mix 1

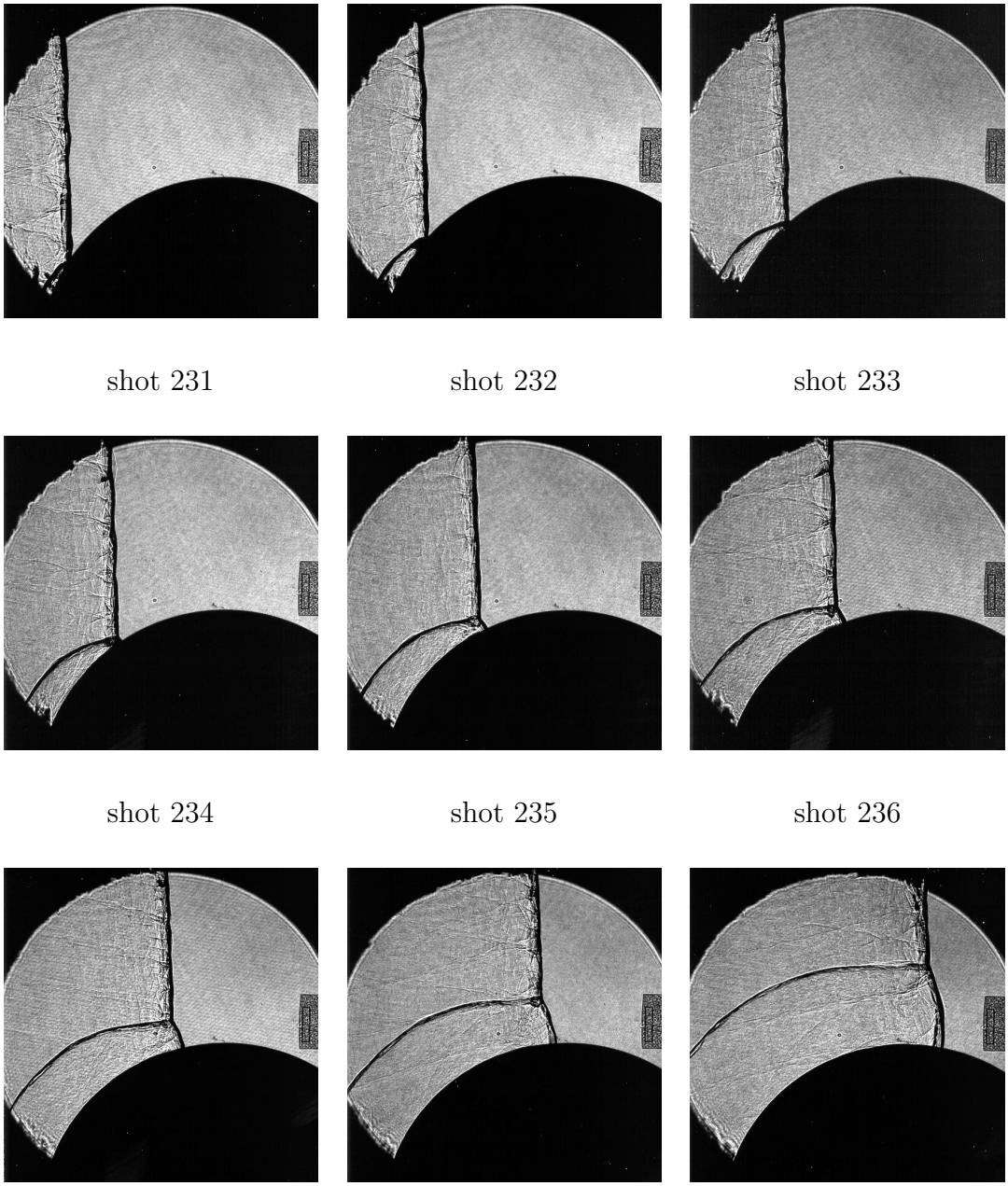

shot 231 shot 232 shot 233

shot 234 shot 235 shot 236

shot 237 shot 240 shot 241

Figure B.10: Half-Cylinder Study: Mix 2

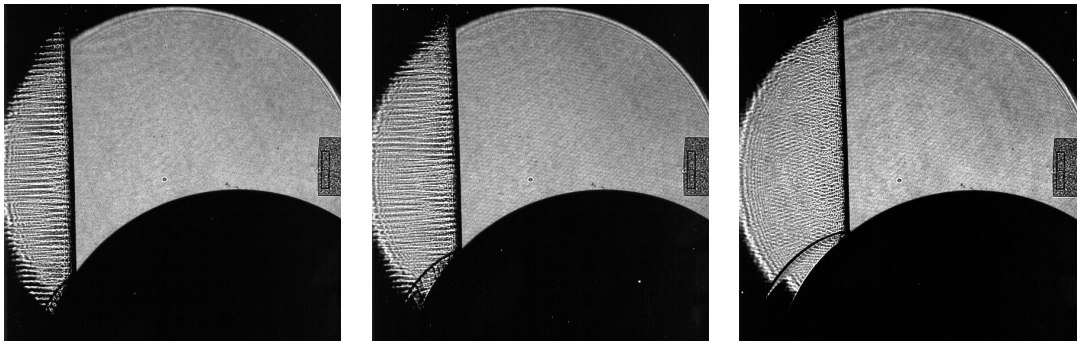

shot 242 shot 243 shot 244

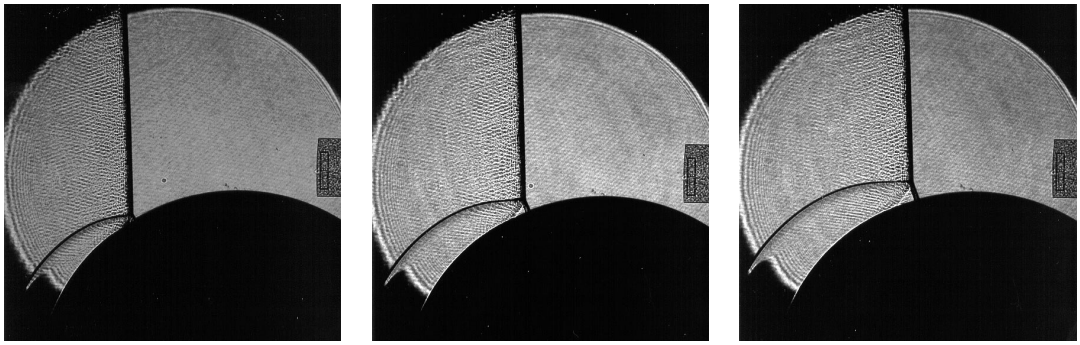

shot 245 shot 246 shot 247

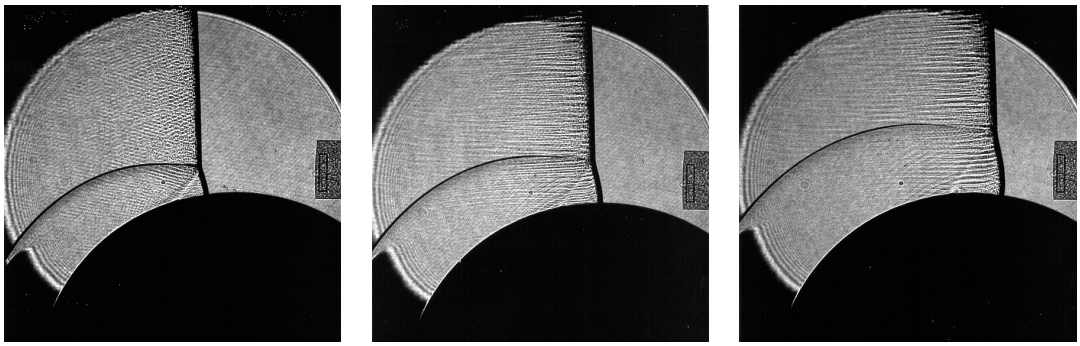

shot 248 shot 249 shot 250

Figure B.11: Half-Cylinder Study: Mix 3

APPENDIX C
Shot Pressure Traces

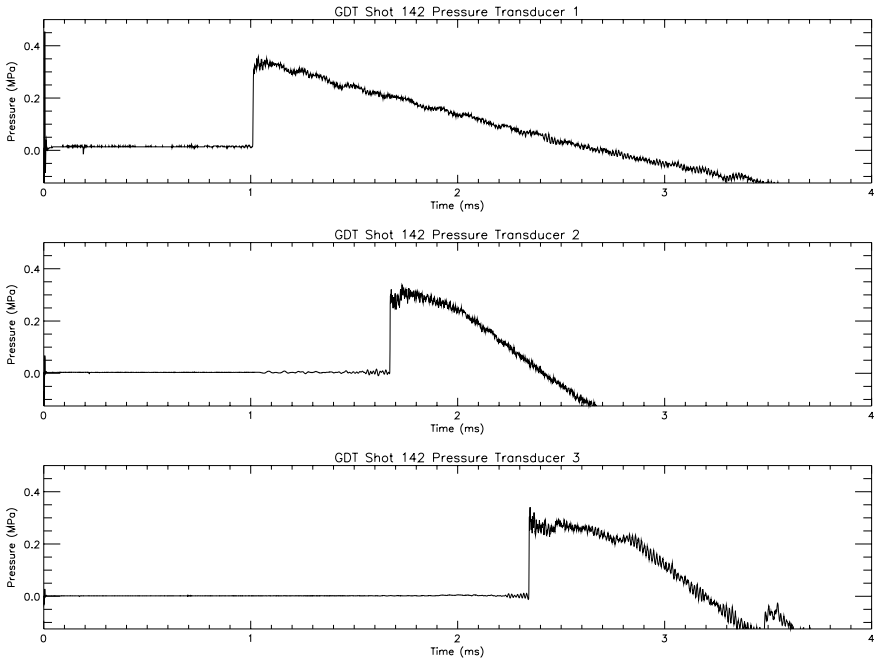

Figure C.1: Pressure Traces for Shot 142

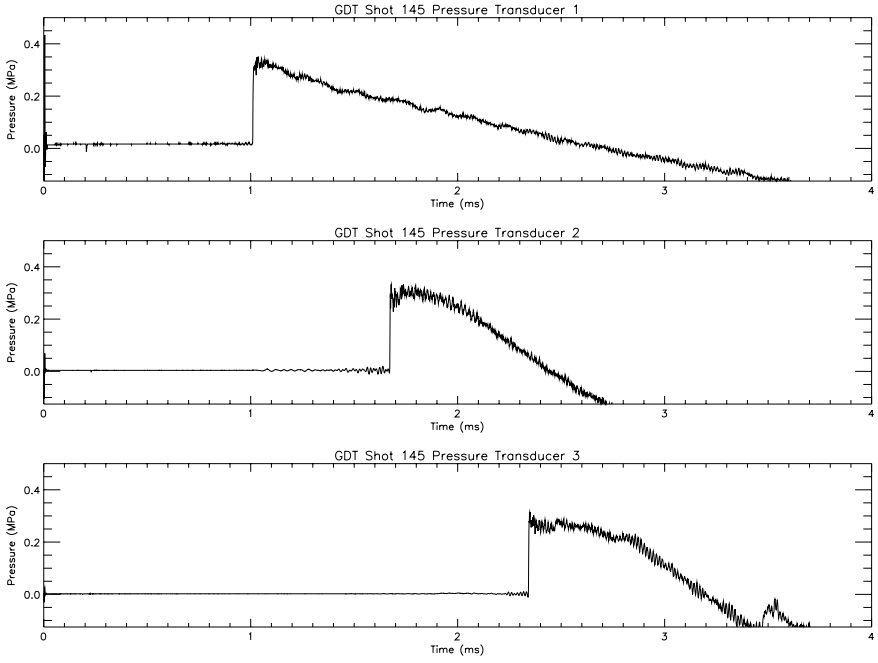

Figure C.2: Pressure Traces for Shot 145

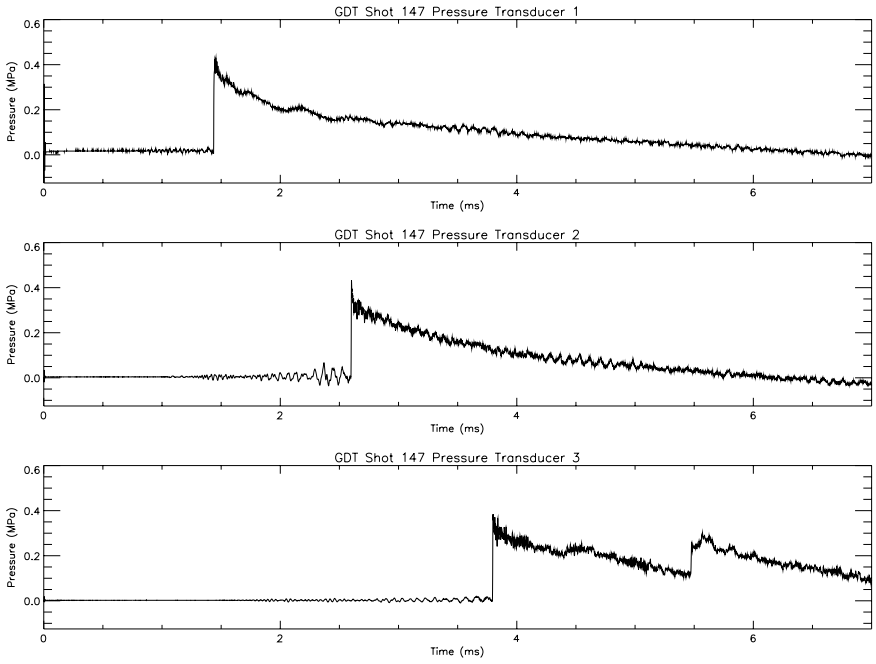

Figure C.3: Pressure Traces for Shot 147

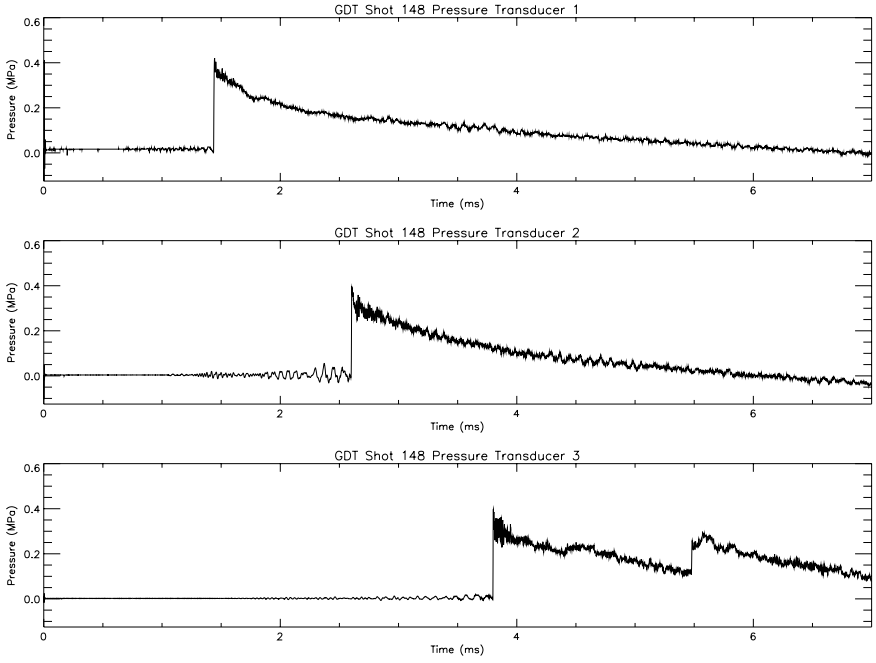

Figure C.4: Pressure Traces for Shot 148

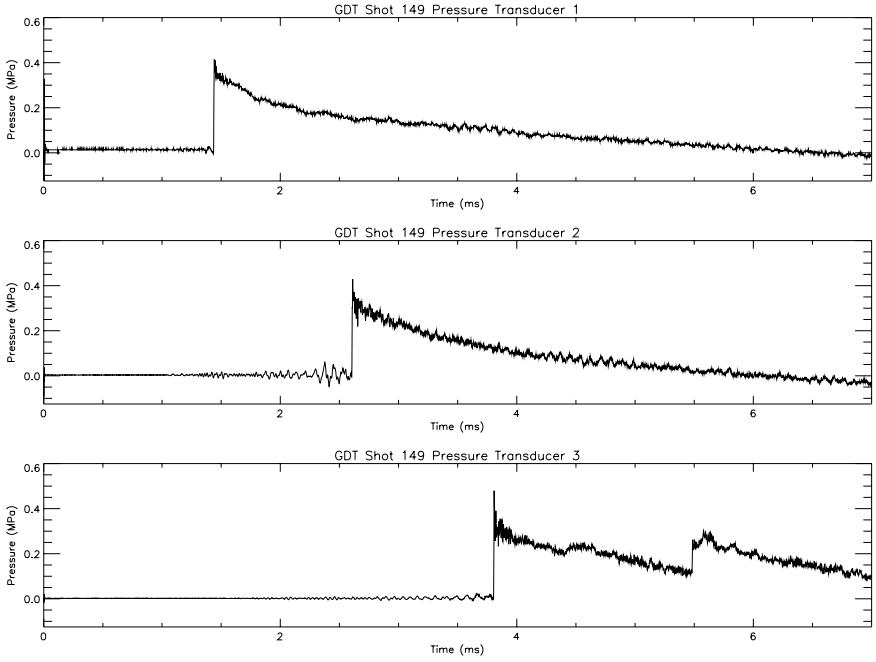

Figure C.5: Pressure Traces for Shot 149

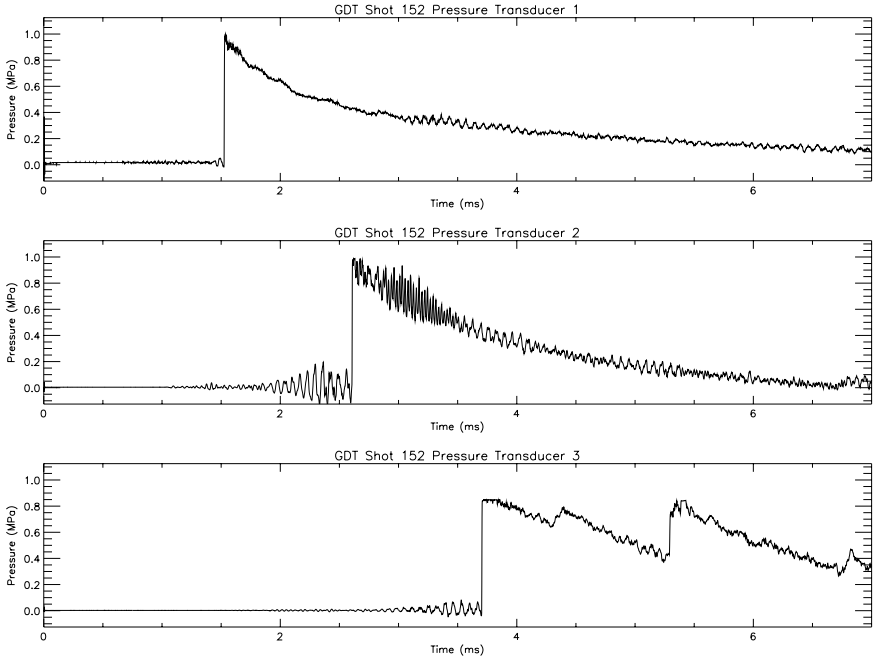

Figure C.6: Pressure Traces for Shot 152

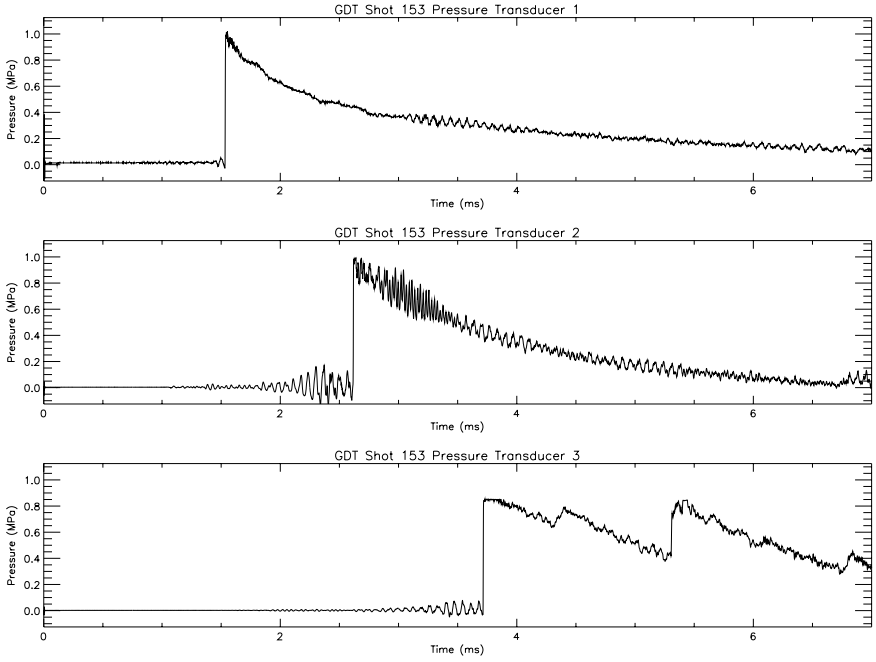

Figure C.7: Pressure Traces for Shot 153

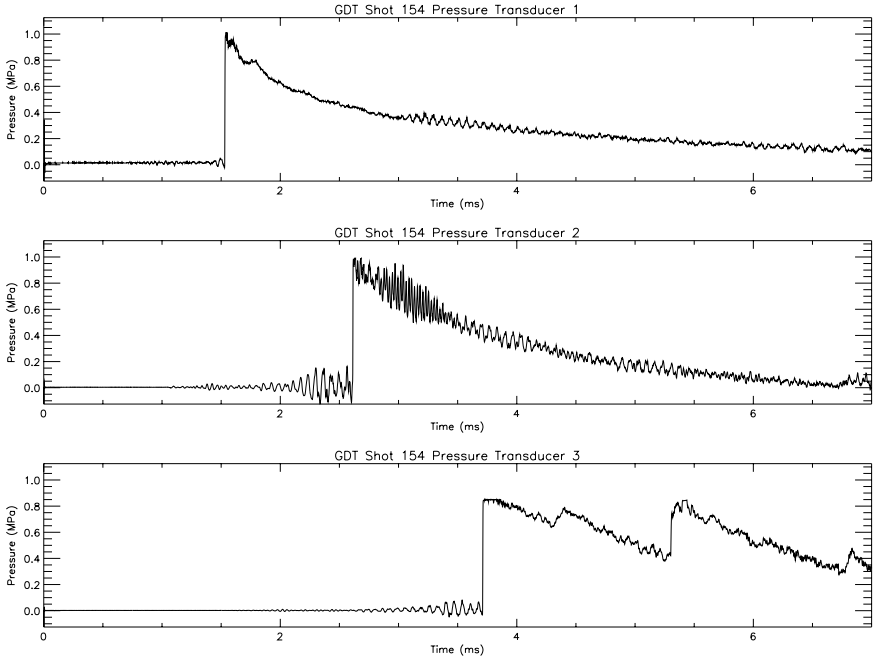

Figure C.8: Pressure Traces for Shot 154

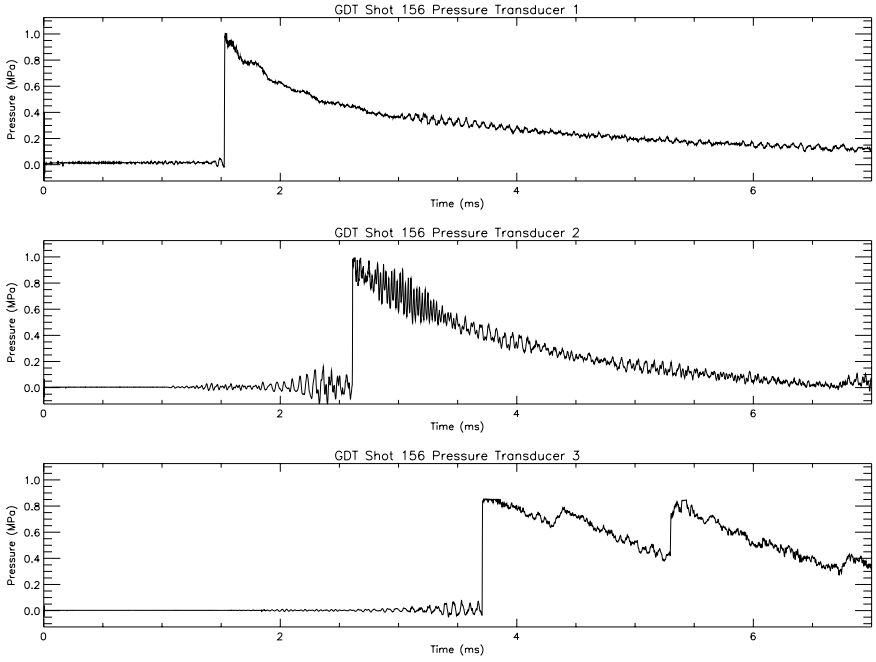

Figure C.9: Pressure Traces for Shot 156

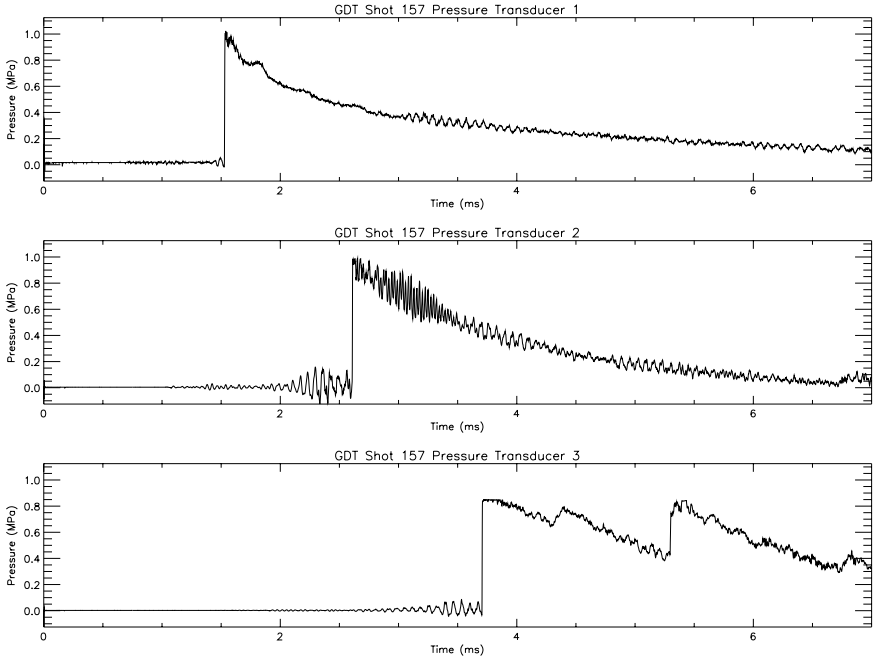

Figure C.10: Pressure Traces for Shot 157

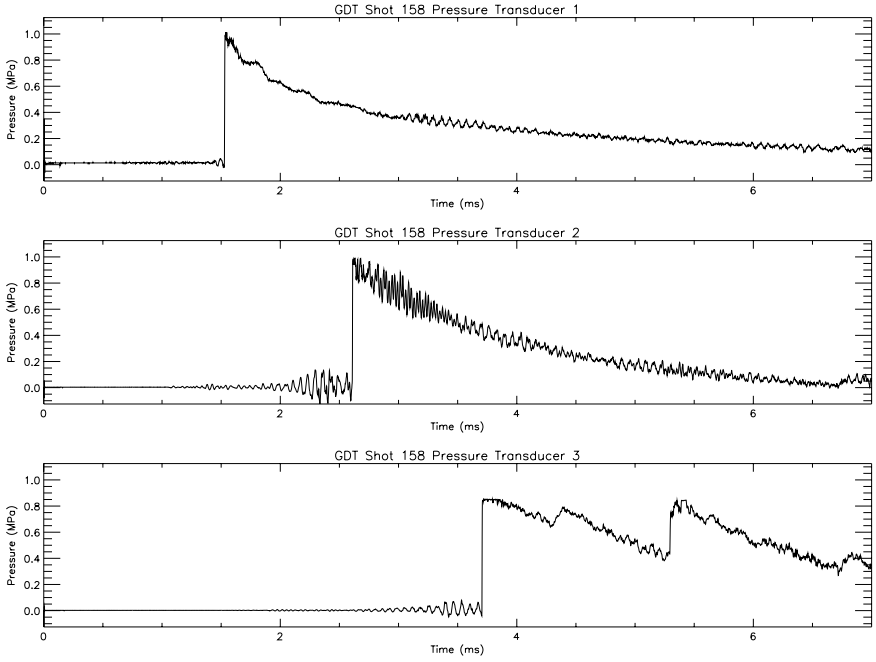

Figure C.11: Pressure Traces for Shot 158

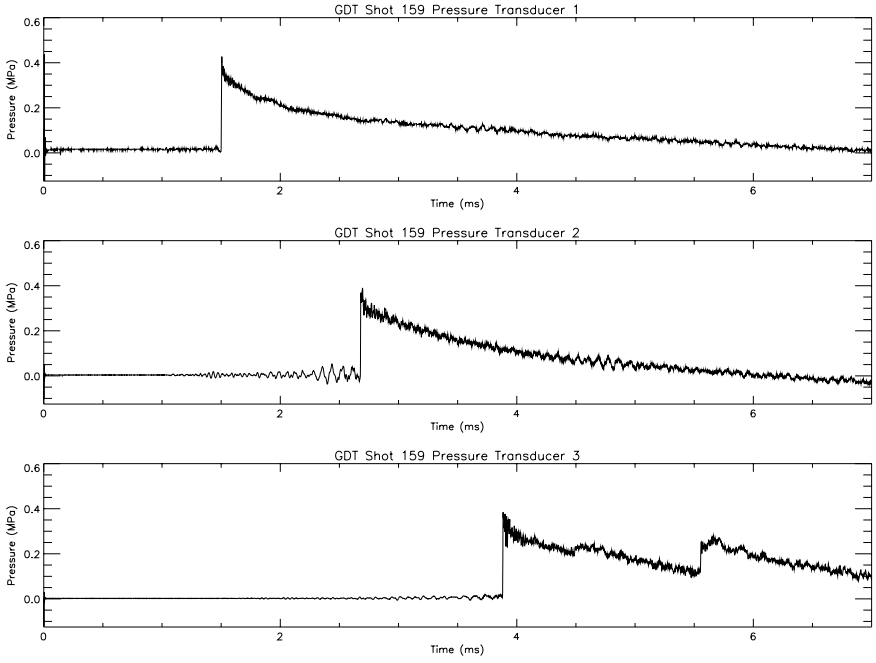

Figure C.12: Pressure Traces for Shot 159

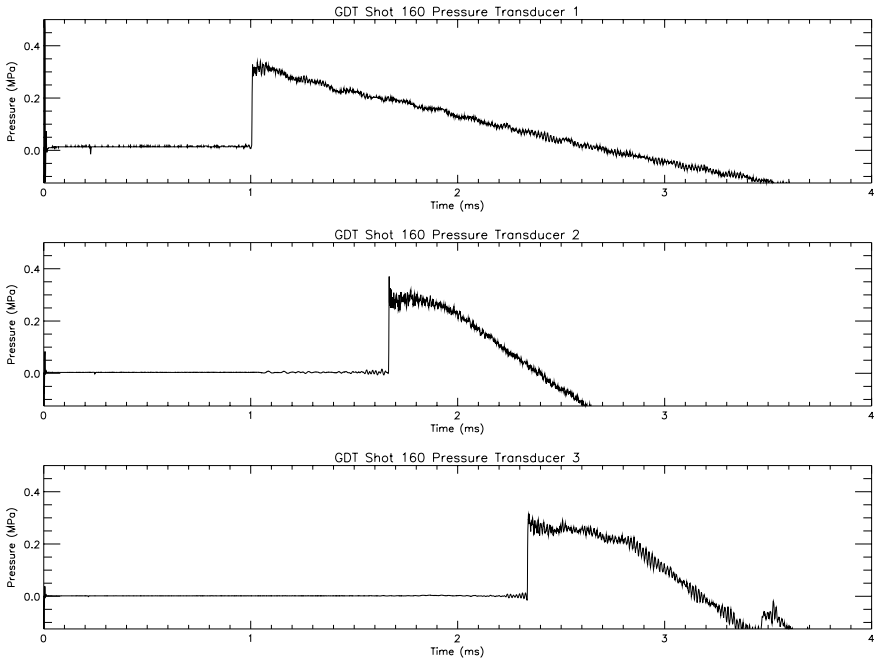

Figure C.13: Pressure Traces for Shot 160

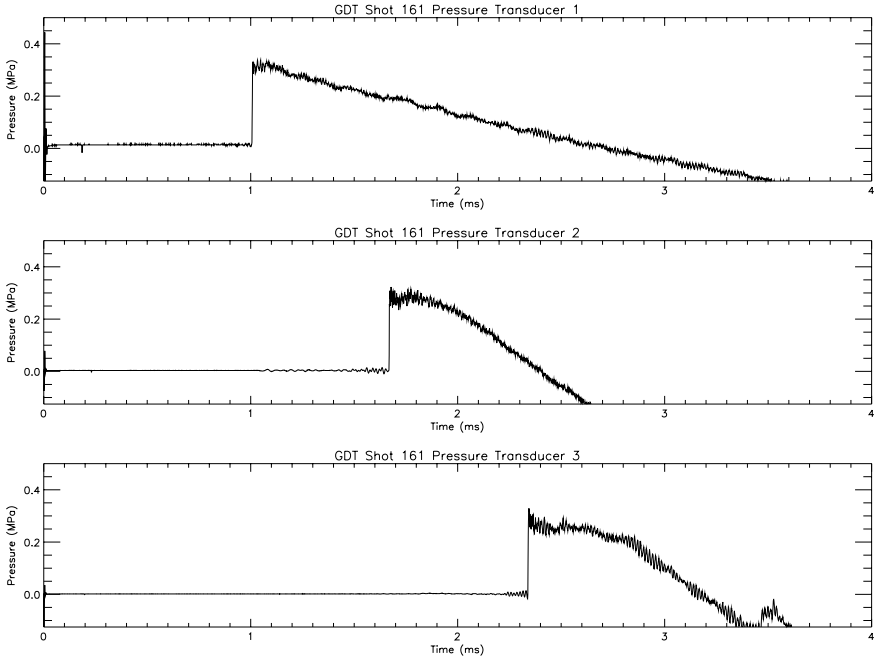

Figure C.14: Pressure Traces for Shot 161

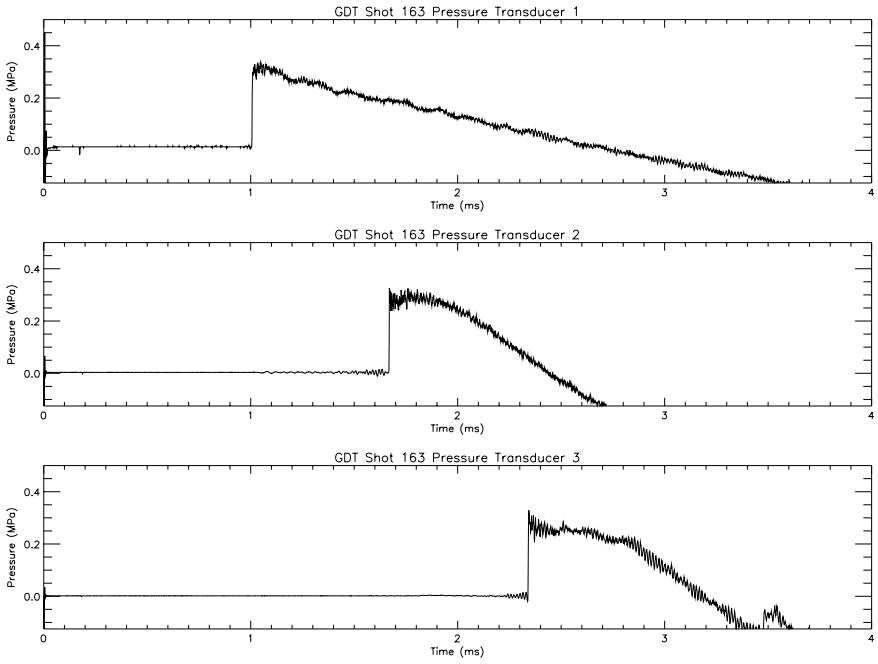

Figure C.15: Pressure Traces for Shot 163

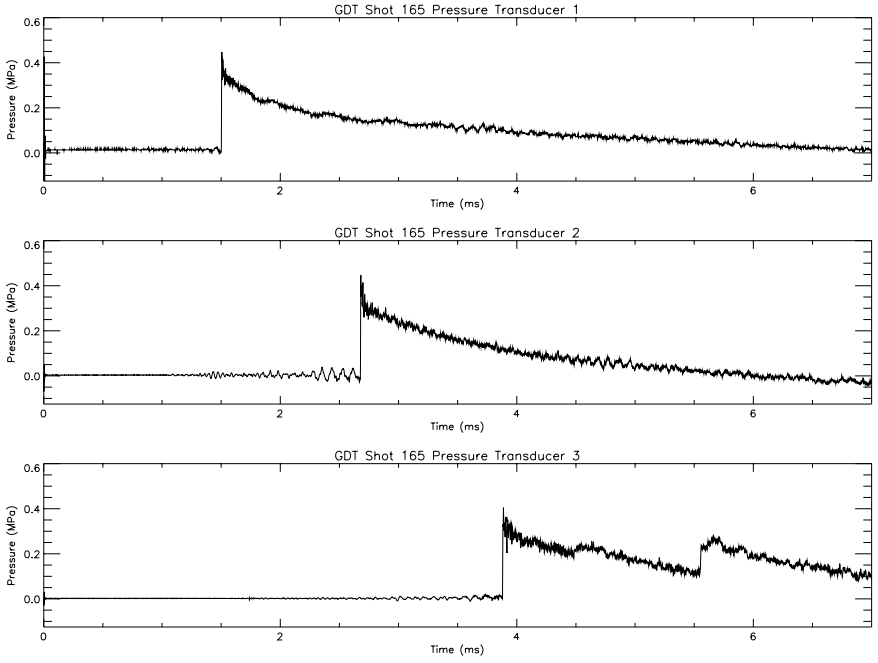

Figure C.16: Pressure Traces for Shot 165

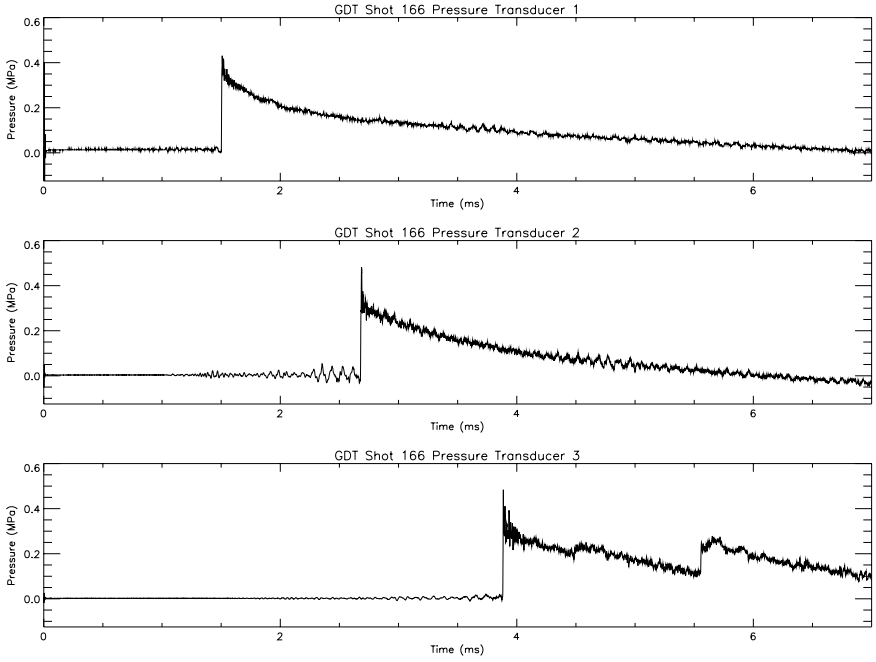

Figure C.17: Pressure Traces for Shot 166

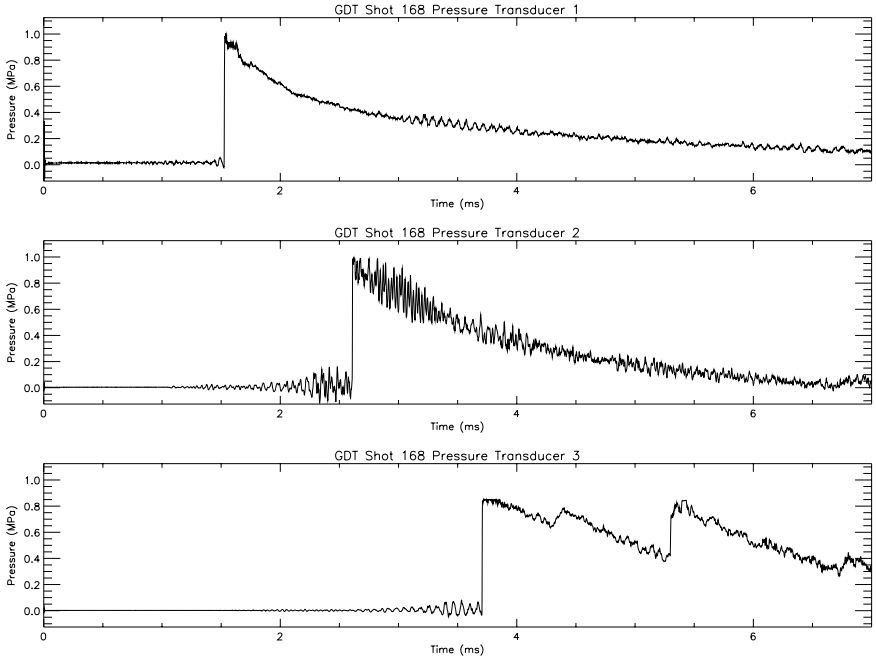

Figure C.18: Pressure Traces for Shot 168

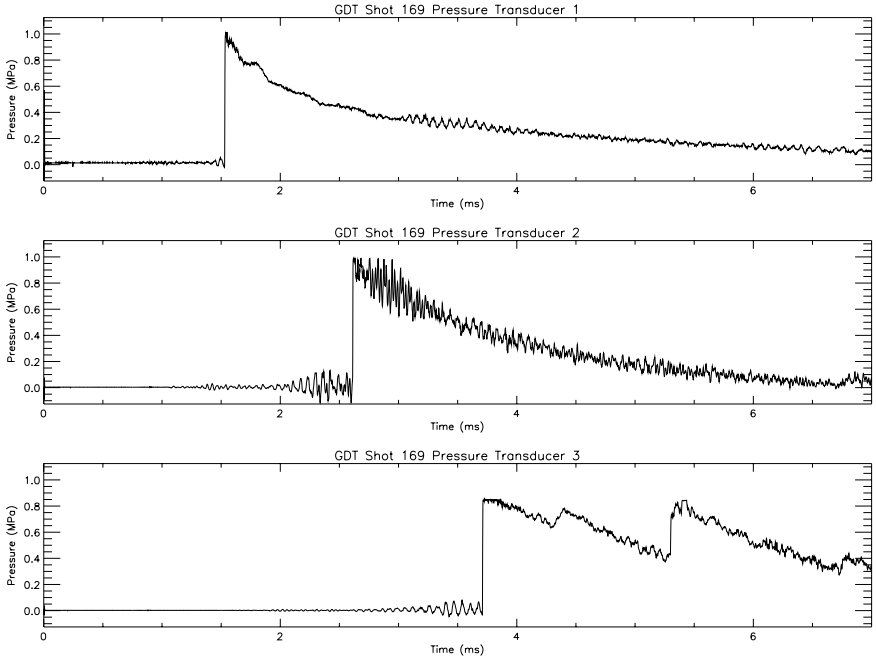

Figure C.19: Pressure Traces for Shot 169

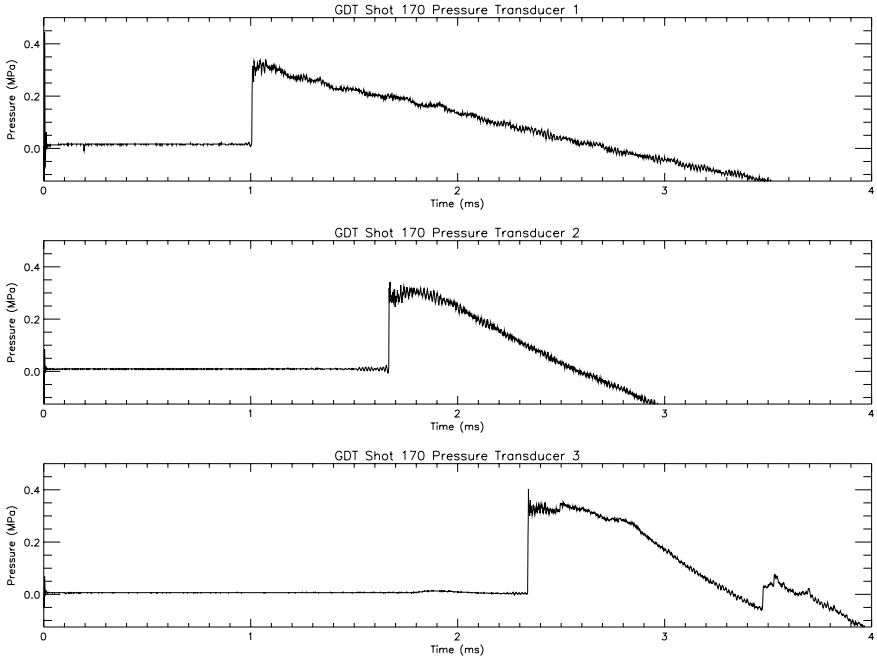

Figure C.20: Pressure Traces for Shot 170

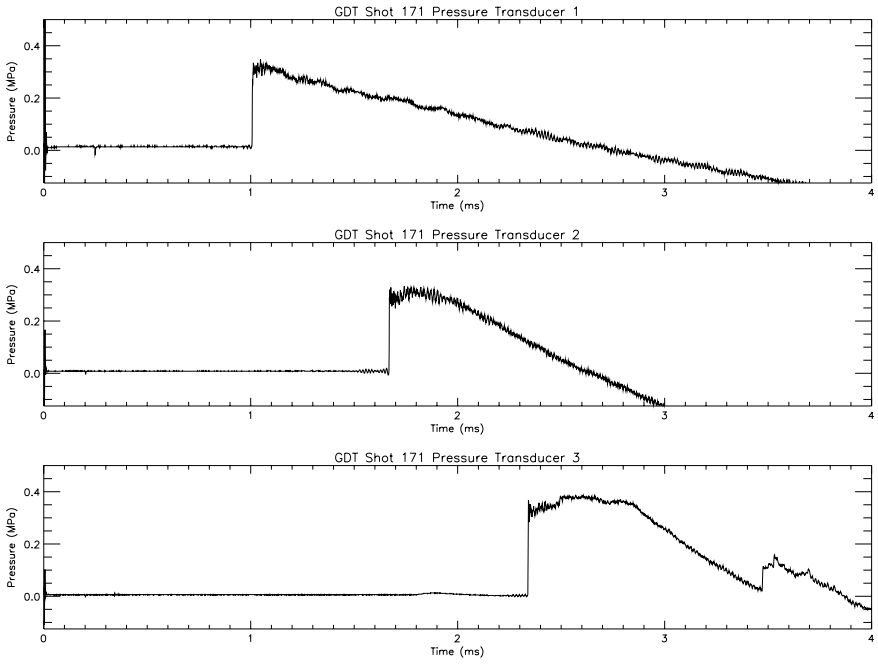

Figure C.21: Pressure Traces for Shot 171

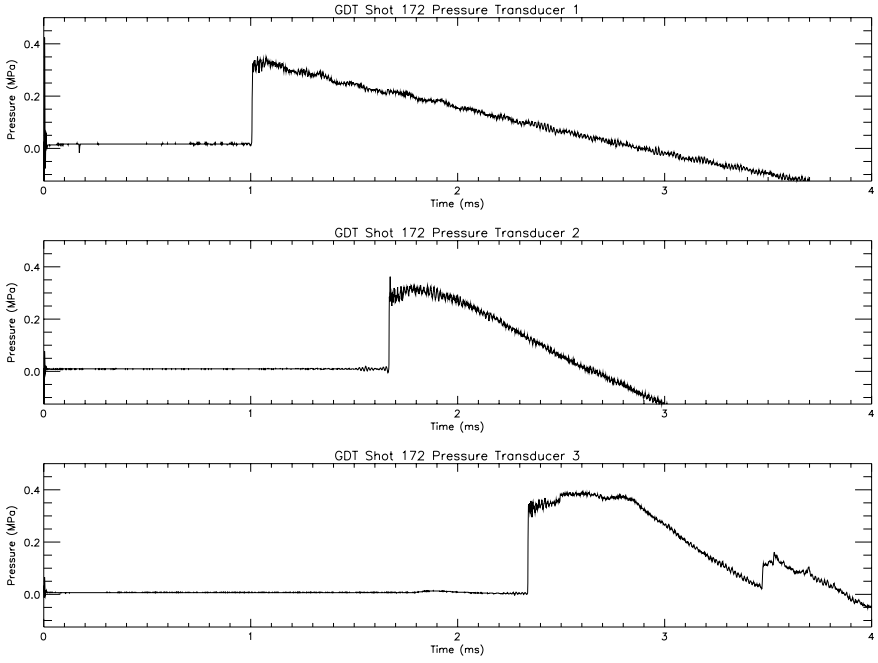

Figure C.22: Pressure Traces for Shot 172

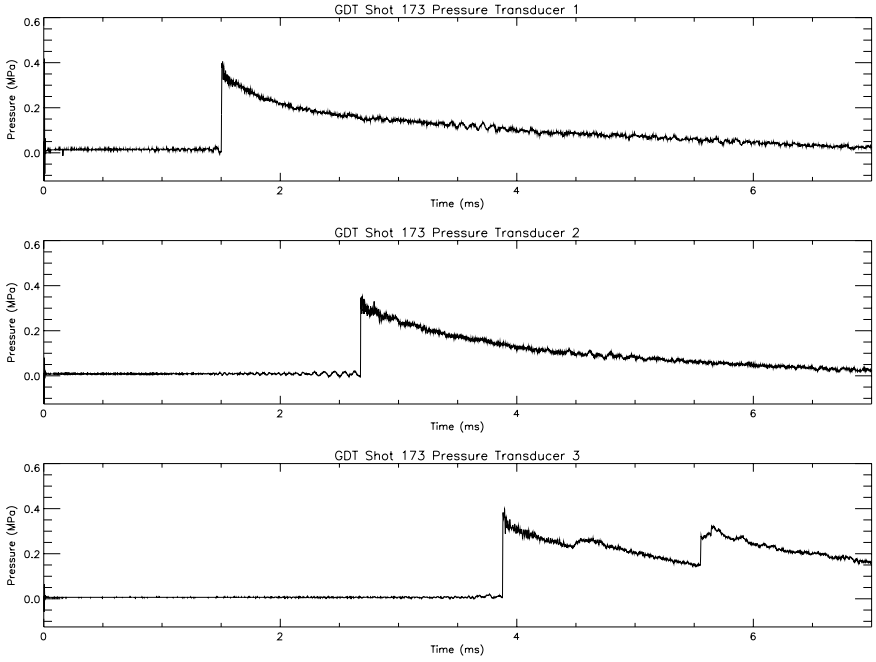

Figure C.23: Pressure Traces for Shot 173

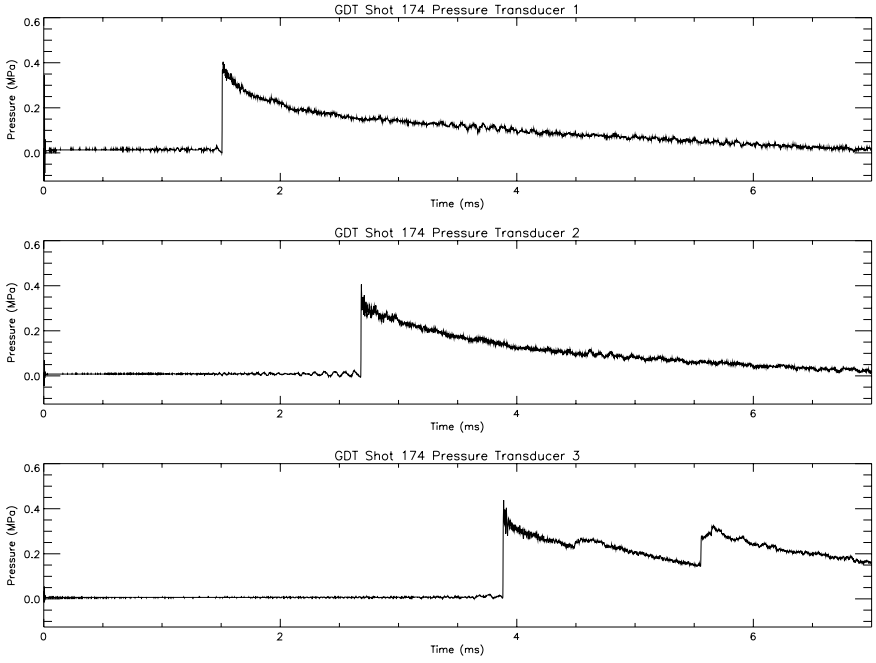

Figure C.24: Pressure Traces for Shot 174

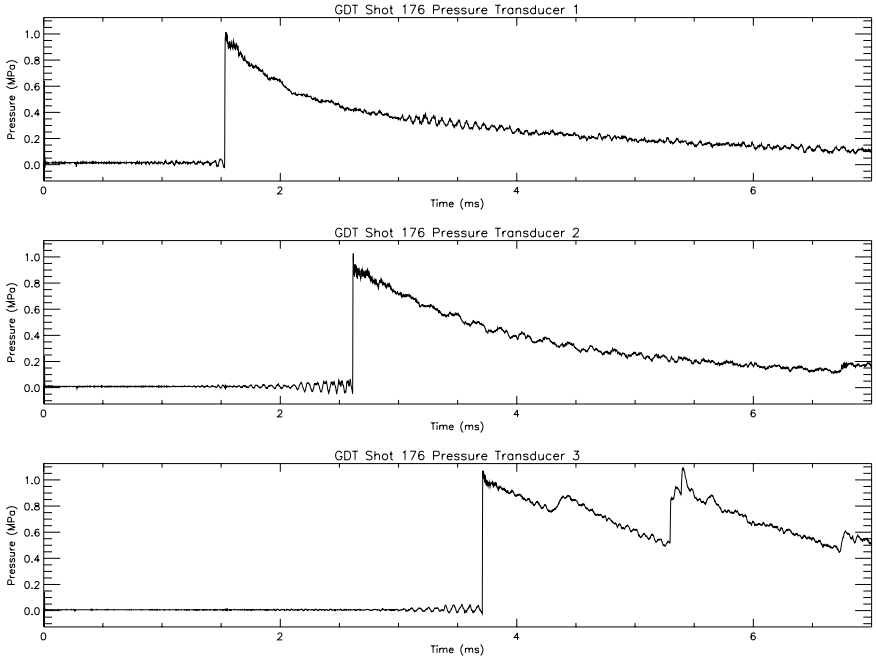

Figure C.25: Pressure Traces for Shot 176

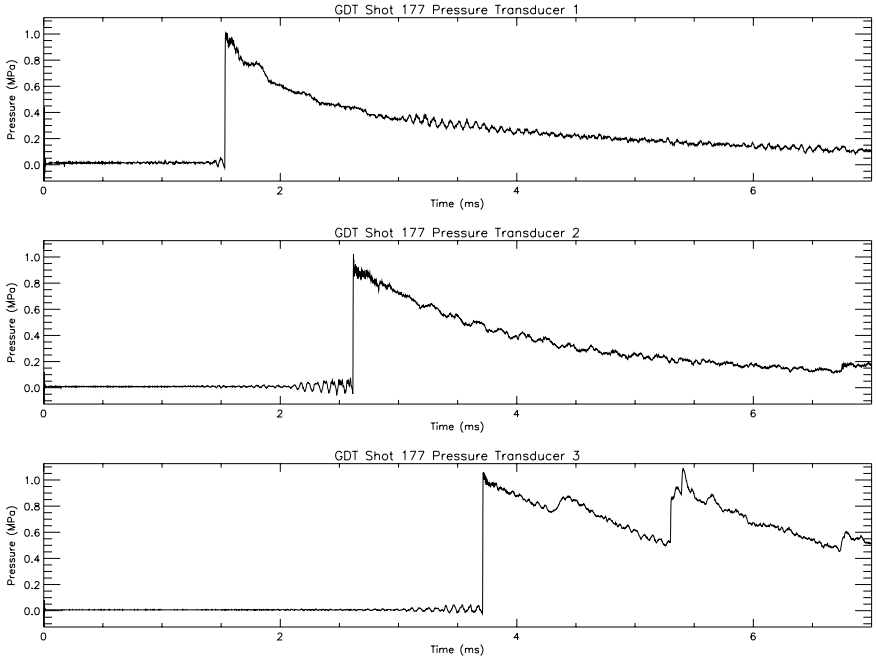

Figure C.26: Pressure Traces for Shot 177

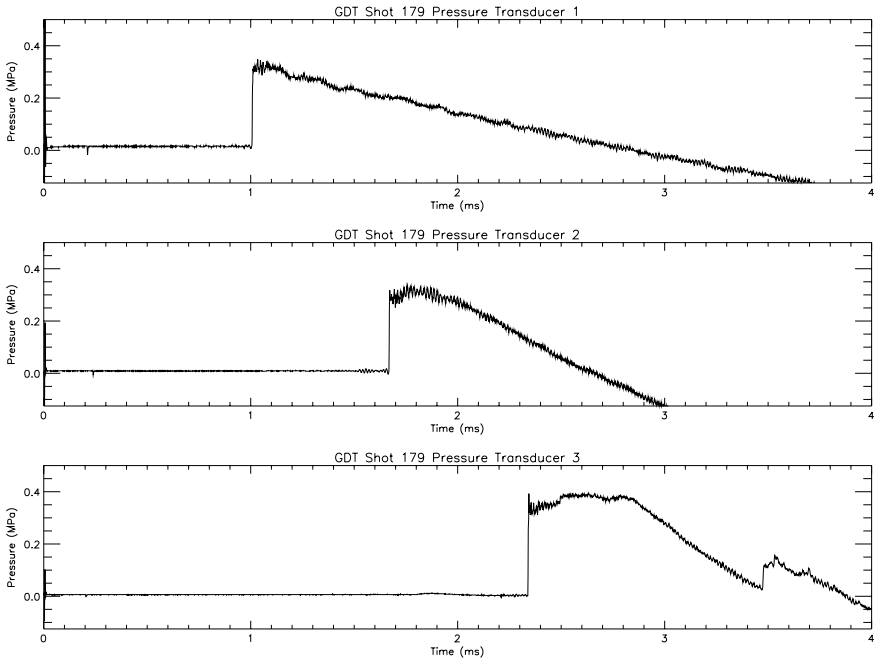

Figure C.27: Pressure Traces for Shot 179

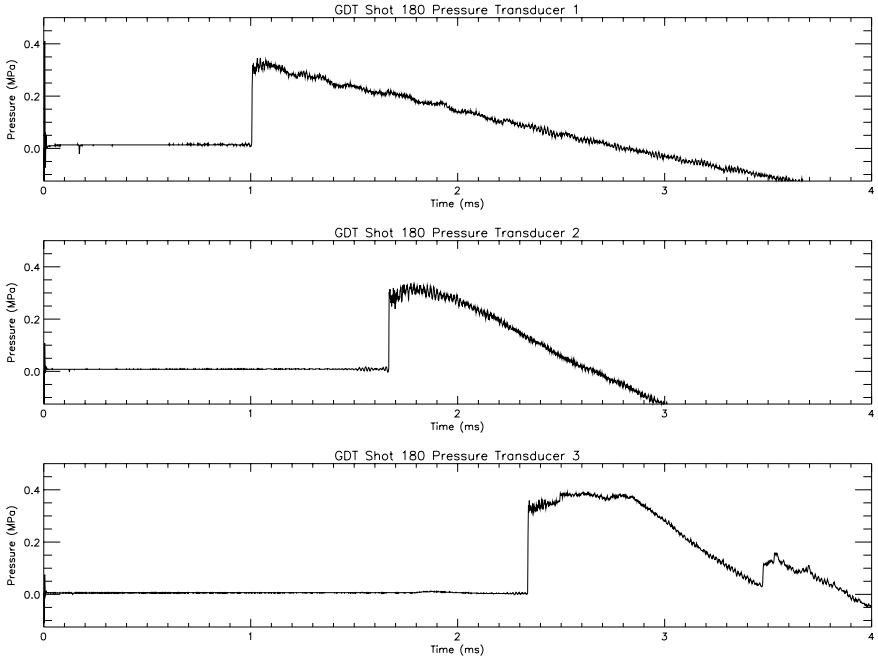

Figure C.28: Pressure Traces for Shot 180

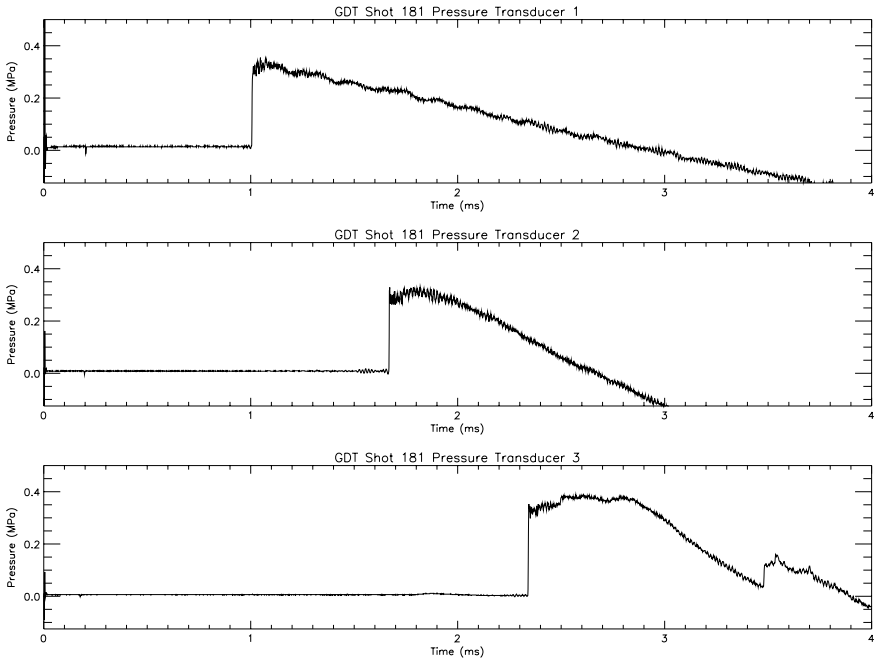

Figure C.29: Pressure Traces for Shot 181

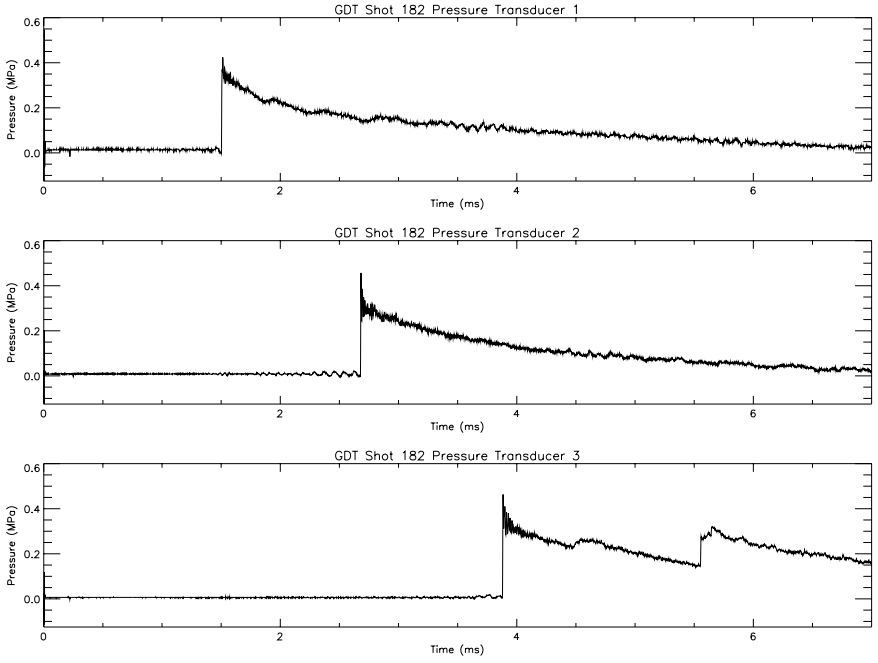

Figure C.30: Pressure Traces for Shot 182

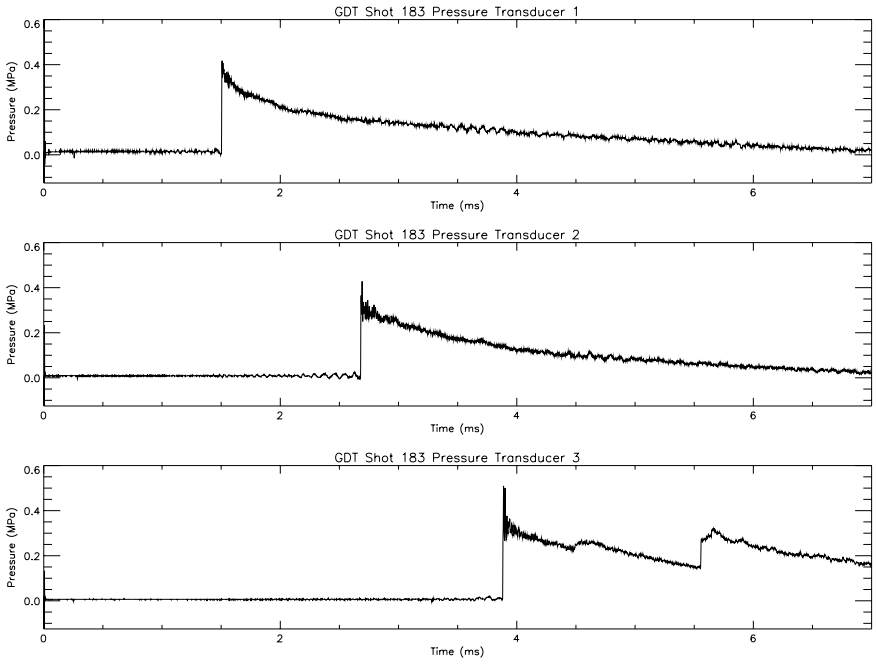

Figure C.31: Pressure Traces for Shot 183

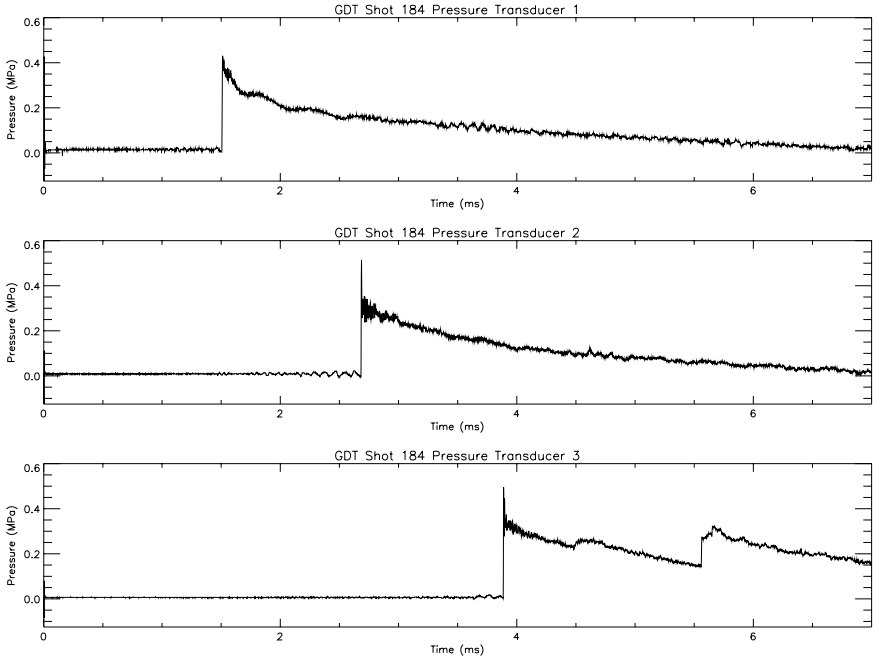

Figure C.32: Pressure Traces for Shot 184

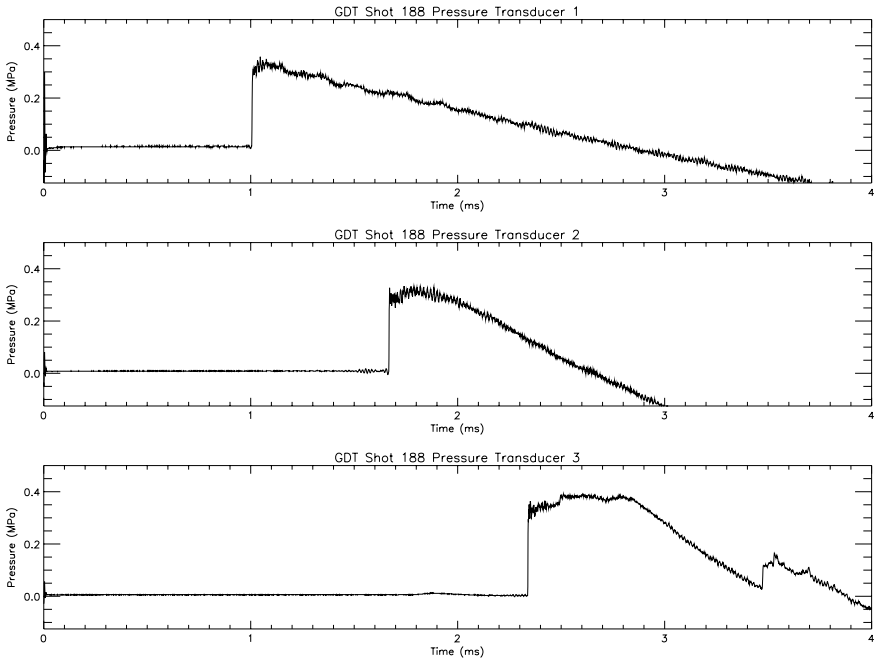

Figure C.33: Pressure Traces for Shot 188

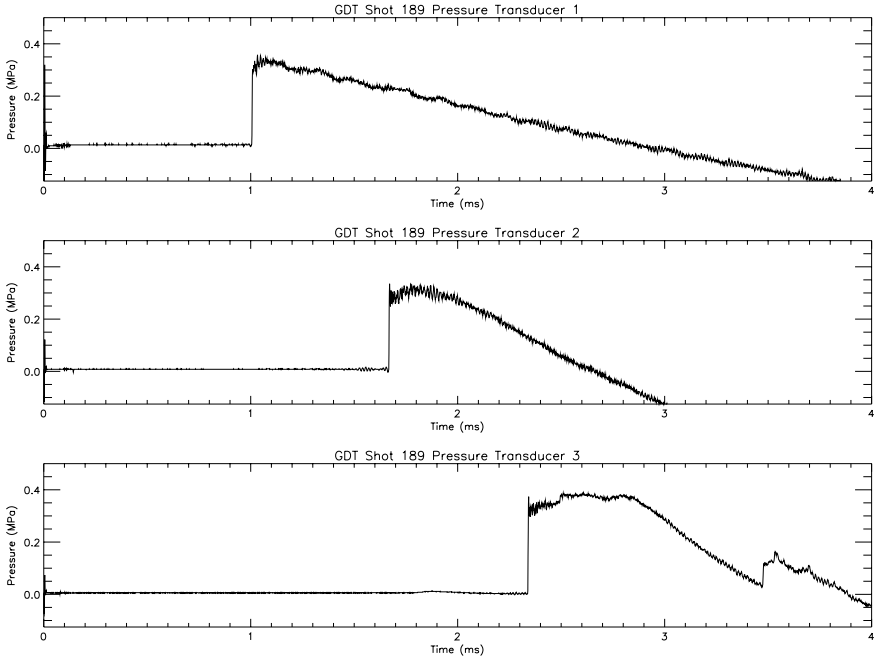

Figure C.34: Pressure Traces for Shot 189

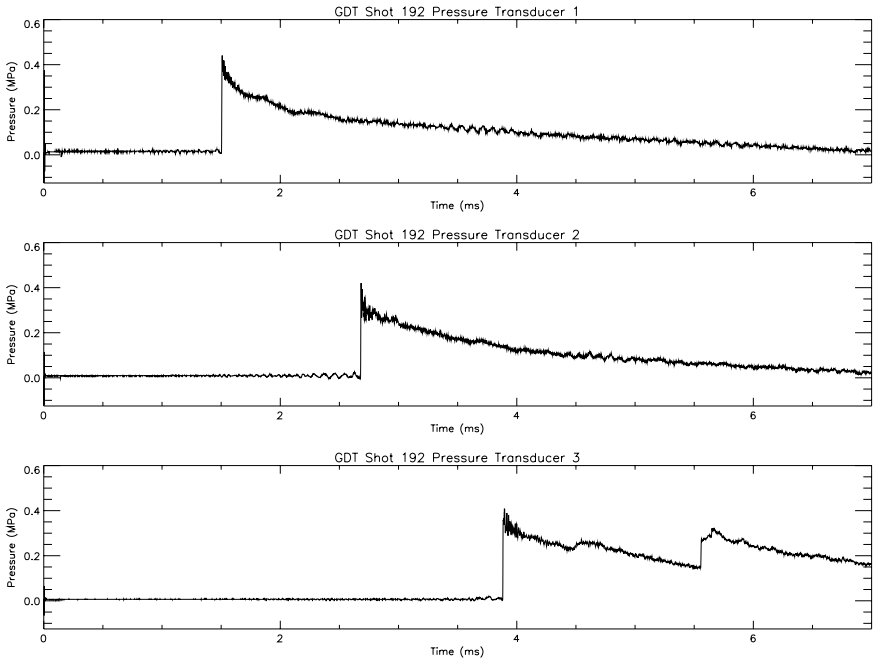

Figure C.35: Pressure Traces for Shot 192

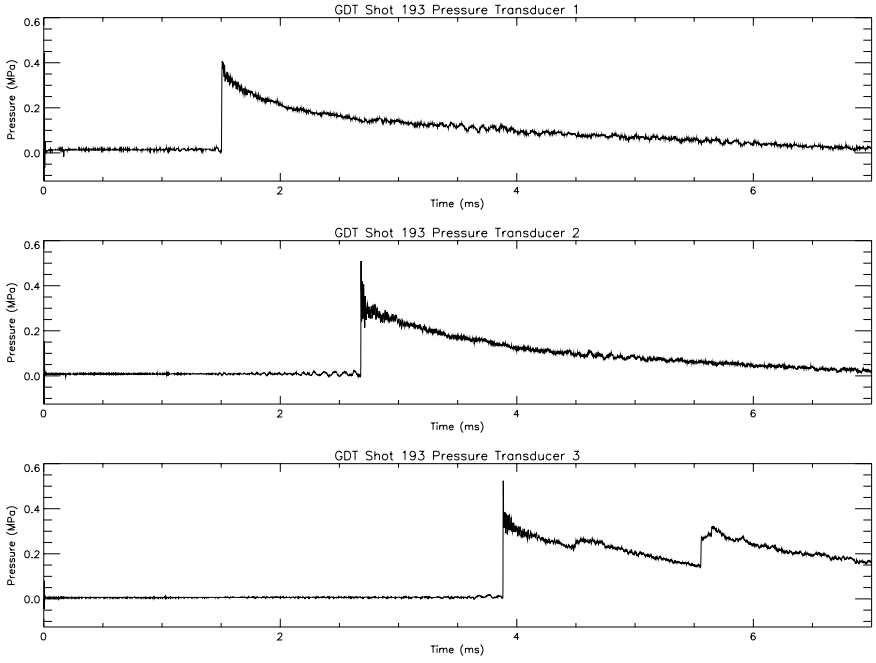

Figure C.36: Pressure Traces for Shot 193

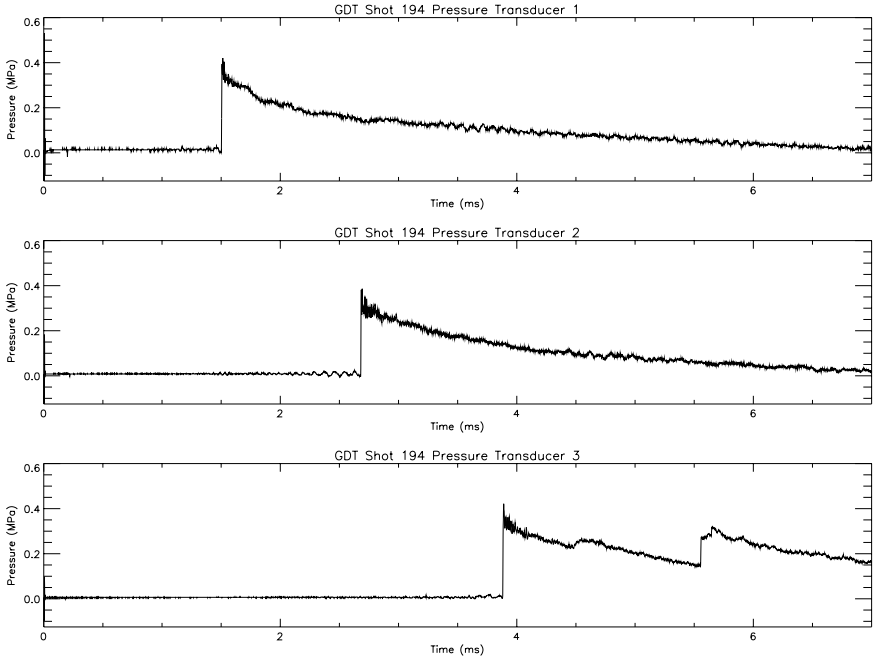

Figure C.37: Pressure Traces for Shot 194

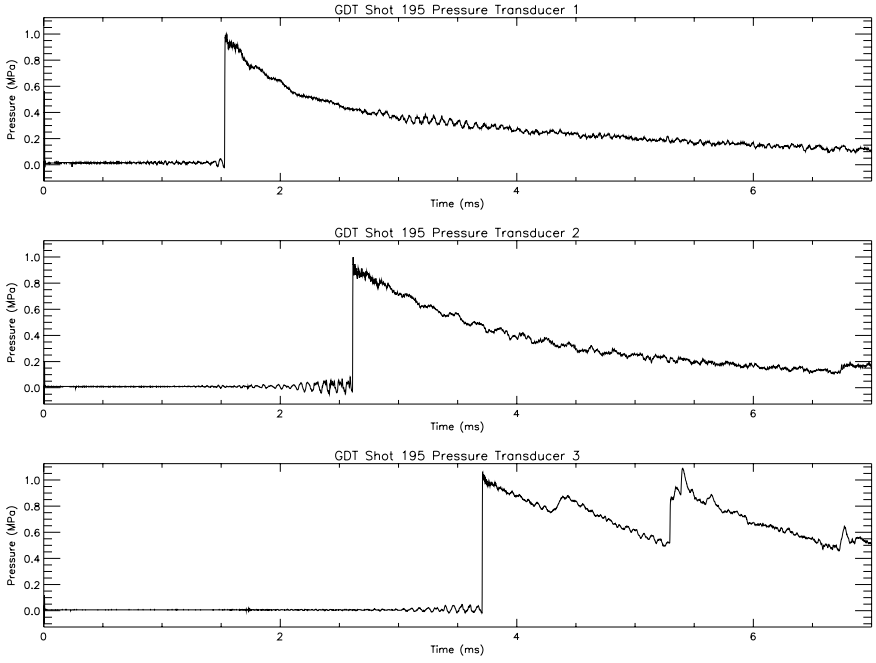

Figure C.38: Pressure Traces for Shot 195

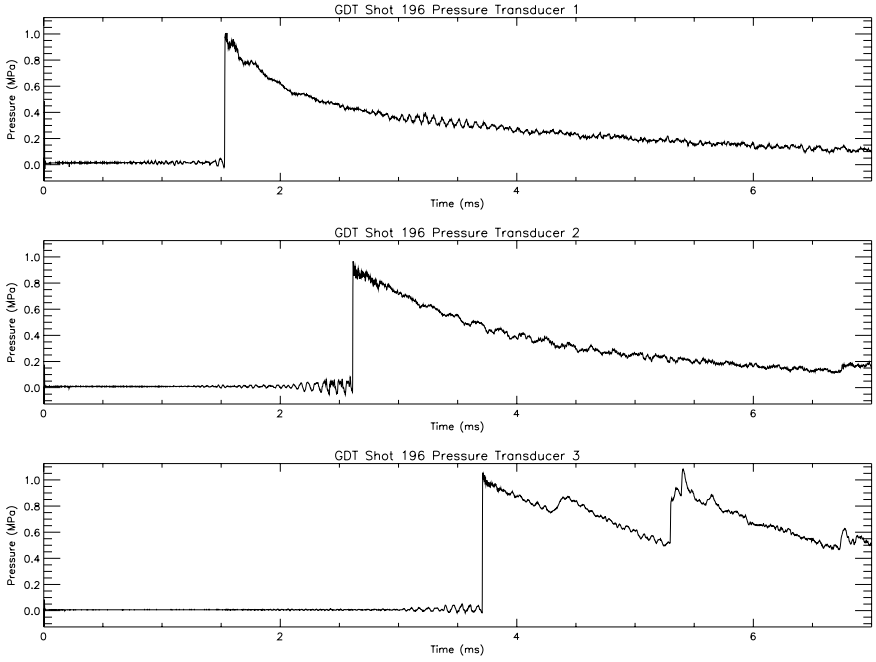

Figure C.39: Pressure Traces for Shot 196

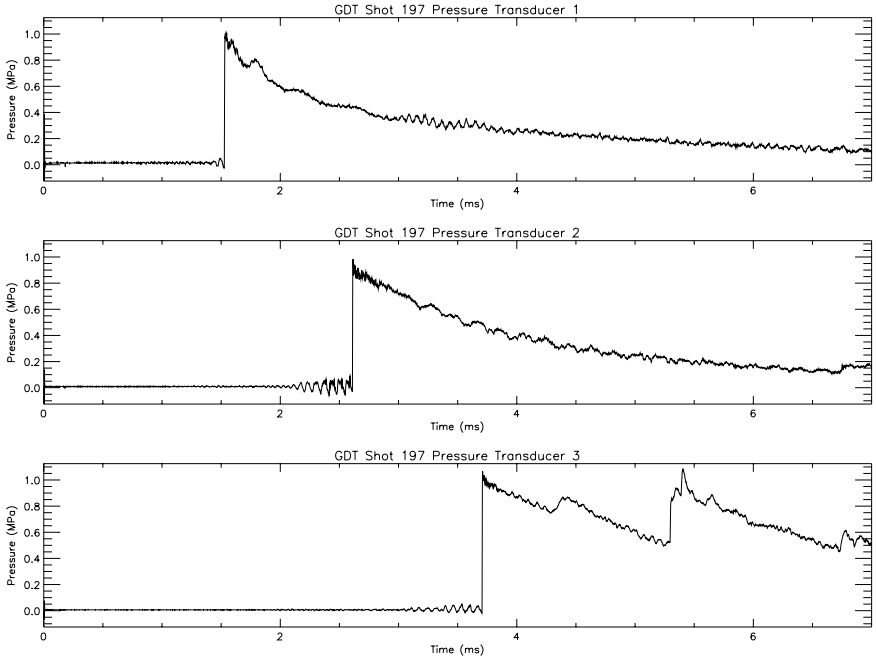

Figure C.40: Pressure Traces for Shot 197

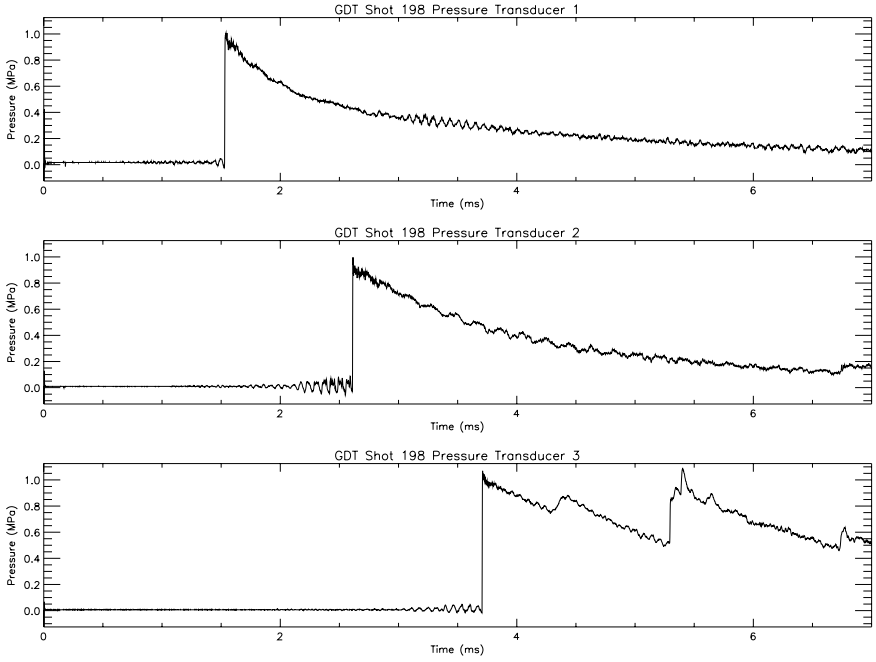

Figure C.41: Pressure Traces for Shot 198

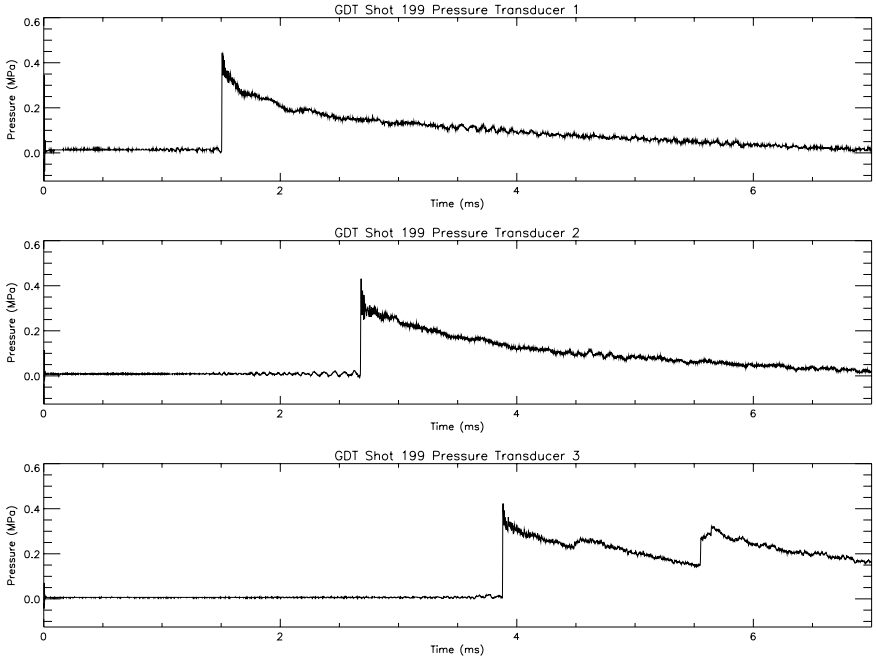

Figure C.42: Pressure Traces for Shot 199

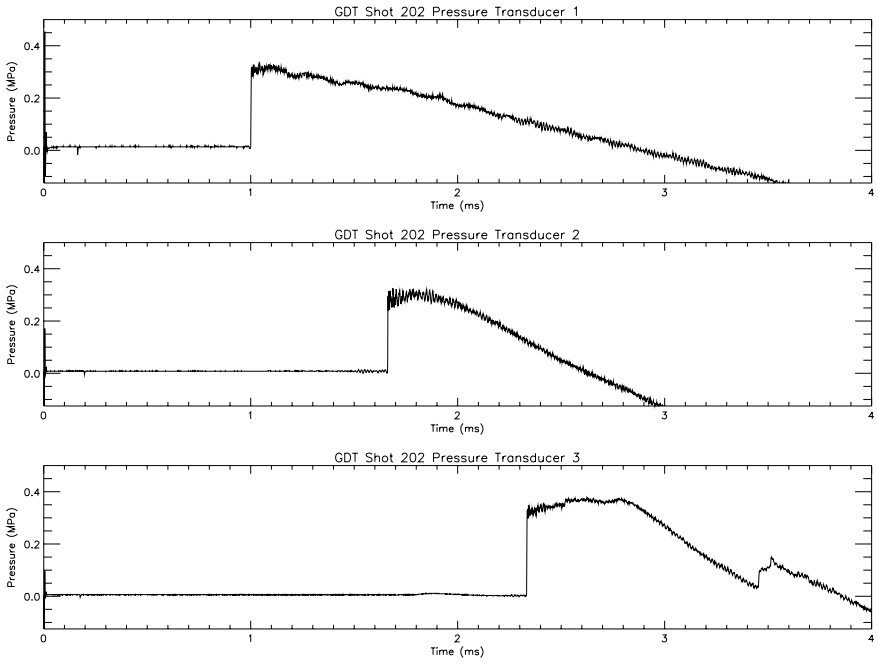

Figure C.43: Pressure Traces for Shot 202

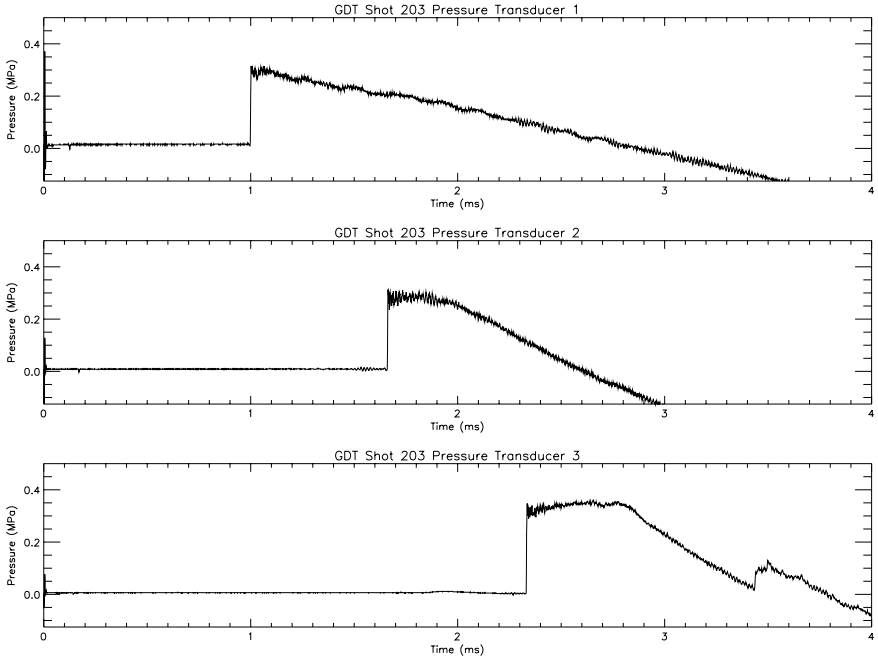

Figure C.44: Pressure Traces for Shot 203

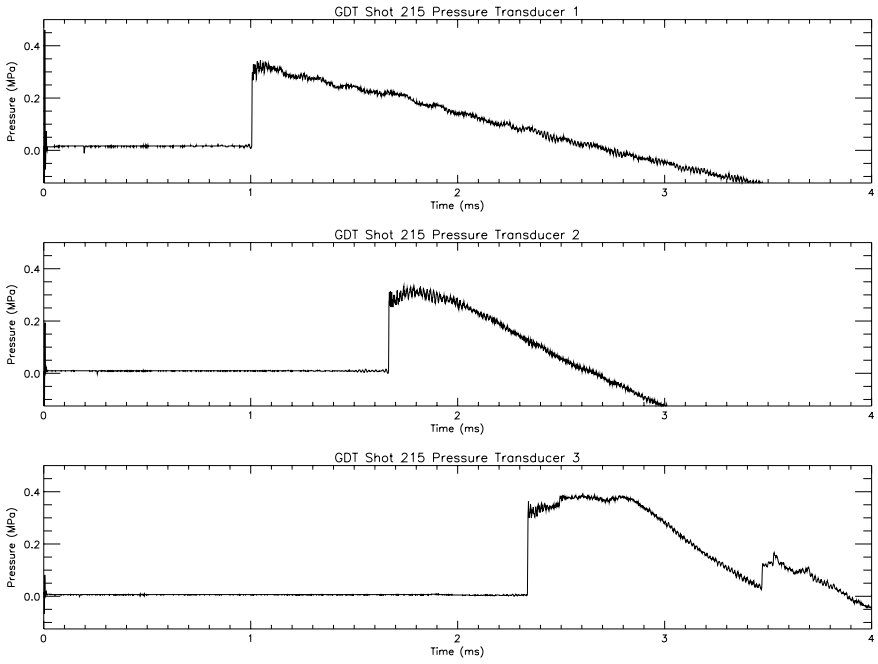

Figure C.45: Pressure Traces for Shot 215

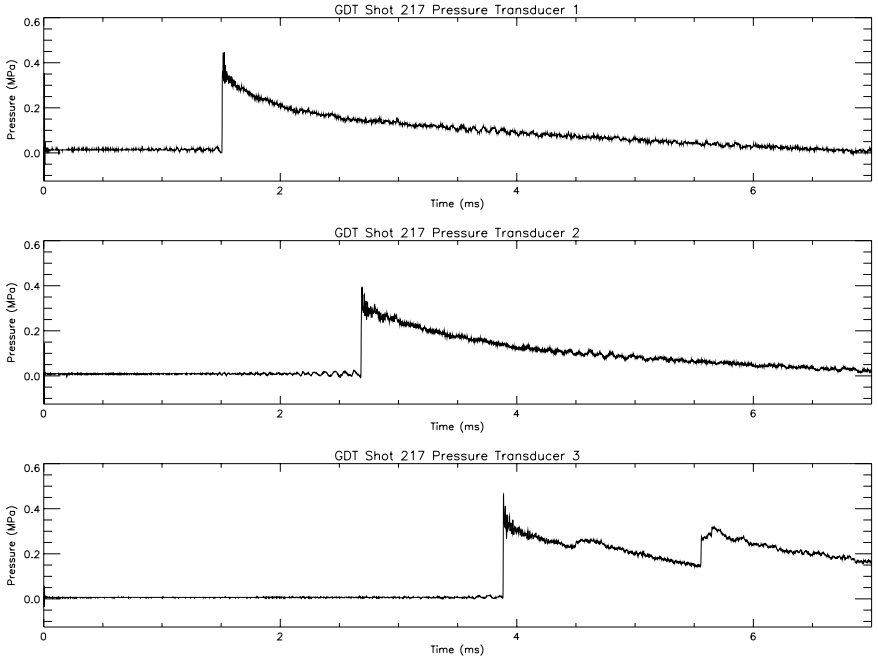

Figure C.46: Pressure Traces for Shot 217

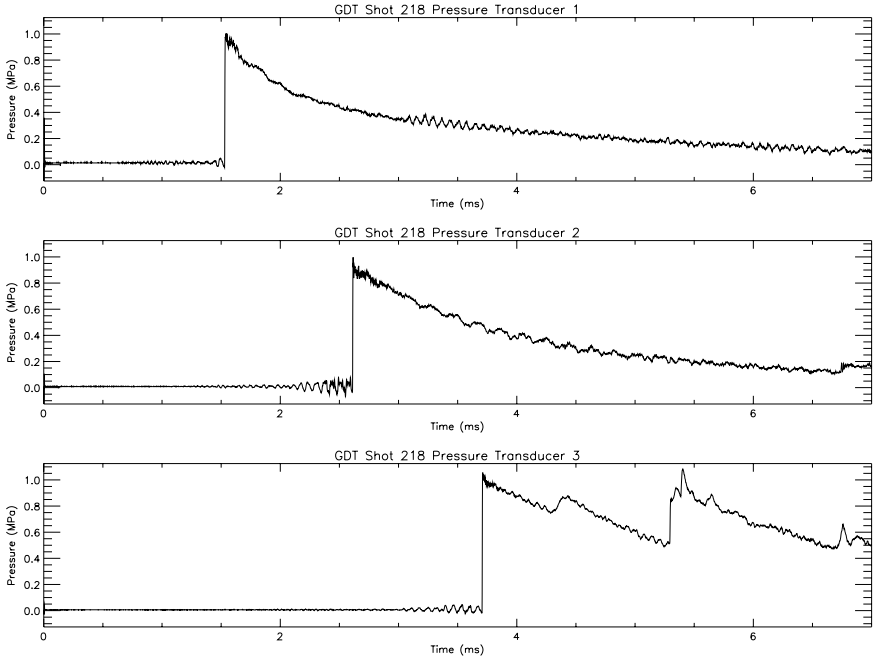

Figure C.47: Pressure Traces for Shot 218

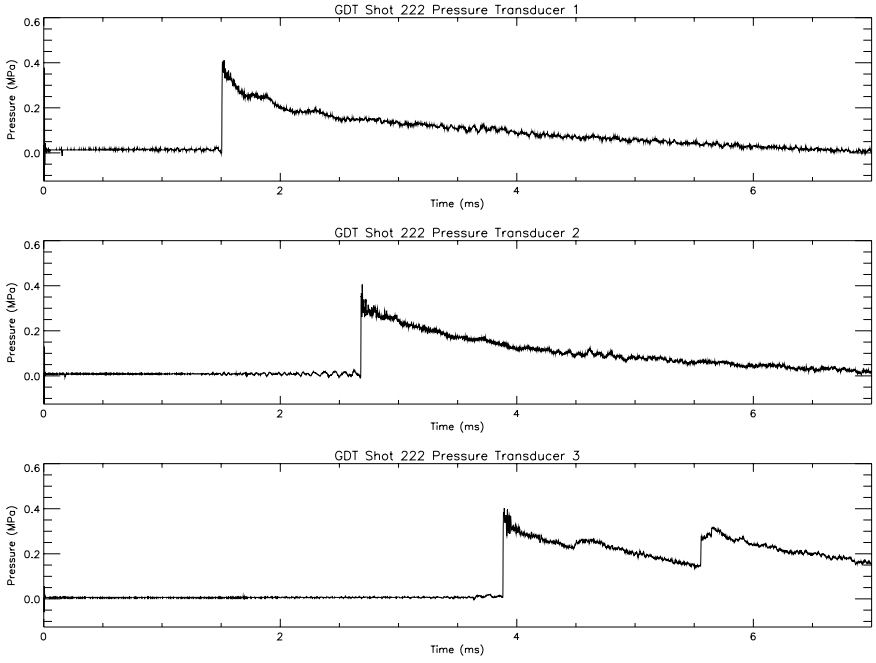

Figure C.48: Pressure Traces for Shot 222

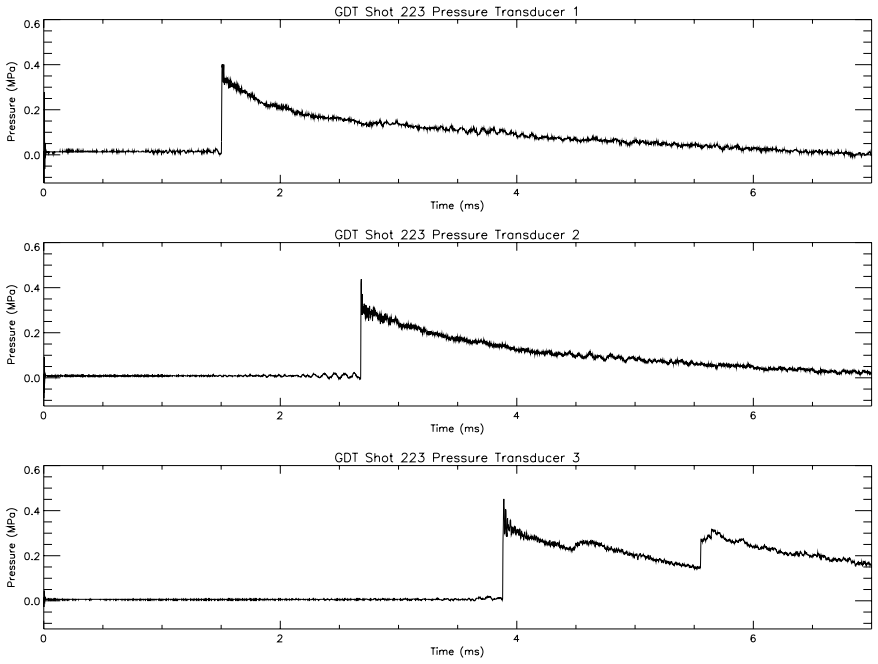

Figure C.49: Pressure Traces for Shot 223

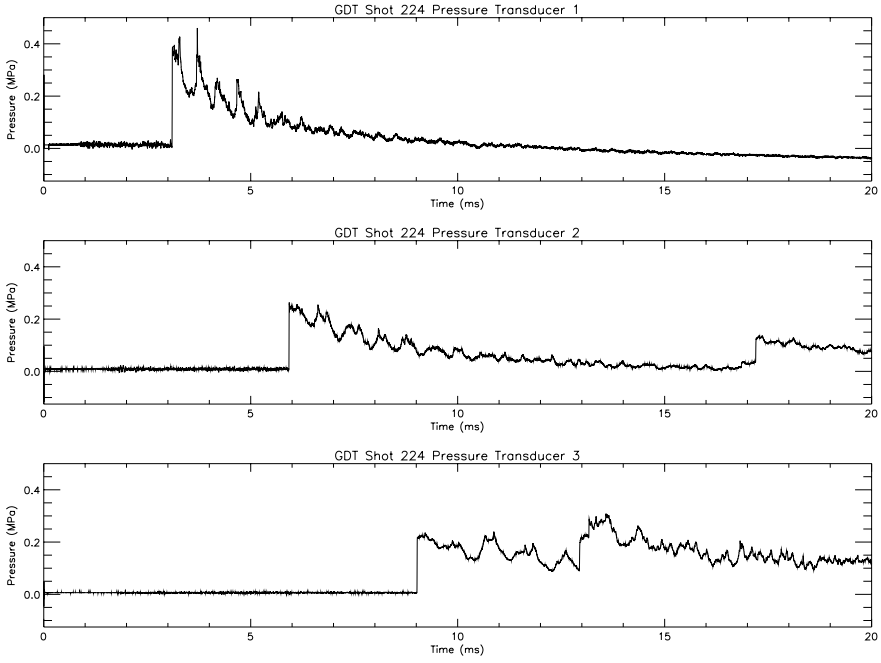

Figure C.50: Pressure Traces for Shot 224

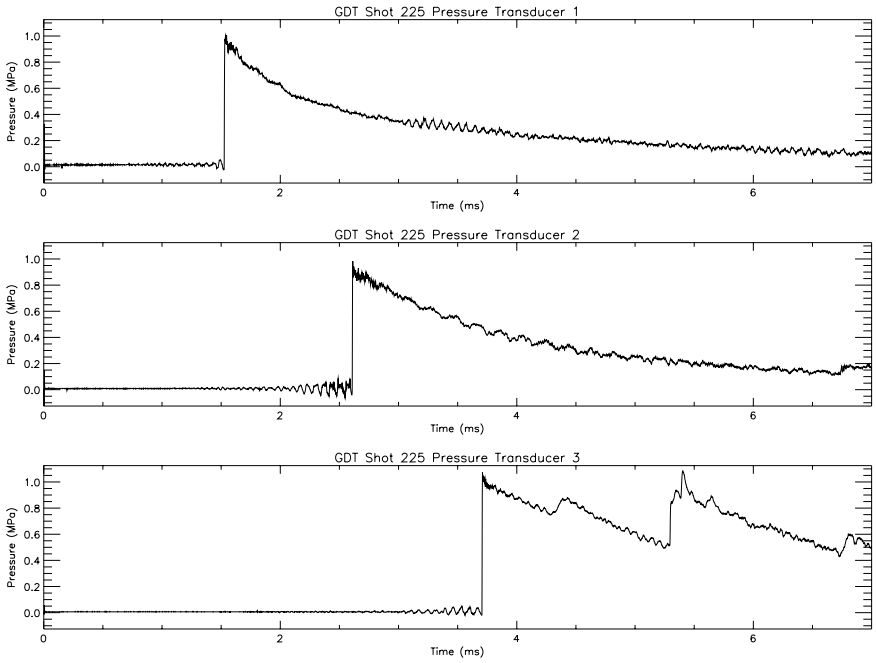

Figure C.51: Pressure Traces for Shot 225